1

Studies in magnetic β-spectrometry

D. Michelson

ProQuest Number: 10098073

ProQuest 10098073

Abstract.

Part I.

A number of modifications were made to the large spheroidal field β-spectrometer and a small lens spectrometer was attached to it for β-β coincidence measurements. The method of ion ejection from a capillary tube for preparing thin sources was developed and used for making Ce^{144} sources. An attempt was made to verify the existence of a 166 keV excited state in Pr^{144} suggested by some investigators by observing the predicted γ-γ cascade, i.e. 33 keV γ-ray followed by a 133 keV γ-ray. No evidence of β-β coincidences between the K133 and $L_1$33 conversion lines was found

Part II.

The trajectories of electrons in a spheroidal field were found by integrating the equations of motion using the electronic computer 'Mercury' of the University of London. The focusing properties of a β-spectrometer using this field were investigated and an attempt was made to find an analytical form for the field intensity which would describe the field in the large spectrometer.

Acknowledgements.

The author would like to express her gratitude to Professor Richardson. The work described in this thesis was done in collaboration with Professor Richardson. The following were however the sole responsibility of the author: in Part I, the construction and testing of the selective amplifier (Fig. 17) for which the circuit was suggested by Dr. Little, the holders for the revolution counters for the control rods, the preparation of the source backing, the apparatus in Fig. 25 (with the exception of the power supplies), the centering of the large spectrometer during operation and tests of the resolving power (Figs. 27-31), Fig. 33, construction of holder for the lamp and mirror inside the large spectrometer; in Part II, the computation and programming, processing of the data and the use of the combined field in Chapter IV.

The author would like to thank Dr. Buckingham for making the facilities of the London University Computer Unit available, Dr. Cooper for reference 17 on the Autocode Runge-Kutta integration, the Council of Bedford College for a Paterson Scholarship and the D.S.I.R. for a Research Studentship.

The author would also like to thank the technical staff of the Physics Department of Bedford College, especially Mr. Greenfield and Mr. Grimes.

Contents.

Part I

Part II

Part I

Key to Figures.

I

Introduction.

The study of beta decay has a double interest in nuclear physics. One is to study the beta decay theories and to determine the constants involved in the beta interaction and other weak interactions. The other is in nuclear spectroscopy as a tool for investigating decay schemes and the properties of nuclear states, their energy, parity and spins so as to provide some guidance in the selection of nuclear models.

When investigating decay schemes of excited nuclei which undergo isomeric transitions, the problem consists of finding the gamma rays and assigning the correct energy levels to the nucleus. Due to the development of scintillation counters, high resolution beta spectrometers ref. [14-19] and coincidence circuits with short resolving times, it has been possible to use coincidence techniques in investigating the cascades.

In the present work the 285 day fission product Ce^{144} was investigated. A number of investigations of this nucleus have been made by measuring the γ-rays emitted by Pr^{144}, $\beta-\gamma$ coincidences and $\gamma-\gamma$ coincidences. The results of these have been collected in Fig. 1(i) and 1(ii) and analysed in Tables I and II [1-13]. The results have been set out in approximately chronological order. The gamma rays found by only one investigator are in the 1st and last columns of Table I. It can be seen that there is some disagreement between the proposed decay schemes.
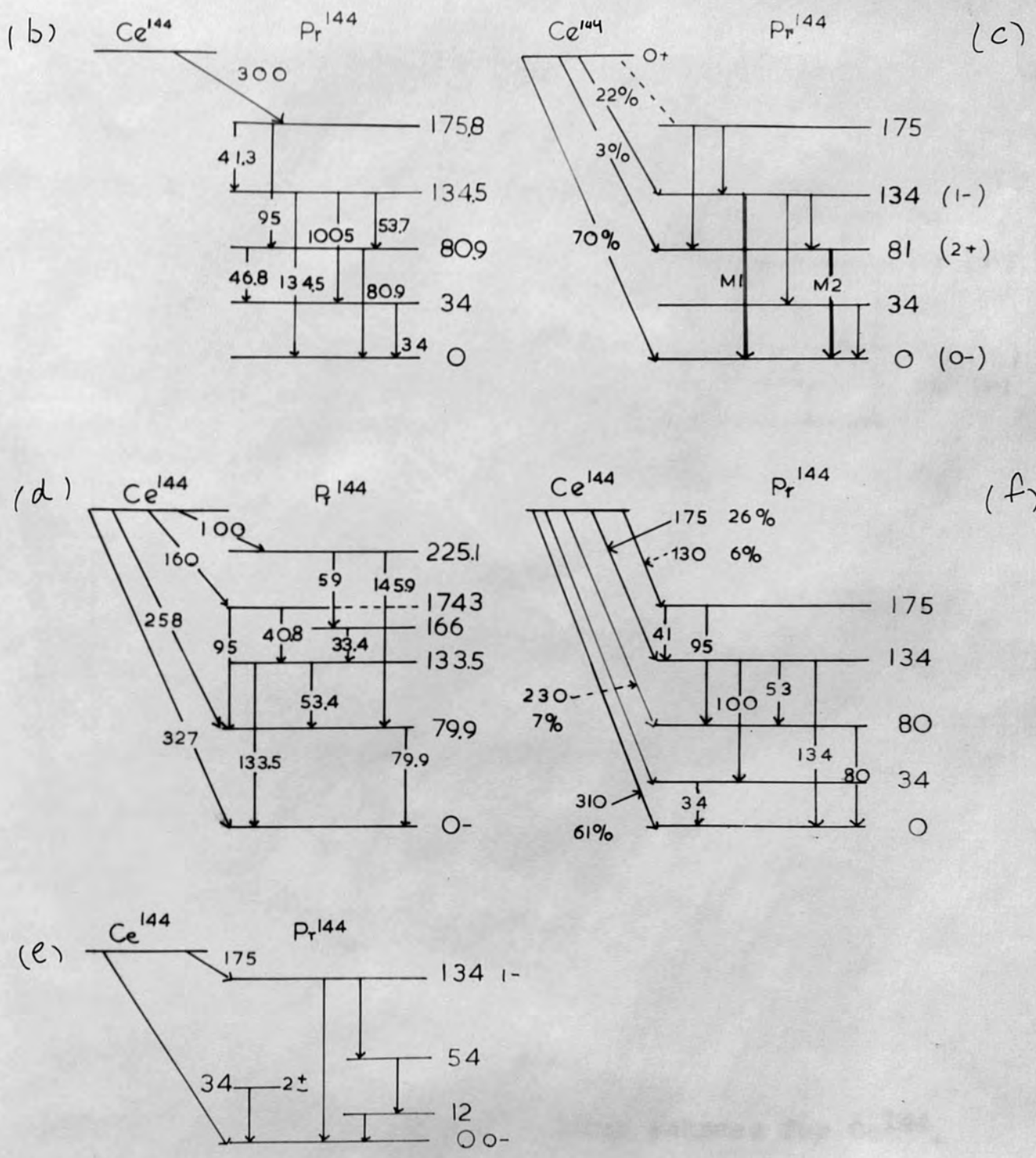
Fig. 1(i) Various suggested decay schemes for Ce[144].

(b) Keller and Cork (1951)
(c) Emmerich, Auth and Kurbatov (1954)
(d) Cork, Brice and Schmid (1954)
(e) Pullman and Axel (1956)
(f) Parfenova et al. (1957)
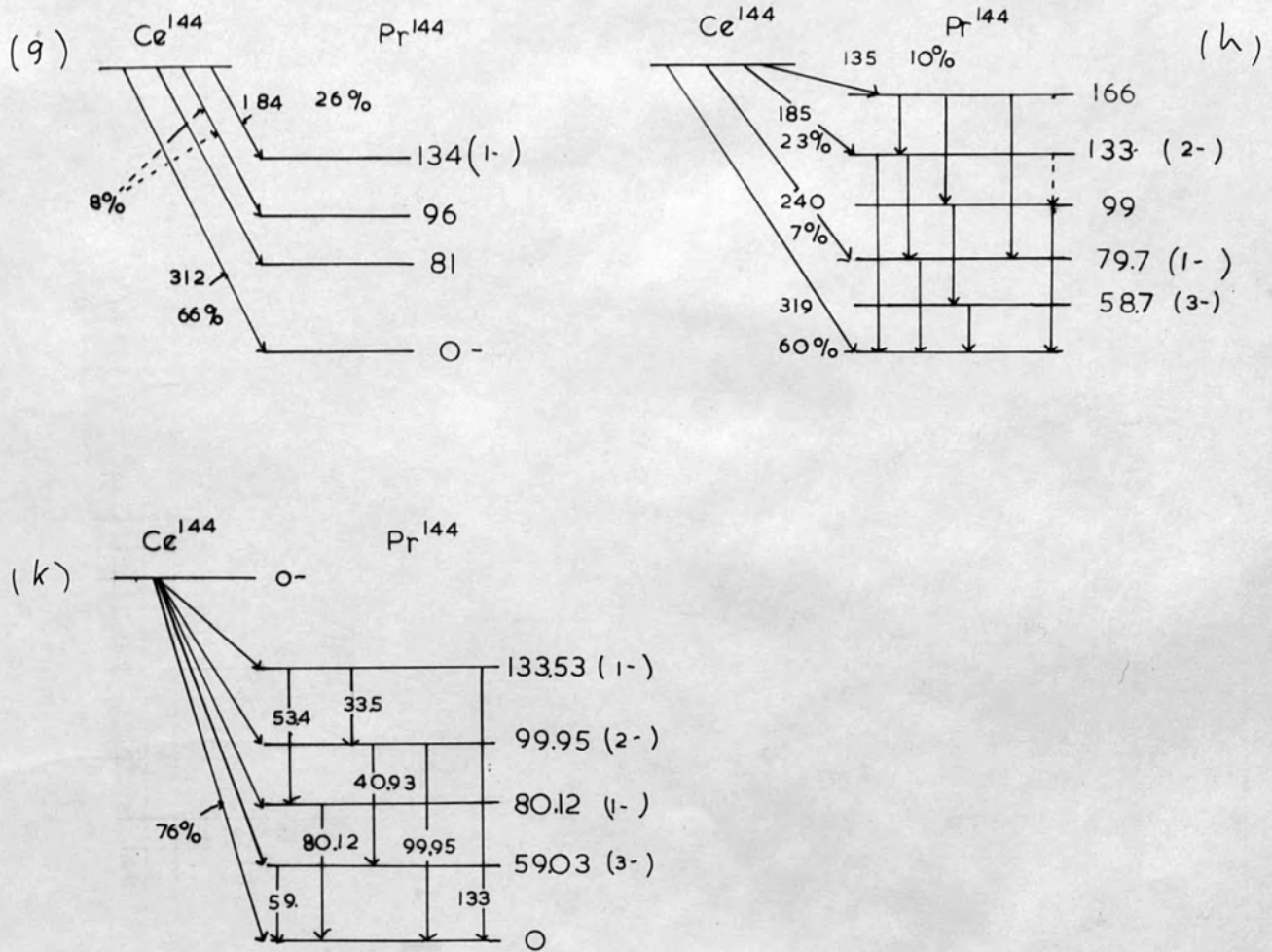
Fig. 1(ii). Various suggested decay schemes for Ce[144].

(g) Sengupta et al. (1959)
(h) Freeman (1959)
(k) Geiger et al. (1960)

Table I.

Gamma rays emitted in the isomeric transition of Pr[144] found by different investigators.

a		134	99.6	94.8	80		53	41	33	
b		134.5	100.5	95	80.9		53.7	41.3	34	46.8
c		134	100	94	81		53	41	34	
d	145.2	133.5		95	79.9	59	53.2	40.8	33.4	
e		134	100		81			42	34	12
f		134.1	100.6	94.7	81		53	41	33.7	
g		134		95	81	59	53	42	33	
h		133	99.3		79.7	58.8	53	40.5	33	86.5 66
i		134	100.6	94.7	80		53	41	35	
j			100			59				
k		133	99.95		80.12	59	53.41	40.93	33.5	

a. Emmerich, John and Kurbatov 1951 [1]

b. Keller and Cork 1951 [2]

c. Emmerich, Auth and Kurbatov 1954 [3]

d. Cork, Brice and Schmid 1954 [4]

e. Pullman and Axel 1956 [6]

f. Parfenova, Forafontov and Shipinel 1957 [7]

g. Sengupta et al. 1959 [9]

h. Freeman 1959 [10]

i. Forafontov and Sorokin 1959 [12]

j. Gnedich et al. 1959 [11]

k. Geiger, Graham and Ewan 1960 [13]

Table II.

Excited levels assigned to Pr^{144} to agree with gamma rays found in Table I.

References as
for Table I.

Levels

	225	175	166	133	99.9	95.9	80	59	54	34	12
a		175									
b		175		134.5			80.9			34	
c		175		134			81			34	
d	225	174	166	133			79				
e				134					54	34	12
f		175		134			80			34	
g				134		96	81				
h			166	133	99		79.7	58.7			
i		175									
k				133.5	99.95		80.12	59.03			

Pullman and Axel [6] , A.K. Sengupta et al. [9] and N.G. Geiger et al. [13] have not assigned a level above 133 keV (Table II). A gamma ray above this energy has been found by Cork et al. (1954) (Table I) only. However, in six of the works (Table II), a level at 175 keV was thought to exist and was thought necessary to explain the observed γ-ray data. Cork et al. (1954) and Freeman (1959) [10] have assigned a 166 keV level to the decay scheme of Pr^{144}. This means that the 133 level is fed by a β-decay of Ce^{144} and also by the 33 keV γ-ray and therefore, if this level exists, a 33 keV-133 keV cascade should be easily observable since both gamma rays are strong. In the present work an attempt was made to find this cascade by measuring $\bar{e} - \bar{e}$ coincidences between the K133 conversion line and $L_I 33$ conversion line.

β-β coincidence technique has many advantages over γ-γ and β-γ coincidence methods for investigating nuclear decay schemes. It becomes possible to make a unique assigment to nuclear energy levels even in complex decay schemes. This is due to the higher resolution in momentum of the β-spectrometer compared to the NaI (Tl) scintillation spectrometer. Plastic phosphors having a short decay time can be used so that the resolving time of the coincidence circuit can be reduced, thus decreasing the number of chance coincidences. Stronger sources can be used than in β-γ coincidence method without overloading one counter because the momentum selection takes place before

the particles reach the detector.

The β-β spectrometer was first introduced and used by N. Feather (1940, 1948) [20, 21] who used a permanent magnet pair of beta spectrometers and Geiger counters as detectors. This restricted the practical resolving time of the coincidence unit to a minimum of 2×10^{-7} sec because of the time lag between the entry of an ionizing particle and the appearance of the voltage pulse across the counter. A number of other beta coincidence spectrometers have been described [22-35]. Bell, Graham and Petch (1952) [25] used two short lens spectrometers for measuring short lifetimes. Bashandy [35] showed that instrumental errors could be considerably reduced by measuring lifetimes in this way. Gerholm who formulated the theory of β-β coincidences [31] has designed a β coincidence spectrometer with a 'triangular' field [30] which had a specially shaped light pipe to increase the efficiency of detection. More recently V.A. Sergienko [34] described a beta coincidence spectrometer consisting of long lens spectrometers. He was able to use a resolving time of the coincidence circuit of $4-5 \times 10^{-8}$ sec with Geiger counters and $1-2 \times 10^{-8}$ sec with scintillation detectors. The photomultipliers were placed in the vacuum chamber eliminating the necessity to use light pipes and he found that he could detect electrons to 5 keV. In the present work a large spheroidal field spectrometer [17, 36, 37] was used together with a short lens spectrometer.

A number of modifications were made to the large spectrometer before the small spectrometer was joined to it.

II

Modifications to the large spheroidal field spectrometer.

A number of modifications were made to the large
spheroidal field spectrometer, the design of which is based
on the theoretical magnetic field where the ~~lines~~ tubes of force
are prolate spheroids (Richardson 1949, ref. 36, see Part II),
in an attempt to improve the symmetry of the large spectro-
meter and thus the resolving power, and also the mechanical
motions, to make operation easier. A small lens spectrometer
was then joined to the large one for β-β coincidence measure-
ments (Fig. 3).

The arrangement of the baffles of the large and small
spectrometers is shown in Fig. 2. This is a radial section of
the baffles. The baffle system of the large spectrometer is
shown in Fig. 6 and that of the small spectrometer in Fig. 23a, b.
A detailed description and diagram of the large spectrometer
are given by P.R. Evans et al. [17] .

(i)   The ring slit.

An attempt was made to improve the slit opening mechanism.
The modified form is shown in Fig. 5. The width of the slit is
determined by the separation between ring 2 and 5 (Fig. 2, 5).
In Fig. 5 the slit is wider than in Fig. 2. The rings 4, 5 and
6 are in the same position with respect to the aluminium tank,
but the ring 2 and the sleeving 15 carrying it have moved to the

Key to Fig. 2 - Radial section of the baffle systems of the large and small spectrometers.

1. Aluminium tank.

2. Plate of slit assembly which moves only with the axial motion, i.e. with the sleeving 15.

3. Inner plate which has 4, 5, & 6 attached to it.

4. Back ring.

5. Middle ring, slit ring.

6. Front ring.

7. Iron bar.

8. Corner block.

9. Left hand iron plate.

10. Hole in left hand iron plate for the nonmagnetic stainless steel tension studs which hold the left hand end plate.

11. Left hand aluminium plate.

12. Brass tube surrounding the light pipe.

13. Mask.

14. Crystal of large spectrometer.

15. Sleeving carrying slit assembly.

16. Central (axial) tube of large spectrometer.

17. Fixed baffle - the baffle is fixed to the axial tube. In the axial motion the slit assembly moves with respect to the baffle. It has three brass bars screwed to it. These determine the position of the axial tube with respect to the tank.

18. Lead block.

19. Sleeving of the angle defining baffle (angle baffle).

20. Ring of angle baffle attached to 19.

21. Inner ring of angle baffle.)
39. Outer ring of angle baffle.) Joined by four rods at 90°.

22. Small lead block.

23. Right hand aluminium plate (disc).

24. Right hand bevelled iron disc.

25. Pumping hole.

26. Angle defining baffle of small spectrometer.

27. Inner moving part of angle baffle.

28. Ring of angle baffle screwed to the iron of the spectrometer.

29. Large lead block of small spectrometer.

30. Moving disc of ring slit.

31. Outer ring of ring slit.

32. Inner disc of fixed section of ring slit.)
33. Outer disc of fixed section of ring slit.) Spider.

34. Iron of small spectrometer.

35. Brass plate with two clearance holes and one 1/2" screw to take stainless steel rod.

36. Stainless steel rod.

37. Brass cylinder - has entry to pumping line and source vacuum gate.

38. Aluminium plate.

39. See 21.

40. Right hand 'cooling' ring.

41. Left hand 'cooling' ring.

42. Control rod for angle defining baffle.

43. Pole piece.

44. Small crystal of small spectrometer.

45. Light guide of small spectrometer.

46. Photomultiplier of small spectrometer.

47. Brass cylinder.

48. Brass end plate.

49. Iron shield which can slide so as to expose the contact between the light pipe and the photomultiplier.

50. Brass tube holding the photomultiplier.

Fig. 2 Radial section of the baffle systems of the large and small spectrometers
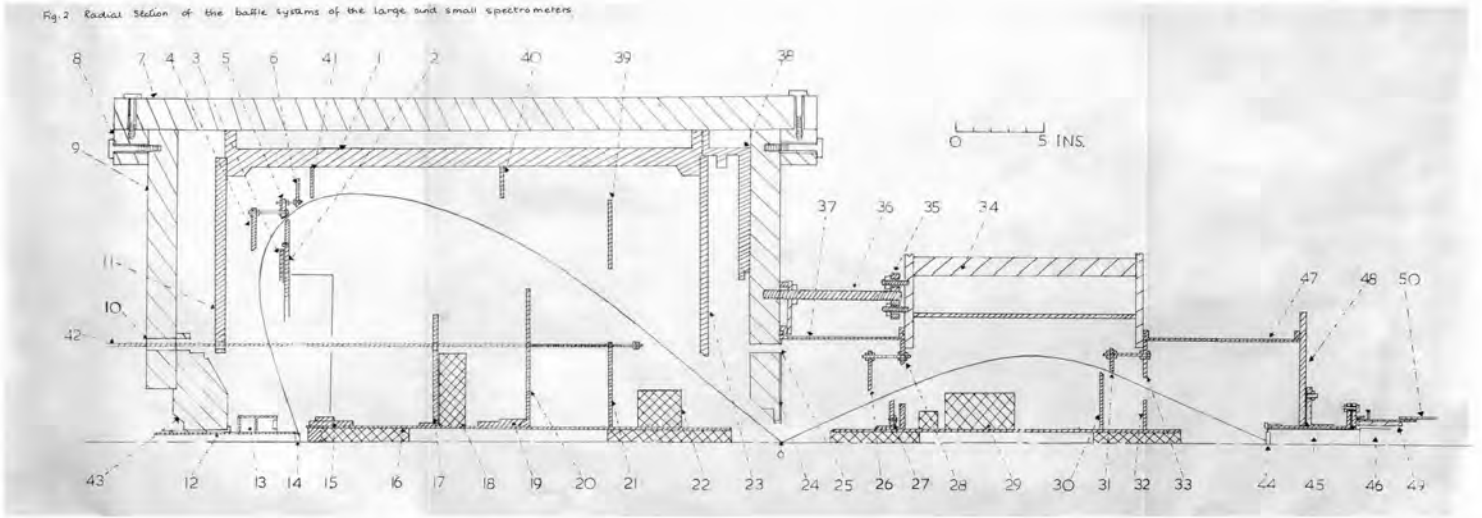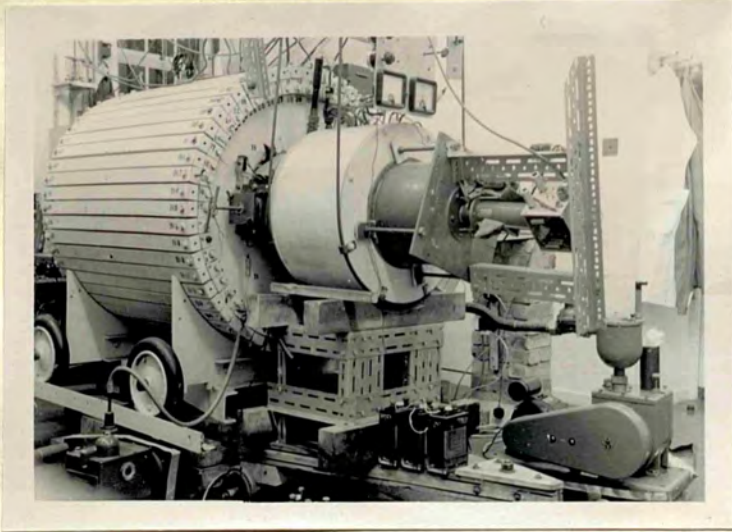
Fig. 3. The large and small spectrometers. The sliding vacuum gate and the handle of the sourceholder can be seen at the centre of the photograph.
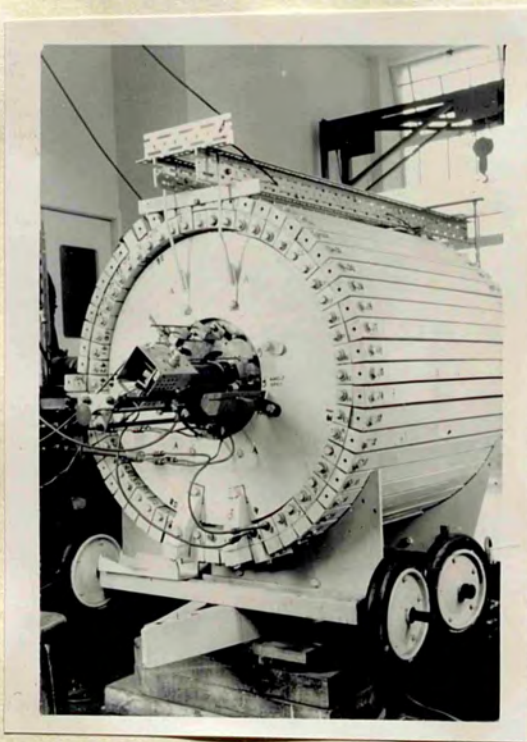
Fig. 4. View of the end of the large spectrometer showing the photomultiplier and the control rods with the revolution counters for changing the position of the baffles.

Key to Fig. 5 - Modified mechanism for opening the slit of the large spectrometer.

A. One of three screw threads which determine the separation between 2 and 3.

B. One of three sprockets carrying the chain which transmits the rotation to other screw threads such as A so that the slit opens uniformly.

C. Gear driven by D through chain and sprockets H.

D. Coupling of control rod to gear, pin sliding in slot (can be seen in lower left hand corner of Fig. 7).

E. Gear transmitting motion of G to thread F.

F. Threaded rod which determines the separation between 15 and 17, when rotated, 15 moves towards or away from 17.

G. Control rod for axial motion.

H. Two sprockets and chain transmitting the rotation of D to C.

J. Gear which is rotated by C. B rotates with it.

Numbers are the same as those in Fig. 2.
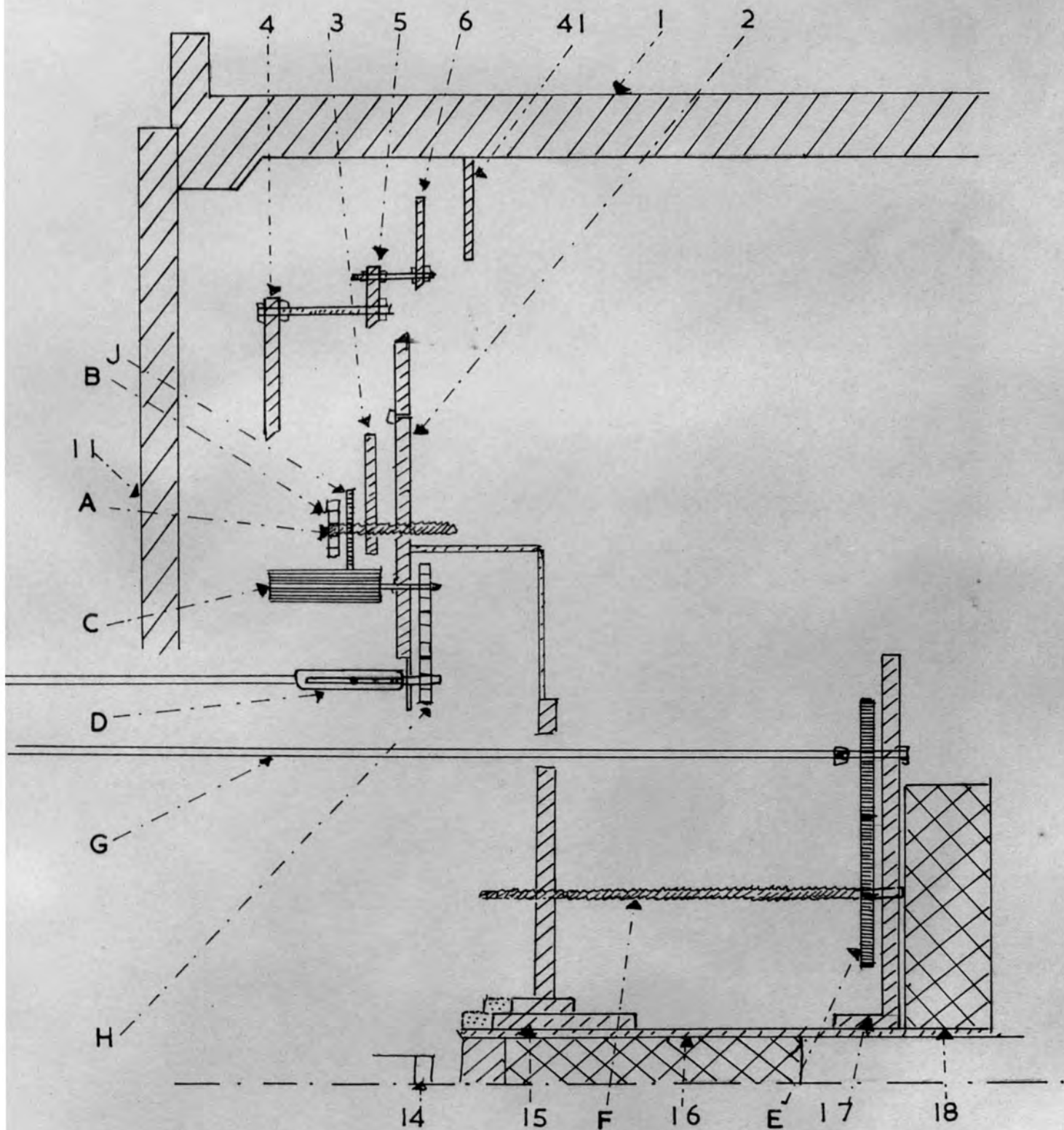
Fig. 5. Modified mechanism for opening the slit of the large spectrometer.
The slit is wider than in Fig. 2. The baffles 3, 4, 5, 6, are in the same position with respect to the tank as in Fig. 2 but the sleeving 15 and therefore the ring 2 which is attached to it has moved to the right. The previous position of the sleeving is dotted.

right, i.e. towards the source. 4, 5, 6 must always remain
on the caustic of the electron trajectories.

To open the slit, the whole assembly consisting of the
rings 2, 3, 4, 5, 6 is moved towards the source by rotating
the rod G. The rotation of the rod G is transmitted through
the plain gears E to the thread F. When this rotates it draws
the sleeving 15 and thus the rings 2, 3, 4, 5, 6 towards the
baffle 17 which is fixed. 4, 5, 6 must now return by moving
an equal amount in the opposite direction, i.e. to the left.
If 2 is now stationary, this can be achieved by varying the
separation between 2 and 3 which is attached to the rings 4,
5, 6. This is done by turning the rod D in the appropriate
direction. The rotation of the rod D is transmitted to the
gear C by the chain and sprocket H. The gear C rotates the
gear J, the sprocket B and the thread A. As the thread A
rotates, the separation between 2 and 5 increases and the slit
is opened. The net result of the two operations above is that
4, 5, 6 are in their original position and the separation
between 2 and 5 has increased because 2 has moved to the right.
There are three sprockets and threads such as A and B at 120°
so that the slit opens uniformly and the motion of A and B is
transmitted to the other threads by a chain which can be seen
clearly in Fig. 7. The slit can also be opened by reversing
the order of the above operations. The gear reduction ratios
(3:1), and the threads A and F (Fig. 5) for the two motions
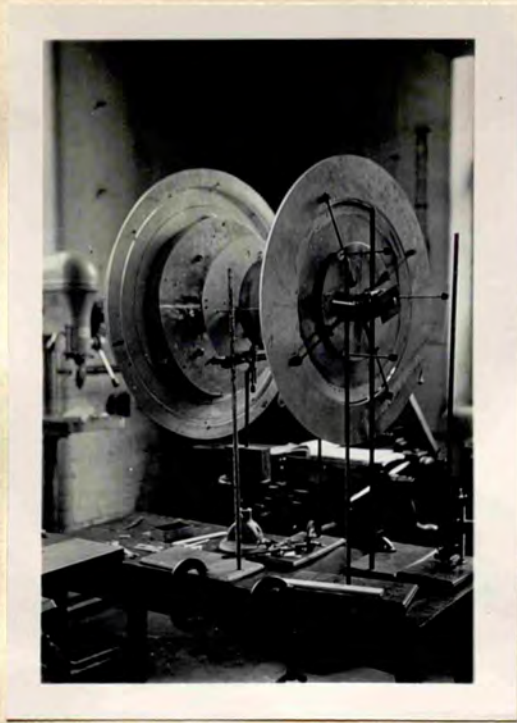
Fig. 6. The baffle system of the large spectrometer mounted on the central tube for alignment and centralising. The ring slit is on the left and the closed angle baffle on the right. The lead block can just be seen in the middle. The fixed baffle 17 has a thick pillar screwed to it. This rests on the bottom of the tank and is one of the supports for the baffle system. Here it is seen supported by the rising table.

Fig. 7. Side of the ring slit which faces the pole piece in the spectrometer, set up for centralising the baffles. The face plate at the centre has been fixed perpendicular to the central tube by a rod that passes right through the axial tube. It was used for centralising only. The straight edge A which is almost vertical was used for adjusting the ring 3 and the rings of the slit. The three bars attaching the ring 3 to the rings 4, 5, 6, Fig. 2, can be seen. They have a small sprocket at the inner edge. The square plate at the centre is attached to the sleeving 15 Fig. 2 which carries the slit assembly.

control rod for axial motion

A

control rod for angle baffle
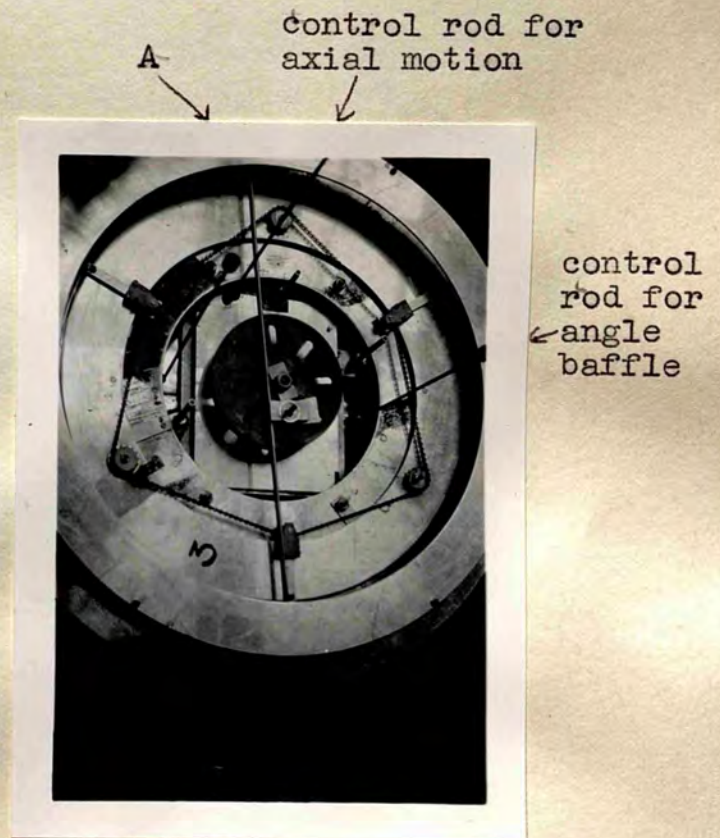
(axial motion of slit assembly along the axis and slit opening)
were made equal so that the rods controlling the motions have
to be rotated the same number of revolutions but in opposite
directions and could be coupled externally. To improve the
slit opening mechanism, Teflon impregnated copper bearings
were used and the existing Meccano chain and sprockets (A and H,
Fig. 5) were replaced by a heavier chain and sprockets seen in
Fig. 7.

Three stops at 120° were placed between the rings 2
and 3 to prevent their relative motion when the slit is shut.
These can also be seen in Fig. 7.

The control rods for centering the rings of the slit
with respect to the field and that for opening the slit were
coupled to the slit assembly by pins sliding in slots such
as D, Fig. 5 (shown in Fig. 7), in order to prevent the control
rods sliding through the O ring seal when the slit is centralized
and opened during operation. This reduces the wear on the O
rings and the possibility of causing a leak. The couplings
with the rods removed can be seen in Fig. 7.

Each control rod passes through an O ring seal and one
of the stainless steel tension studs which screw into the bronze
ring firmly attached to the left aluminium ring 11 (Fig. 2 and 5).
The seal is shown in Fig. 8. It was difficult to change these
O rings because it was difficult to grip and remove the collar
(Fig. 8 and 9) pressing on the O ring. Small (10 BA) threaded
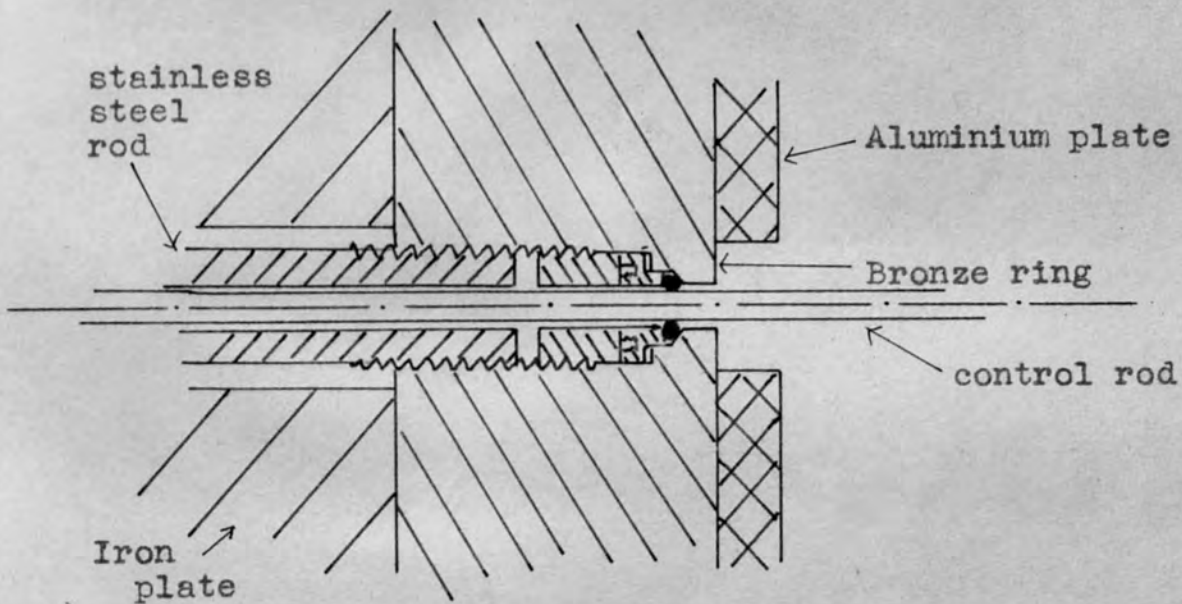
Fig. 8. Diagram showing the vacuum seal for the control rods.
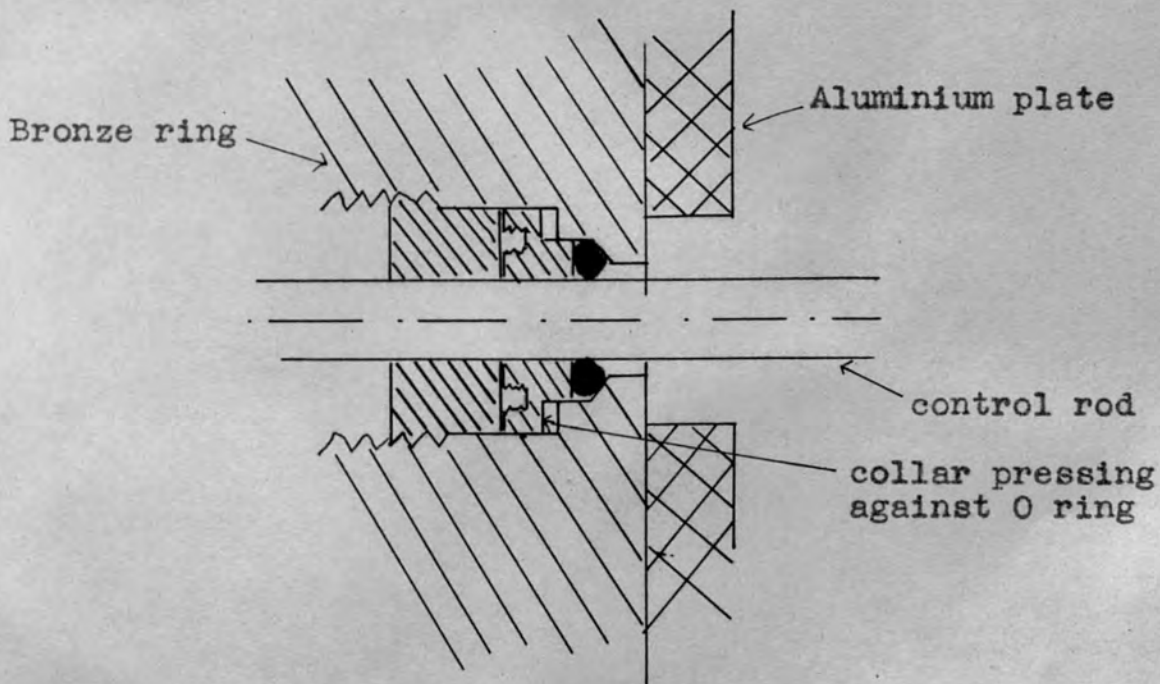
Fig. 9. Portion of Fig. 8 enlarged showing the O ring and collar with the threaded holes.

holes were made in these collars so that they could be removed easily by pulling them out with a long threaded rod. These can be seen in Fig. 9 which is an enlarged version of the seal in Fig. 8.

Revolution counters to count the revolutions of the control rod were attached to the stainless steel tension studs mentioned earlier by methods shown in Fig. 14. The counters were set in such a way that the rings 4, 5, 6 are automatically stationary with respect to the field when the slit is opened and shut and when the readings on the counters for the slit opening and axial motion are the same.

(ii) Baffle 41 (Fig. 2).

The new position of the baffle is shown in Fig. 2 and 5. It must be firmly fixed in the tank so that it cannot be pushed out of position easily by the baffles 4, 5, 6 as the slit is opened and shut even though the danger of this happening is small because the baffles 4, 5, 6 should remain stationary. The method shown in Fig. 13 was used. The ring was cut along one radius and a plate with slots was screwed to it. As the nut of the countersunk screw at the centre of the plate A is tightened the bevelled head slides into the countersunk portion of the ring which expands and fits very tightly into the tank.

(iii) Angle defining baffle.

This consists of the rings 20, 21, 39 (Fig. 2). It is
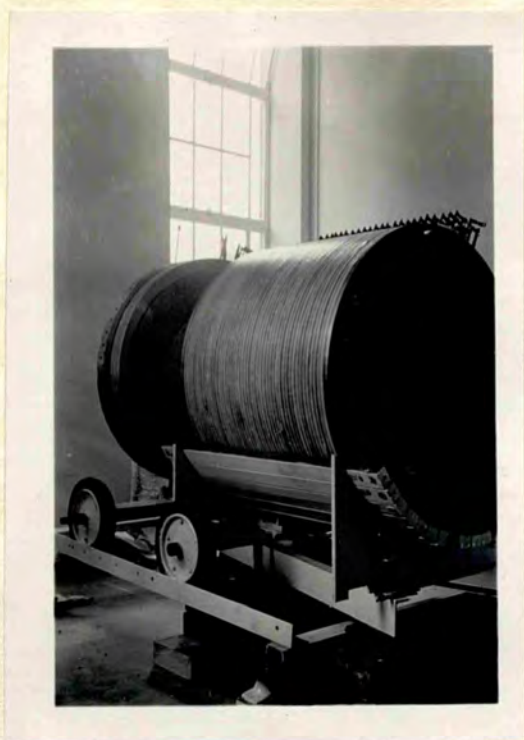
Fig. 10. The aluminium tank 1 of the large spectrometer. Some of the numbered iron bars can be seen on the cradle under the tank. The electrical connections can be seen at the top.

Fig. 11. The right hand end plate. Note the bevelled hole and bush at the centre of the iron plate, the pumping holes and bracket for the rotating coil.

Fig. 12. The left hand end plate showing the pole piece. The crystal is withdrawn into the hole at the centre for protection. The corner blocks with the holes are on the left.
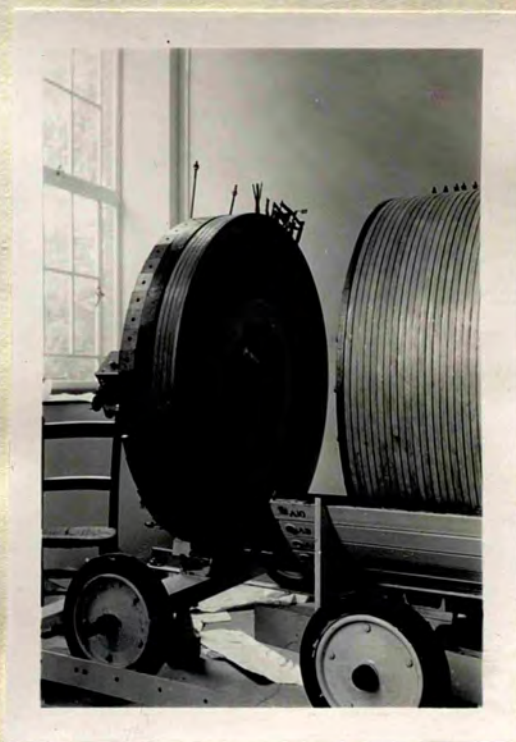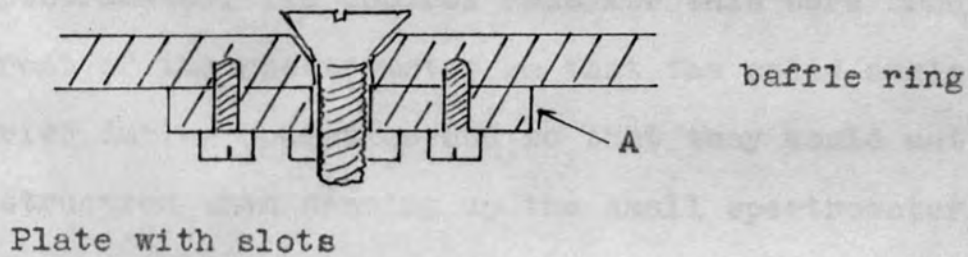
Fig. 13. Method used for fixing the baffle 41.
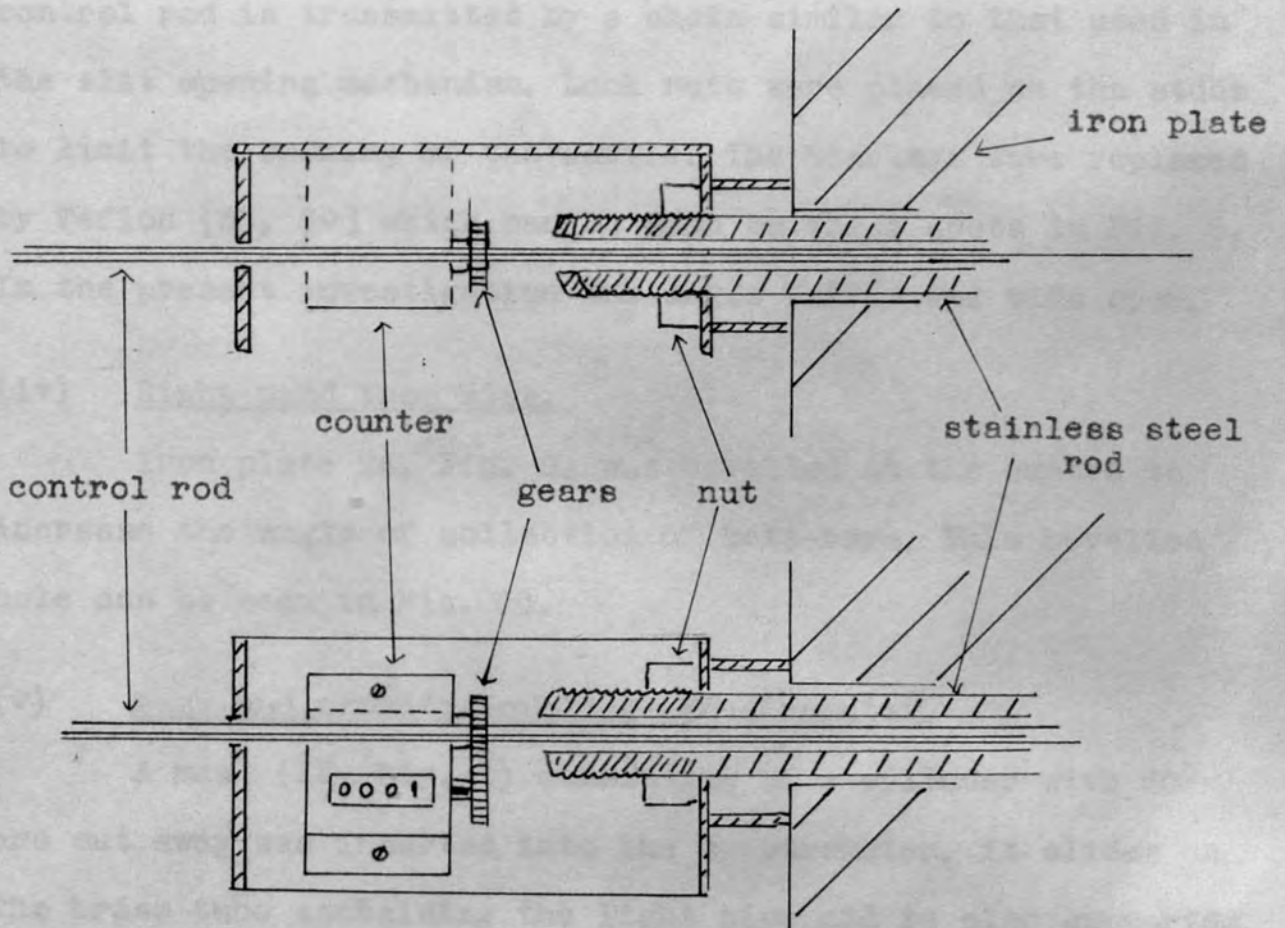
Fig. 14. Holder for revolution counter to count the revolutions of the control rods (a modification of this was used for the angle baffle where the counter can slide as the rods move in and out).

used for selecting the solid angle of the β-rays accepted by
the spectrometer. The control rods for this were brought to
the front of the spectrometer so that the solid angle could
be varied during operation and so that they would not cause
an obstruction when drawing up the small spectrometer. It is
opened by rotating one threaded control rod. There are three
studs (Fig. 6) and sprockets at 120° and the rotation of the
control rod is transmitted by a chain similar to that used in
the slit opening mechanism. Lock nuts were placed on the studs
to limit the opening of the baffle. The bearings were replaced
by Teflon [38, 39] which can be seen as white spots in Fig. 6.
In the present investigation the angle baffle was wide open.

(iv)   <u>Right hand iron disc.</u>

Iron plate 24, Fig. 2, was bevelled at the centre to
increase the angle of collection of beta-rays. This bevelled
hole can be seen in Fig. 11.

(v)   <u>Mask and symmetry of large spectrometer.</u>

A mask (13, Fig. 1) consisting of a cylinder with 60°
arc cut away was inserted into the spectrometer. It slides on
the brass tube containing the light pipe and is also supported
by its two control rods. It can be moved over the crystal so
that only the beta-rays in a 60° sector are counted. The
symmetry of the spectrometer can be tested by measuring the
counting rate with the rotation of the mask (Chapter IV). In
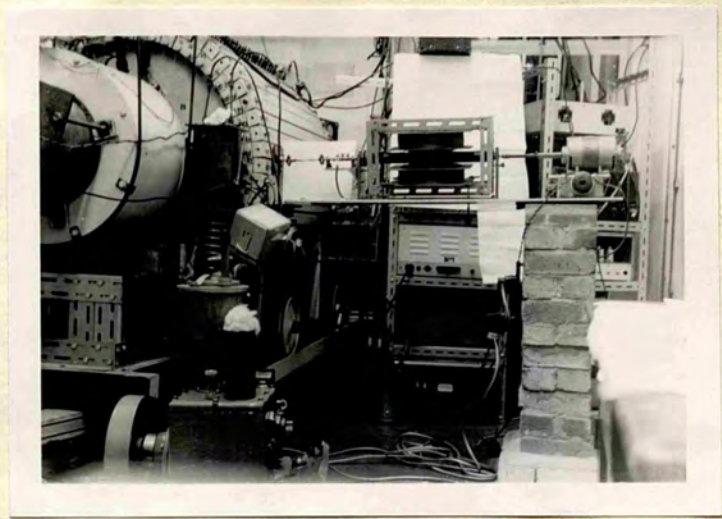
Fig. 15. Rotating coil for measurement of the field
in the large spectrometer. The motor is supported
on a brick pillar to reduce vibration of the shaft.
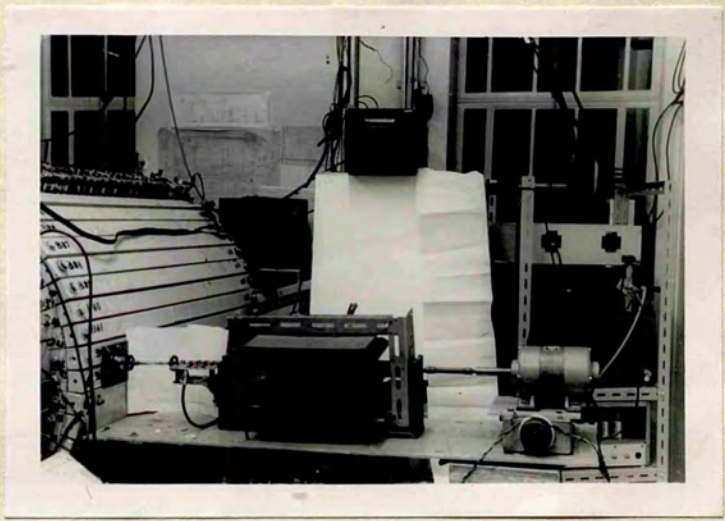
Fig. 16. View of rotating coil showing the bearing at
the entry to the spectrometer, the slip rings and the
Helmholtz coils for producing the reference field.

reference 17, 37 it was found that there was some asymmetry
in the spectrometer, which may have been due to the fact that
the iron bars near the electrical connections were further
from the axis than the others. An attempt was made to correct
this by inserting soft iron shims between the corner blocks 8
and iron bars 7, Fig. 2, to bring all the bars to the radius
of those near the electrical connections.

(vi)   Source changing.

It was difficult to change the source because the window
in the cylinder 37 is small and therefore the illumination poor.
A mirror and lamp were attached to the centering cross of the
cylinder 37. The lamp inside the spectrometer was run from a
4 V accumulator. One of the electrical leads passes into the
vacuum through a glass seal and the spectrometer is used for
the return path (the switch of the lamp is above the handle of
the source holder in Fig. 3).

(vii)   Field measurement in large spectrometer.

The method of measuring the field was similar to that
described by Hedgran (1952) [40, 41]. The method consists in
the comparison of the e.m.f. induced in a coil rotating in the
field (generator principle) with that induced in a coil rotating
in a reference field. The coil connections are shown in Fig. 20.
The rotating coils and the Helmholtz coils producing the reference
field are shown in Fig. 15 and 16. Either of the sets of coils

Fig. 17a. Circuit diagram of one stage of the selective amplifier tuned to 25 c/s.

Fig. 17b. Circuit for coupling the two stages of the amplifier.
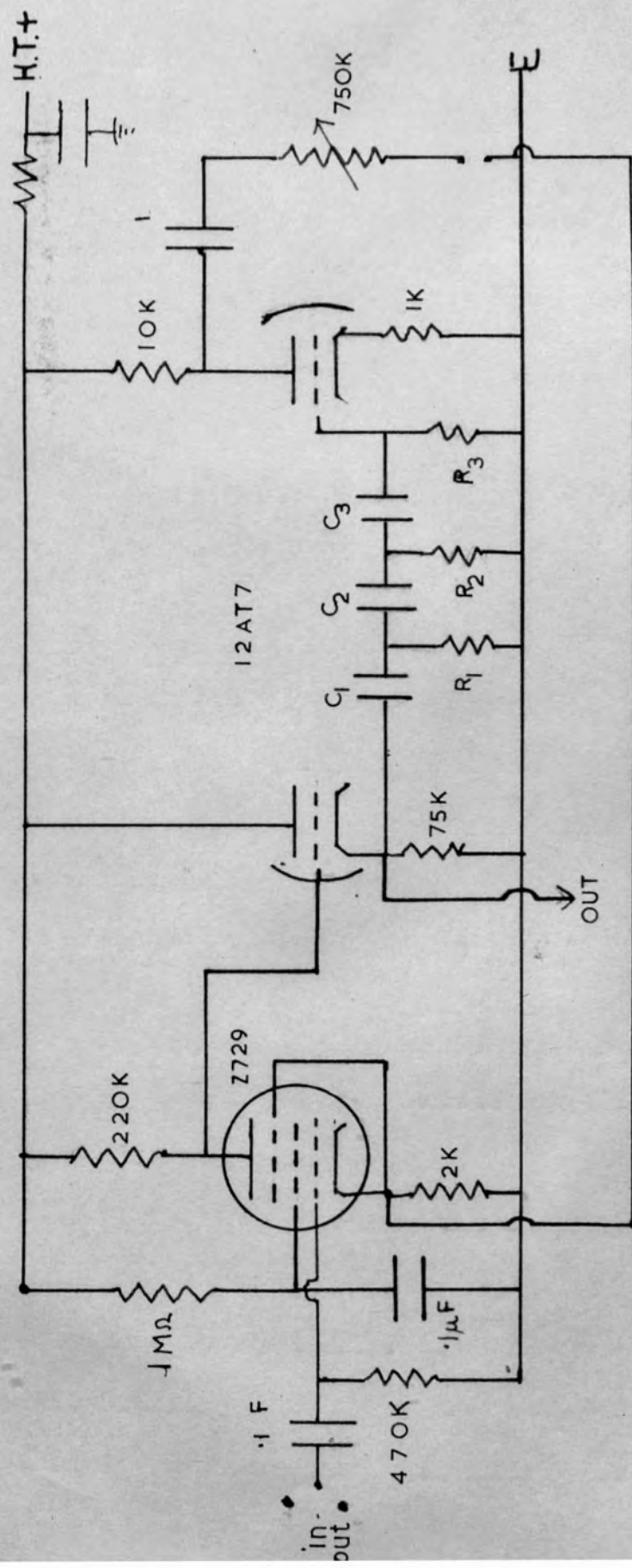
Fig 17a.

$C_1 = C_2 = C_3 = \cdot1\,\mu F$

$R_1 = R_2 = R_3$ 0-50 K

on one spindle

Colvern ganged potentiometer
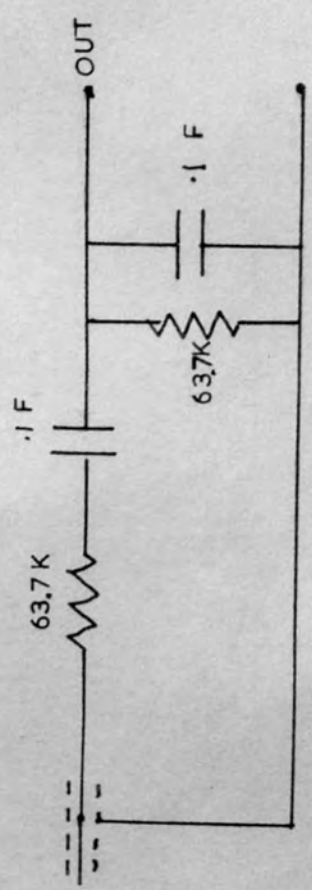
Fig. 17 b.
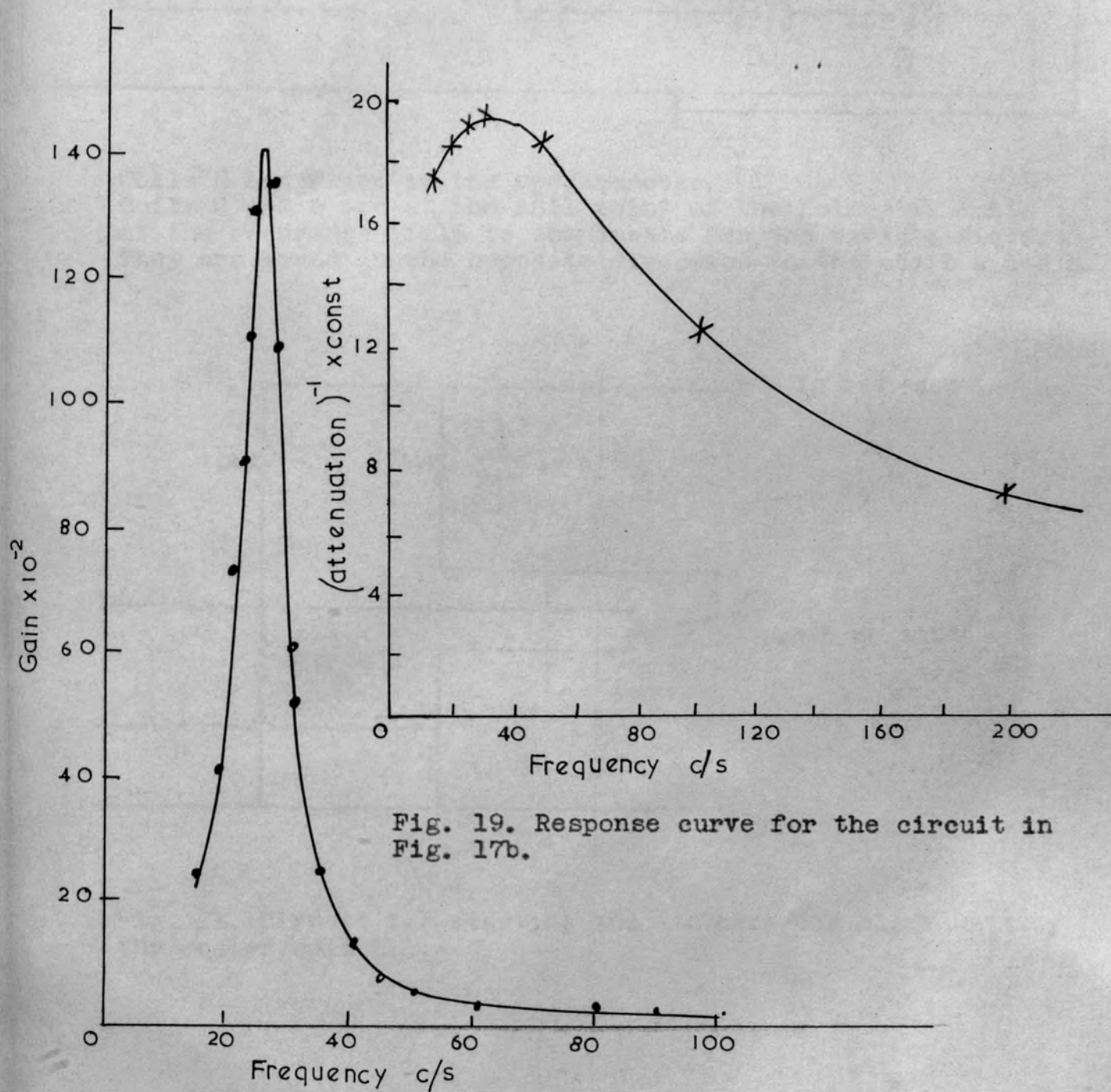
Fig. 19. Response curve for the circuit in
Fig. 17b.

Fig. 18. Response curve for the two-stage amplifier tuned to
25 c/s.

Fig. 20. Connections to the spinning coils for measuring the magnetic field in the large spectrometer.
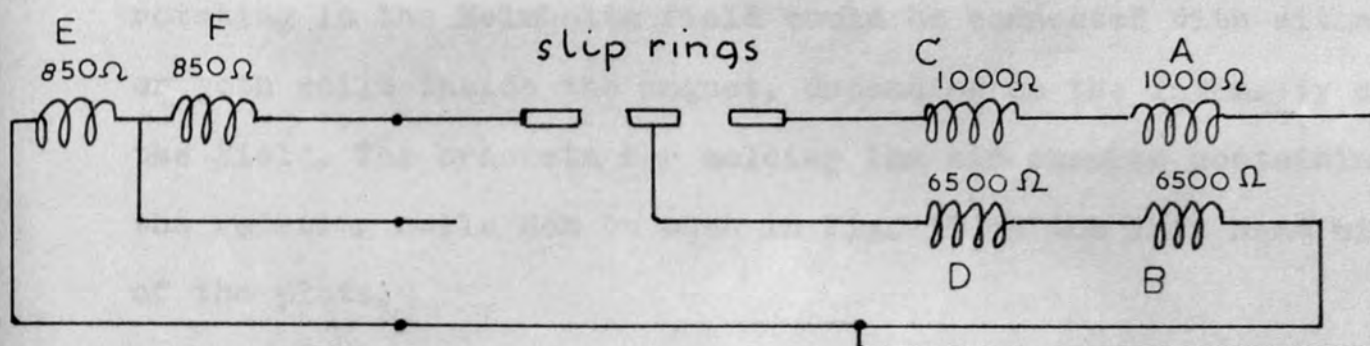
Coils E and F are in the spectrometer.
Coils C and D are at the null point of the Helmholtz coils
of the reference field to compensate for the earth's field.
They are wound in the opposite direction to the coils A and B.
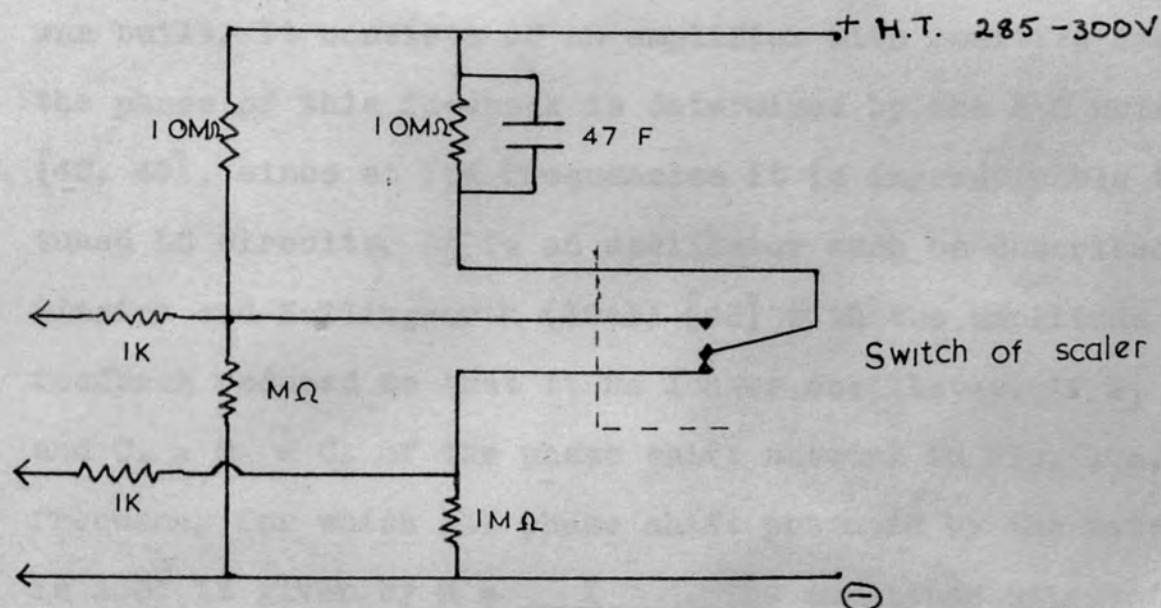
Fig. 21. Circuit for starting and stopping the clock unit by the scaler switch.

rotating in the Helmholtz field could be connected with either or both coils inside the magnet, depending on the intensity of the field. The brackets for holding the air chamber containing the rotating coils can be seen in Fig. 11 on the left hand side of the plate.

A synchronous motor with a speed of 1500 rpm was used to replace the squirrel cage motor to make the mains pick up constant and improve the accuracy of the balance between the e.m.f. induced by the spectrometer and Helmholtz fields. An amplifier tuned to 25 c/s to match the rotation of the motor was built. It consists of an amplifier with positive feed back; the phase of this feedback is determined by the R C network [42, 43], since at low frequencies it is impracticable to use tuned LC circuits. It is an oscillator such as described by Ginzton and Hollingworth (1941) [43] with the amplitude of the feedback reduced so that it no longer oscillates. If $R_1 = R_2 = R_3$ and $C_1 = C_2 = C_3$ of the phase shift network in Fig. 17a, the frequency for which the phase shift produced by the network is 180° is given by $n = \dfrac{1}{2\pi RC\sqrt{6}}$. The amplitude attenuation produced by the network is 29. Therefore, provided the feedback is sufficiently low, the amplifier will have a maximum gain at a frequency when the phase shift is 180°.

The amplifier built consisted of two stages of the type shown in Fig. 17a coupled by the circuit shown in Fig. 17b.

Fig. 22. The small spectrometer being slightly raised for bringing up to the large spectrometer. Two pairs of short studs used for drawing the two spectrometers together can be seen on the upper part of the iron plate.

The baffle system of the small spectrometer

ring
slit
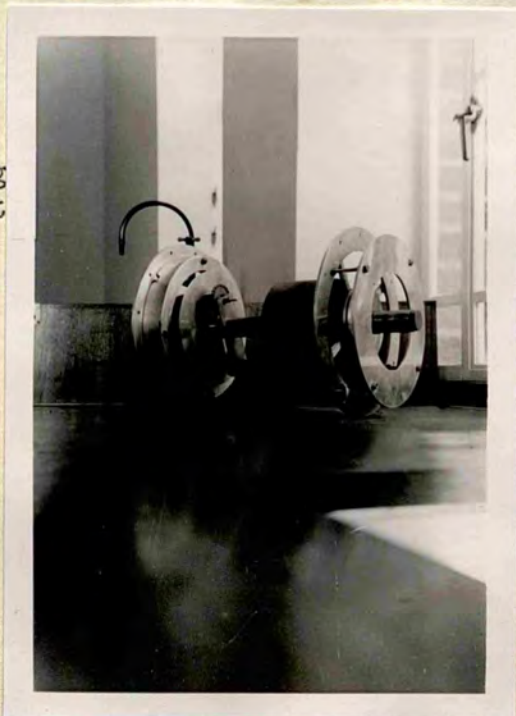
angle
baffle

Fig. 23 a.

ring
slit

angle
baffle

Fig. 23 b.

This is also selective since it has a minimum attenuation of 3.9 in the region of 25 c/s. The curve of (attenuation)$^{-1}$ against frequency for this is shown in Fig. 19.

The response curve of the 2-stage amplifier driven from H.T. dry batteries and accumulators is shown in Fig. 18. The noise limited the accuracy of the field measured to a little better than $1:10^3$.

(viii) Counting equipment.

A Philips preset count unit PW 4052 was attached to the Dynatron scaler. The clock and scaler were stopped by the switch of the scaler. There was no pulse given out by the latter at the special connections at the rear for operating external equipment and therefore the special circuit in Fig. 21 was used. It was suggested by Philips who used this in their own scaler for the same purpose. The timer was supplied with an extra amplifier to amplify the output pulses from the Dekatron, so that the timer was stopped after a preset number of counts, on the assumption that the output pulse was small. Many spurious pulses were produced and it was found that the output pulses of the Dekatron were too long and had an amplitude of 30 V. Therefore the amplifier was removed and the pulse was differentiated.

(ix) Small spectrometer.

The small spectrometer was attached to the large spectrometer by four nonmagnetic stainless steel bars. One of these and

Fig. 24. The ring slit of the small spectrometer, the slit is closed in both photographs.
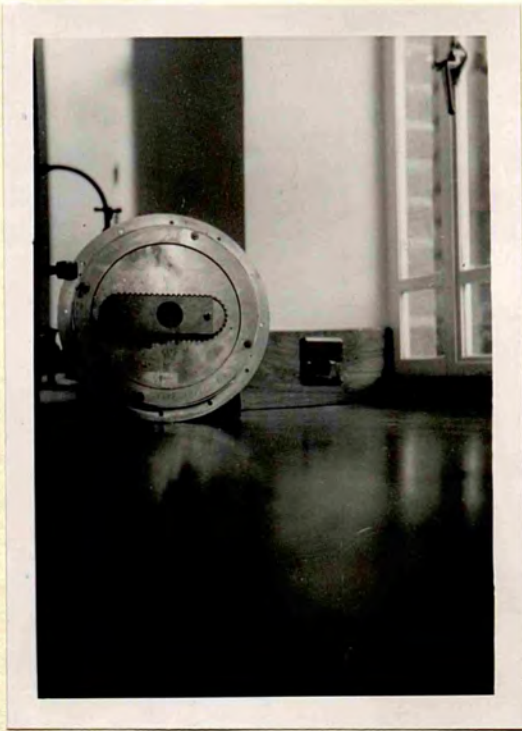
a. View showing chain drive
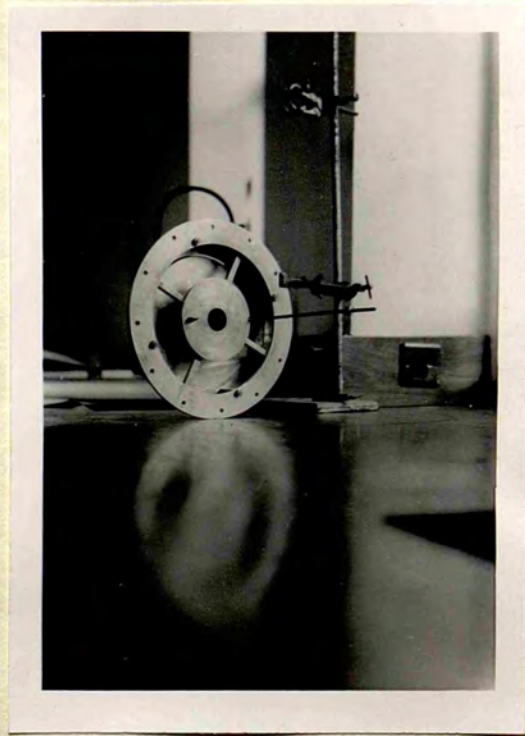
b. View showing spider and control rod for opening the slit.

the method of attachment is shown in Fig. 2. Each stainless

steel rod (one shown in Fig. 2, 36) was screwed into the iron

plate 24 of the large spectrometer. Two pieces of brass studding

were screwed into the iron of the small spectrometer (two pairs

of these can be seen in Fig. 22). When the two spectrometers

were brought together, the studs passed through holes in a

small brass plate 36 (Fig. 2) which was screwed into the stain-

less steel rods already on the large spectrometer. Nuts were

then placed on the studs to secure the plate and then tightened

to pull the two spectrometers together. The baffle system of

the small spectrometer is shown in Fig. 23a, b. The bearings

on the ring slit were also replaced by Teflon.

Both spectrometers have a common vacuum chamber which

is pumped by the oil diffusion pump and rotary pump previously

used for the large spectrometer. The pressure finally attained,

measured by a Penning gauge, was well below 5×10^{-5} mm Hg.

III

Preparation of thin sources.

(i)   Introduction.

The preparation of thin sources [49] on thin backings
is of great importance in β-spectroscopy because backscattering
and loss of energy of the electrons in the source gives rise to
an increased number of low energy electrons in the β-spectrum.
This distortion in the spectrum may be erroneously interpreted
in the spectrum analysis as a low energy β-component. The source
thickness is not so critical when the high energy portion of the
spectrum is investigated and when conversion lines are studied,
although the effect shows up in the broadening of the lines at
low energies.

Several methods of preparing thin sources were tried,
and finally the method of ion ejection from a capillary tube,
first suggested by Carswell and Milsted [51], was developed and
used.

(ii).   Drop method.

Early measurements with a thin source were made using
a source prepared by the drop method. A drop of dilute insulin
[50a, 50b] was applied to the centre of an aluminium film
0.25 mg/cm^2 strengthened by a VYNS film [47] stretched over
the source ring, and the excess was removed with a pipette.
(The thickness of the VYNS film was measured with a Michelson

interferometer and was found to be $< 1/2 \lambda$). ThB collected

on a thin platinum wire was dissolved in dilute nitric acid.

Nitric acid was chosen because hydrochloric acid even in very

dilute form attacked the aluminium foil. A drop of the radio-

active solution was then dropped onto the film. A resolution

of 1.5% to 2.4% was obtained for the ThB F line compared to

0.6% obtained under the same conditions with a 2 mm source

on a platinum button showing that the sources were different

on different occasions and were larger than the initial drop

of insulin. With a Ce^{144} source prepared in this way the re-

solution of the K133 conversion line (electron energy 91 keV)

was 2.7%, again suggesting that the liquid spread probably

by capillary action. Since the spread could not be observed

visually, the liquid probably spread between the VYNS and

aluminium. Closing the slit or masking a portion of the crystal

with the mask [Chapter IV] produced no improvement and therefore

it was concluded that the width of the line was due to the

source. The source holder also became contaminated confirming

this.

To eliminate any gap between the aluminium and VYNS

film, an aluminium film was evaporated onto the film [47, 48].

The appearance of VYNS changed probably as a result of the atomic

bombardment of the film by aluminium atoms. It became more

elastic and had many wrinkles. Dilute nitric acid attacked

the aluminium film whether it was applied on the aluminized

side of the film or the uncoated side of the VYNS, probably
because the VYNS was affected and because the aluminium had
no protective oxide layer.

(iii) Ion ejection from a capillary tube.

This method, first suggested by Carswell and Milsted
1954, was developed and used for making ThB and Ce^{144} sources.
With the source prepared in this way the resolution for the
ThB F line obtained with a ~5 mm source was 0.69% compared *which* *favourably*
with a 2 mm button taken under the same conditions (slit 12
turns open) and it was 0.8% with the slit more than twice as
wide (30 turns).

The apparatus used is shown in Fig. 25. The effect of
the shape of the tube and type of liquid which gave the most
satisfactory results were investigated with the object in mind
of preparing a Ce^{144} source.

The source ring with the aluminium film and VYNS backing
was placed on the machined earthed brass plate. This was then
enclosed in a Perspex box with a lid, the hole in which was
machined to be coaxial with the centre of the source ring. The
capillary tube was gripped by a clip which rested on the Perspex
lid.

The high voltage was applied to one end of the wire
inserted into the capillary tube. The voltage was measured
by the current flowing in the 100 MΩ resistor which consisted

of 100 1 M Ω high stability resistors carefully soldered together so that there were no sharp points at any of the soldered joints [54] . Any sharp points gave rise to corona discharge which could be seen in the dark and could be detected by the hiss produced. The resistors were supported by a Perspex frame.

(iii a) <u>Effect of the shape of the tube.</u>

The effect of the shape of the tube and the wire on the process of ejection was investigated by observing the liquid at the tip of the tube with a microscope and by noting the current in the galvanometer connected in series with the liquid. It was found that the current flowing in the galvanometer was directly related to the type of deposit obtained and behaviour of the liquid at the tip of the tube. The tip as seen in the microscope is shown in Fig. 26.

Capillary tubes with an internal diameter 1 mm were drawn out so that various tips were obtained. 44 S.W.G. (0.082 cm diameter) tungsten wire was used for the initial investigation and later replaced by platinum and Pt-Ir wire [47a]. The tips of some of the tubes had an internal diameter up to 2 times the diameter of the wire and some less than $\sim$0.060 cm diameter. The quantity of liquid held in the capillary when the gravitational forces are in equilibrium with surface tension forces was much greater than could be tolerated in this method. As the field was applied, the discharge was not steady but the liquid

Fig. 25. Diagram of the apparatus used for preparing sources by ion ejection from a capillary tube.
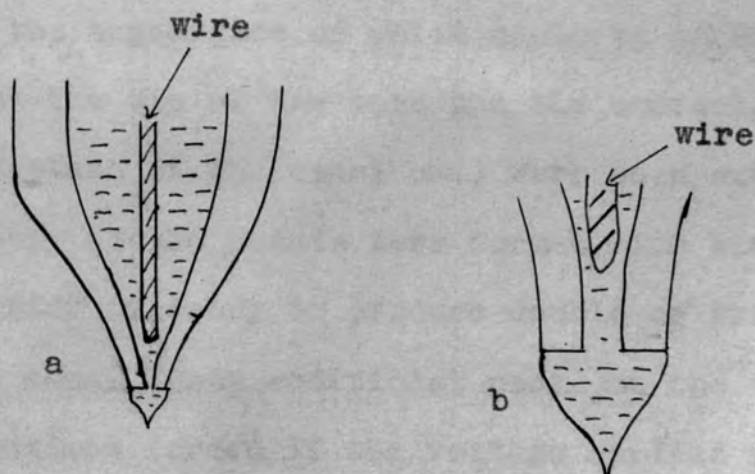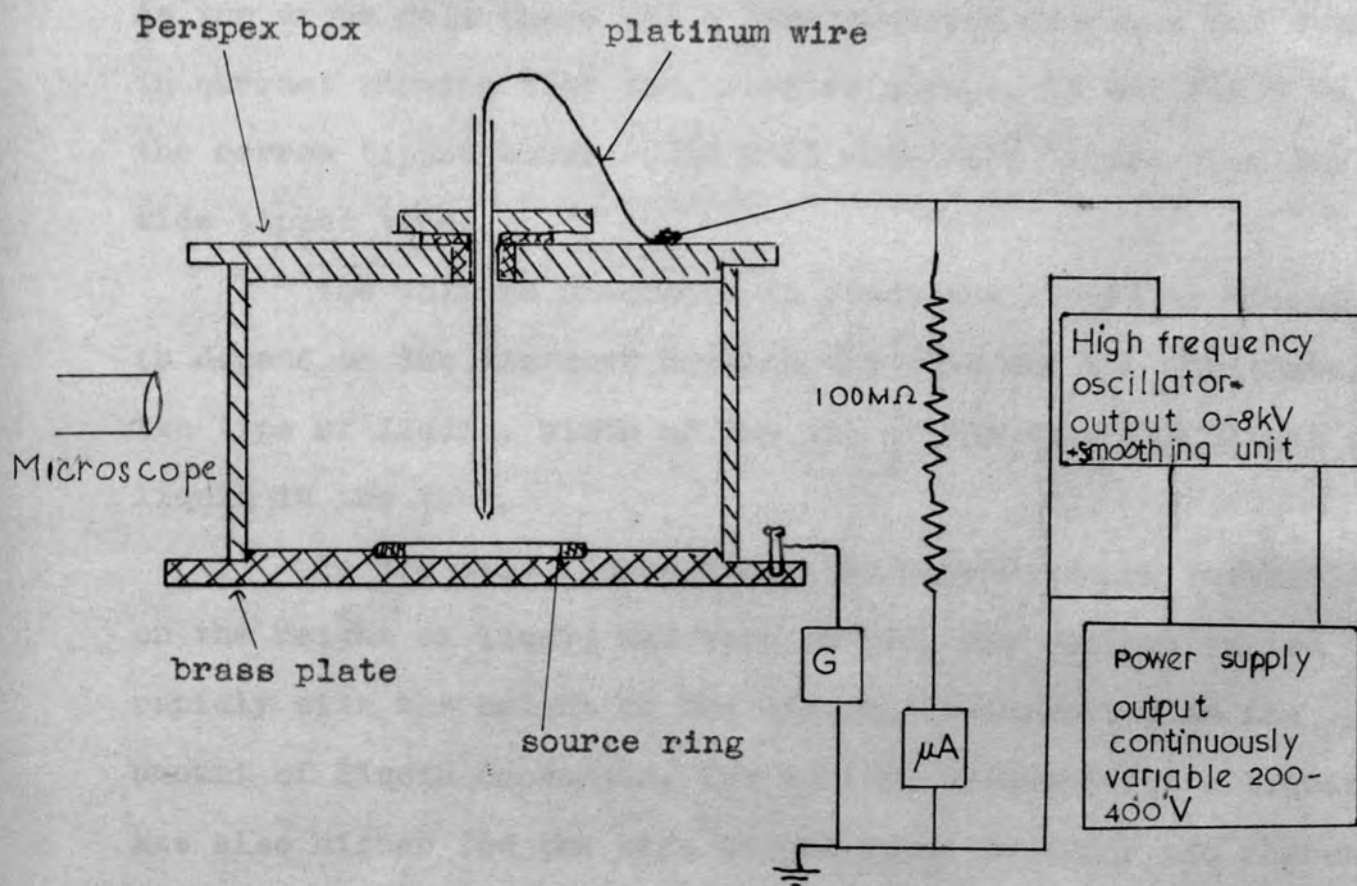
Fig. 26. View of the tip of the capillary tube seen in the microscope when the liquid is being ejected.

came out in drops until the surplus liquid had fallen out.
As the drops fell there was a corresponding increase and decrease
in current showing that they carried charge. It was found that
the narrow tipped tubes could hold much more liquid than the
wide tipped tubes.

The voltage necessary to eject the liquid was found
to depend on the distance between the tube and the substrate,
the type of liquid, width of the tip of the tube and height of
liquid in the tube.

In the wide tipped tubes the dependence of voltage
on the height of liquid was very marked. The voltage varied
rapidly with the height of the liquid. It increased as the
amount of liquid decreased. The voltage to discharge a liquid
was also higher for the wide tipped tubes than for the narrow
tipped ones. This was probably so because the drop was more
obtuse for the former. Sometimes double or triple deposits
were obtained, the appearance of which could be correlated
with the drop at the tip of the tube and the current. Two or
three points, instead of the usual one, were seen, and the current
increased abruptly as the points were formed. The wider tipped
tubes had a greater tendency to produce double or triple deposits
than the narrow ones. These additional peaks on the tip of the
liquid were sometimes formed if the voltage applied was too
high but disappeared when the voltage was lowered. From the
appearance of the tube (Fig. 26) it appears that the external

diameter is as important as the internal diameter.

The voltage at which the deposition began was not sensitive to the position of the wire in the tube, provided the wire did not block the end of the tube. However, the discharge was found to be much more stable in the narrow tipped tubes when the wire was near the tip of the tube, probably because the viscous forces in the capillary helped to damp any oscillations.

It was found that for hand drawn tubes the deposits obtained were not central, i.e. coaxial with the tube. Therefore the tubes were drawn vertically by placing them in a hand drill and applying the flame horizontally. The free end was allowed to fall under gravity. For these, the deposits were very accurately below the centre of the tip of the tube.

The deposits were observed for tips broken and those subsequently ground with carborundum. With the latter the deposits were well defined, whereas with the former they were more diffuse and had no sharp boundaries.

The size of the deposit was found to depend on the tube and was always the same for the same tube.

(iii b) Effect of wire.

Tungsten wire cut with wire cutters was used in the initial experiments. No marked change in the behaviour of the deposition was observed when the wire was sharpened to a point by etching it with sodium nitrite.

Platinum was used in later experiments; however, it was attacked rapidly if hydrochloric acid was present indicating the presence of free chlorine. A platinum + 20% iridium wire, which is more corrosion-resistant than pure platinum and also easier to handle, was therefore used for the final preparations.

(iii c) Effect of liquid.

The method was first tested with pure acetone and pure alcohol and added dye, then with a solution of 50% water and 50% alcohol by volume. With pure water the discharge was very slow and practically unobservable when a small amount of acid was present.

Addition of various inorganic salts to the solution of 50% water + 50% alcohol had no effect on the deposition. The voltage necessary for the ejection was the same as above and the shape of the deposit was unaffected, from which it may be concluded that once the liquid has been selected the satisfactory results will be obtained with any inorganic soluble salt and the yield probably the same for all materials.

After a large number of tests with a liquid containing a dye, no traces of the material could be detected on any portion of the apparatus, except at the central deposit, which suggests that the efficiency is high. The resolution of the spectrometer also shows that the source was very well defined and did not spread over the whole film area. The spray probably follows the lines of force originating at the tip of the drop.

When a solution of 50% of 1/2 N nitric acid and 50% alcohol was tried, no liquid emerged from the tube and no fall of meniscus was observed when the high voltage was applied even though a current was flowing. If the voltage was raised, streamers appeared as in a corona discharge and the current increased abruptly (Meek and Craggs, ref. 54).

With acid solution, acetone crystals were formed at the tip of the tube even with weak acid. This was probably due to acetone polymerizing in the presence of acid. No such effect was observed with alcohol.

On adding acid to the solution, the physical properties such as surface tension and density of the solution do not change very much [56, 57]. The effect must therefore be due to the increased hydrogen ion concentration of the solution, since inorganic salts did not affect the process.

When the best deposits were obtained, the current was 0.2-0.5 μA [52] depending on the quantity of liquid, and ~1.5 cc of liquid could be sprayed in 1 hr, although the volume of liquid used for preparing sources was about 1/3 of this. The voltage varied from 4-5 kV. The discharge was steadier when radioactive solutions were used, due to increase in the number of ions present near the tip of the liquid.

(iii d) Cerium source.

Cerium was supplied by The Radiochemical Centre, Amersham, as a solution of cerium chloride in 1N HCl. The

solution was evaporated with an infra-red lamp and the salt
redissolved in N/10 nitric acid. 66% by volume of alcohol was
added with a graduated pipette (the volume of the drops of
acid and alcohol were first measured). After the source was
prepared, the unused liquid was removed from the capillary
and stored.

(iii e) ThB source.

The ThB sources were prepared by dissolving the active
deposit from a platinum wire in N/10 nitric acid and N/10
hydrochloric acid, and again 66% alcohol was added. Similar
sources were obtained in both cases.

The above method has clearly a number of advantages
over the previously used methods [49] . The substrate, the
film on which the source is deposited, is not exposed to any
heat treatment and therefore much thinner backings can be used.
The apparatus is comparatively simple, and it is easy to control
any spread of contamination. The strength of the source can be
controlled easily and measured half way through the deposition.
The meniscus can be seen moving down the tube, and it is easy
to stop the process of deposition when the required volume of
liquid has been ejected. In the above, it was found that the
size of the deposit depends on the tube. This is somewhat of
a disadvantage, but a tube giving the correct size can usually
be selected. Any excess material is recoverable and very small
quantities of material are necessary.

Further investigations on the processes taking
place at the tip of the tube would considerably help in
providing guidance in the selection of appropriate parameters.
From the above it appears that the surface tension plays an
important role, the viscosity probably has some influence and
the hydrogen ion concentration is very important. The point
of the liquid was very sharp and it was difficult to see how
the liquid surface disintegrates, but no disturbances or glow
could be seen on the tip. The current was very steady. It may
be that the temperature at the point is high or that the liquid
disintegrates at the expense of the electrical energy.

IV

(i)   <u>Alignment of large spectrometer.</u>

The baffle system of the large spectrometer was first centralized on the bench (Fig. 6) with respect to the axial tube, all the motions were tested, and the rings of the slit aligned (Fig. 7). The baffles were then placed into the tank and centralized mechanically with respect to the tank using micrometer calipers. The rings of the slit can be moved horizontally and vertically (horizontal and vertical motion) with respect to the central tube and therefore the fine adjustments could be made during operation. The mask (13, Fig. 2) was used to test the alignment.

To centralize the ring slit the counting rate was measured for the horizontal displacement and vertical displacement of the slit. The results are shown in Fig. 28 and 27. From these it can be seen that 60° rotation of the control rod for the horizontal motion produced the same displacement of the slit system as ~ 65 turns of the control for the vertical motion. The position at which the counting rate is a maximum was taken as the correct position. This was tested in two ways.

The counting rate with the rotation of the mask was measured for two positions of the horizontal motion. In Fig. 29 the horizontal motion was at 150°. The existence of only one sharp peak shows that more beta rays were getting through one side of the slit than through the other, i.e. that the
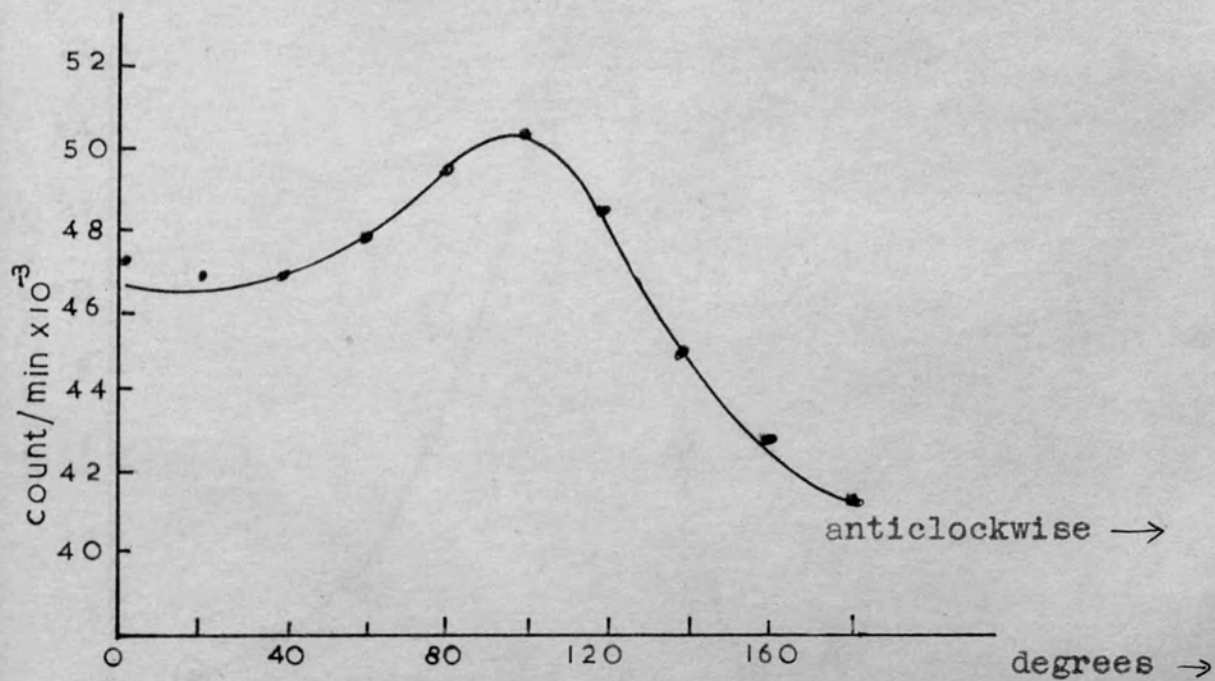
Rotation of control rod for horizontal motion.

Fig. 27. Variation of the counting rate as the ring slit is moved horizontally.
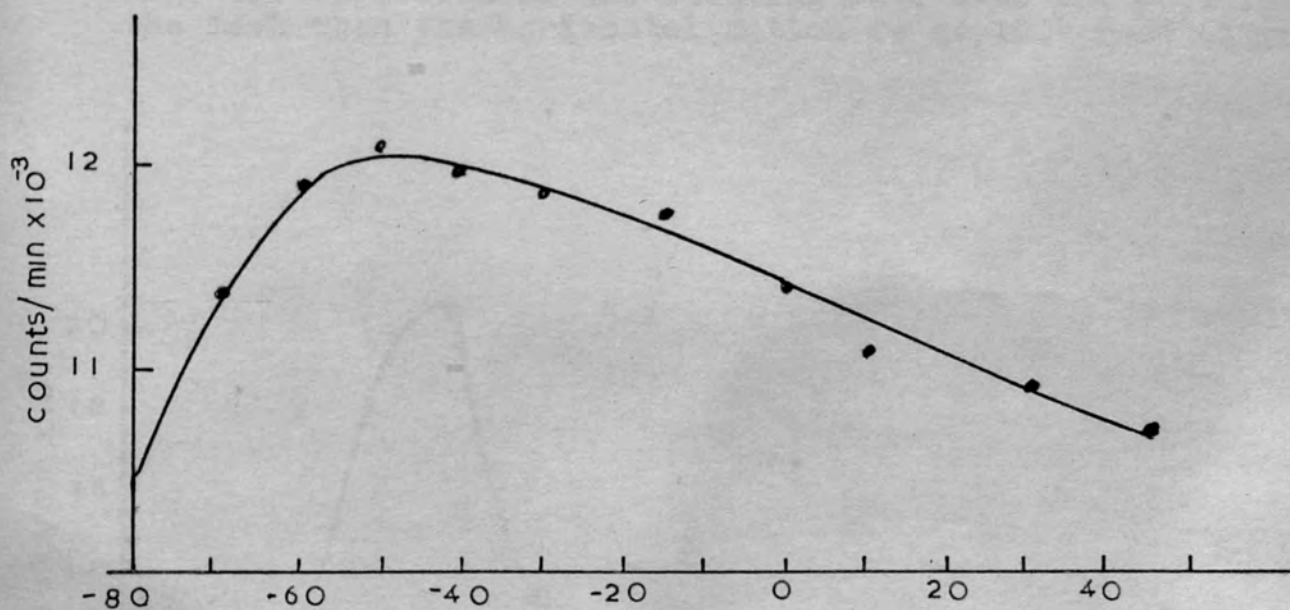
Rotation of control rod for vertical motion (turns).

Fig. 28. Variation of the counting rate with the vertical motion of the slit assembly.
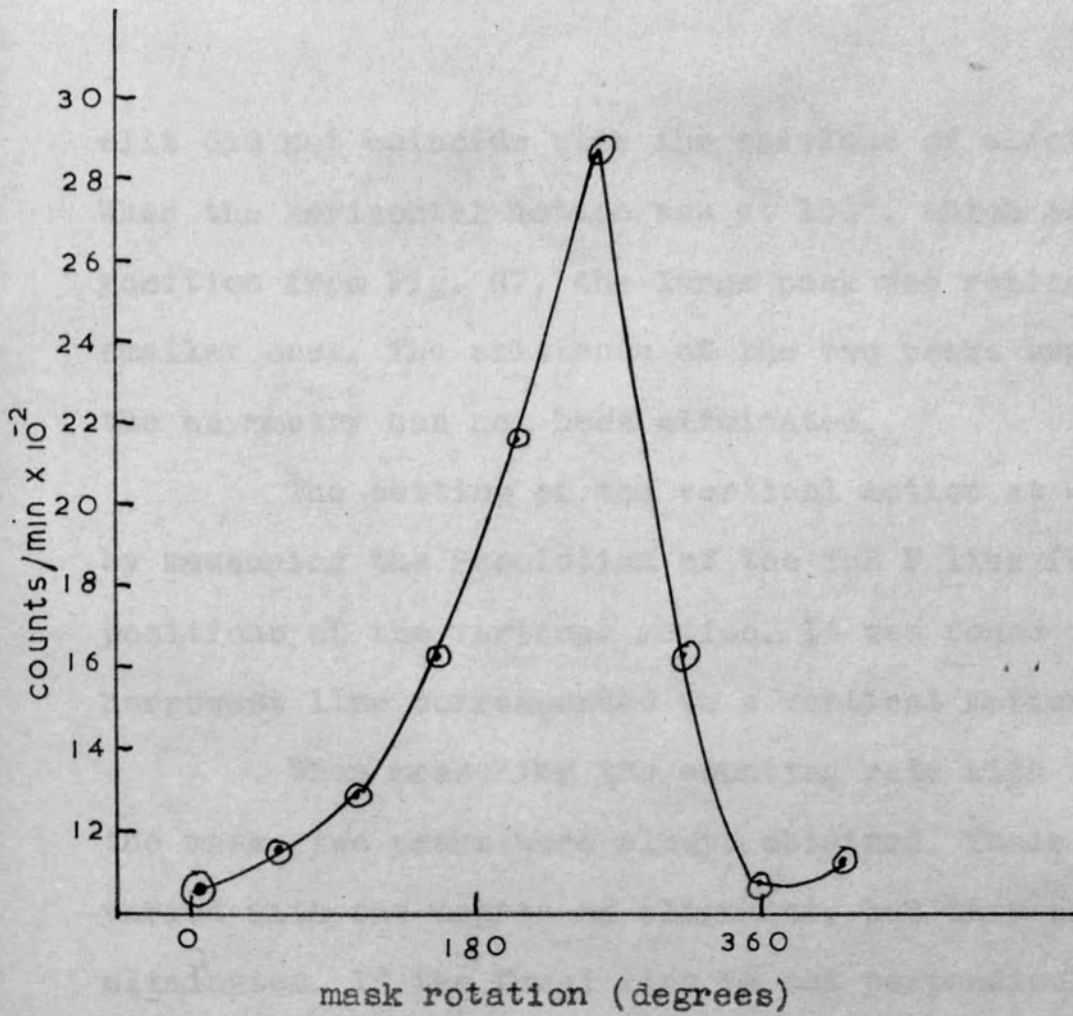
Fig. 29. Variation of the counting rate with the rotation of
the mask when the horizontal motion is at 150° (not aligned).
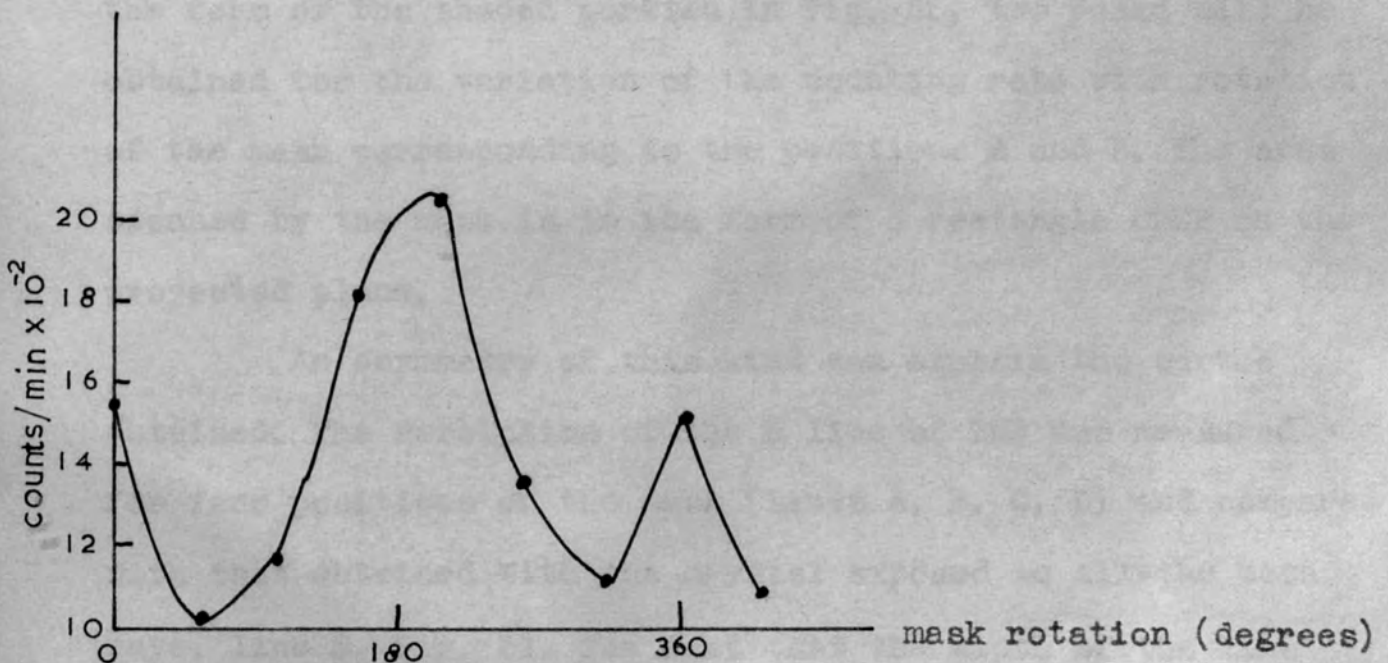
Fig. 30. Variation of the counting rate with the rotation of the
mask when the slit system is near the correct position.

slit did not coincide with the envelope of electron trajectories. When the horizontal motion was at 100°, which is the correct position from Fig. 27, the large peak was replaced by two smaller ones. The existence of the two peaks suggests that the asymmetry has not been eliminated.

The setting of the vertical motion at -45 was tested by measuring the resolution of the ThB F line for several positions of the vertical motion. It was found that the narrowest line corresponded to a vertical motion setting of -45.

When measuring the counting rate with the rotation of the mask, two peaks were always obtained. Their amplitude varied with the degree of alignment, but they could not be eliminated. If the focal ring is not perpendicular to the axial tube but at a small angle to it and the image of β-rays on a piece of photographic paper [17] covering the crystal is in the form of the shaded portion in Fig. 32, two peaks will be obtained for the variation of the counting rate with rotation of the mask corresponding to the positions A and B. The area scanned by the mask is in the form of a rectangle CDEF on the projected plane.

An asymmetry of this kind can explain the curves obtained. The resolution of the F line of ThB was measured for four positions of the mask (lines A, B, C, D) and compared with that obtained with the crystal exposed to all the beta rays, line E, Fig. 31. The fact that the width of the line varies with the position of the mask supports the assumption
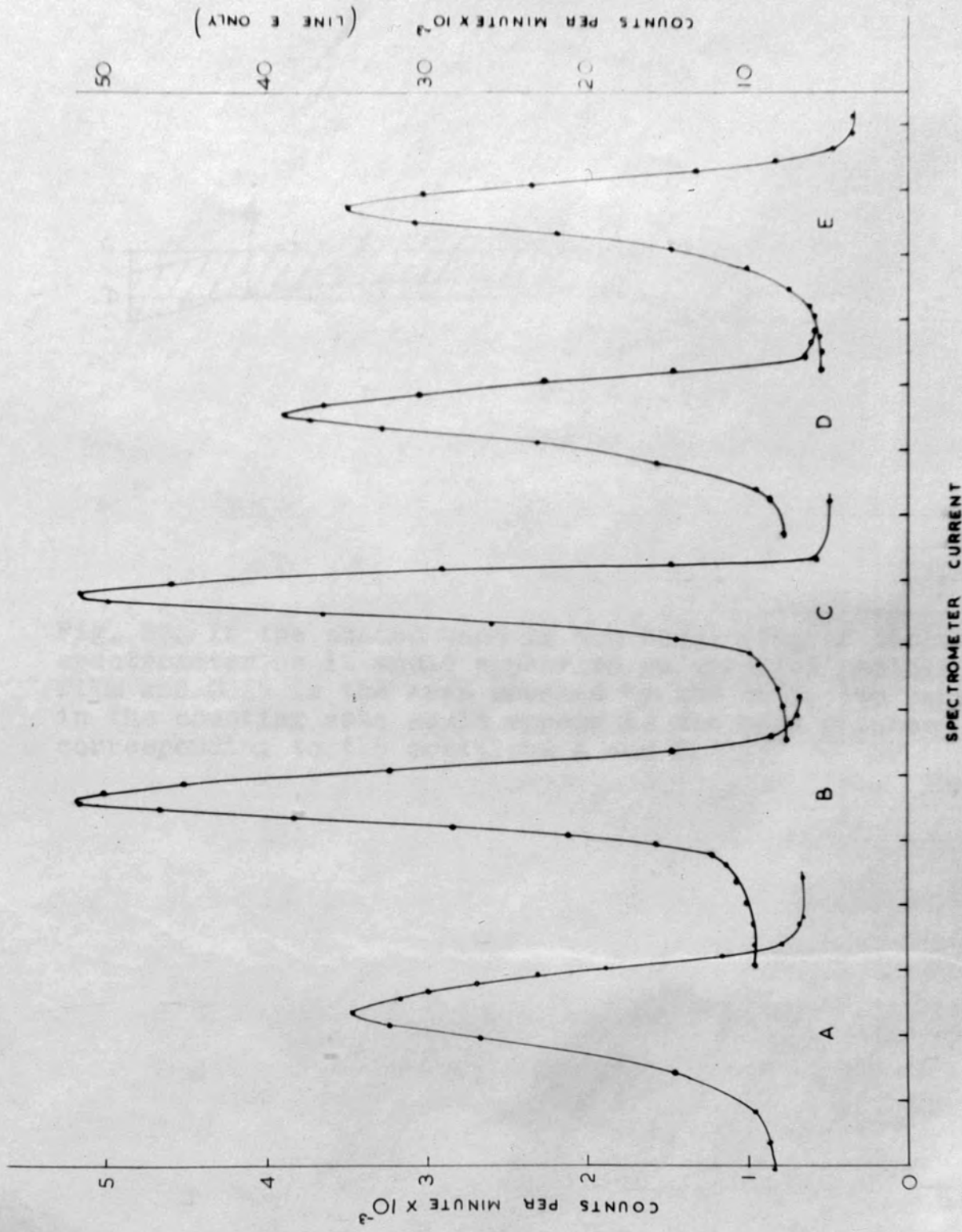
Fig. 31. The ThB F line taken at four positions of the mask. The widths at half height are for a 0.59% , B 0.42%, C 0.38%, D 0.42% and E 0.45%. For line E the mask was withdrawn
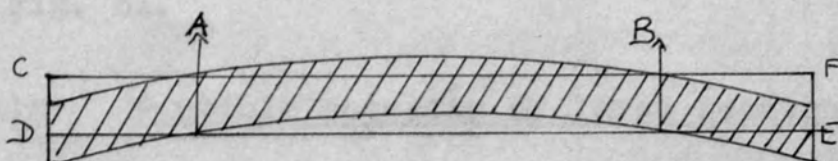
Fig. 32. If the shaded band is the focal ring of the
spectrometer as it would appear on an unrolled photographic
film and CDEF is the area scanned by the mask, two peaks
in the counting rate would appear as the mask rotates
corresponding to the positions A and B.

that a small asymmetry still exists. An obstruction in the path of the β-rays, such as the pillar supporting the axial tube, could explain the dips in Fig. 30 but not the results of Fig. 31.

(ii)   Particle detector of large spectrometer.

        The resolution and performance of the particle detector (plastic scintillator NE102) of the large spectrometer was investigated by measuring the pulse height spectra from the output of the limiter valve (input is from the anode of the photomultiplier) and the output of the cathode follower (input is from the 11th dynode of the 13-stage photomultiplier). The circuits described by Freeman [37] were used. Some of the results are shown in Fig. 33. The pulse height spectra are dependent on the rise and fall time of the wide band amplifier and were chosen to give the maximum separation between the noise and peak produced by the β-rays. The curves were obtained with a voltage on the photomultiplier 1.76 kV. Curves a and b were obtained with the same gain of the amplifier, but the gain had to be increased for the curve c. The position of the peak (corrected for gain of the amplifier) against energy has been plotted in Fig. 33d. The cathode follower output increases linearly with energy. The limiter output, however, changes little as the energy is decreased, but falls rapidly when the pulse from the photomultiplier is not sufficiently large to cut off the conducting limiter valve. However, from 33c it

can be seen that the limiter peak has a low energy tail but is very much sharper than that for the cathode follower.

(iii)   Electron detector of small spectrometer.

Initially, pulse height spectra were taken of the output from the limiter and cathode follower of the small spectrometer as above with the small crystal (shown in Fig. 2) 1 1/2" diameter. It is desirable to have as large a solid angle as possible in coincidence measurements. An attempt was therefore made to increase the solid angle of collection by replacing the small crystal by a 3" crystal. The method of mounting is shown in Fig. 34. The light pipe was made up of several sections and an attempt was made to join the components with silicone fluid which had been allowed to stand in a high vacuum for some time to remove air bubbles from the fluid. When the parts were joined and placed into a vacuum, the components of the light pipe separated at the edges. This method could not be used and it was therefore stuck with Perspex cement [60, 61] . The crystal was attached to the light pipe with the silicone fluid. Aluminium was evaporated in vacuo onto the surface of the crystal facing the β-rays and the inner surface of cylinder A, Fig. 34.

The pulse heights found for this system were half of those found for the small crystal under the same conditions showing that the light collection efficiency was lower. The
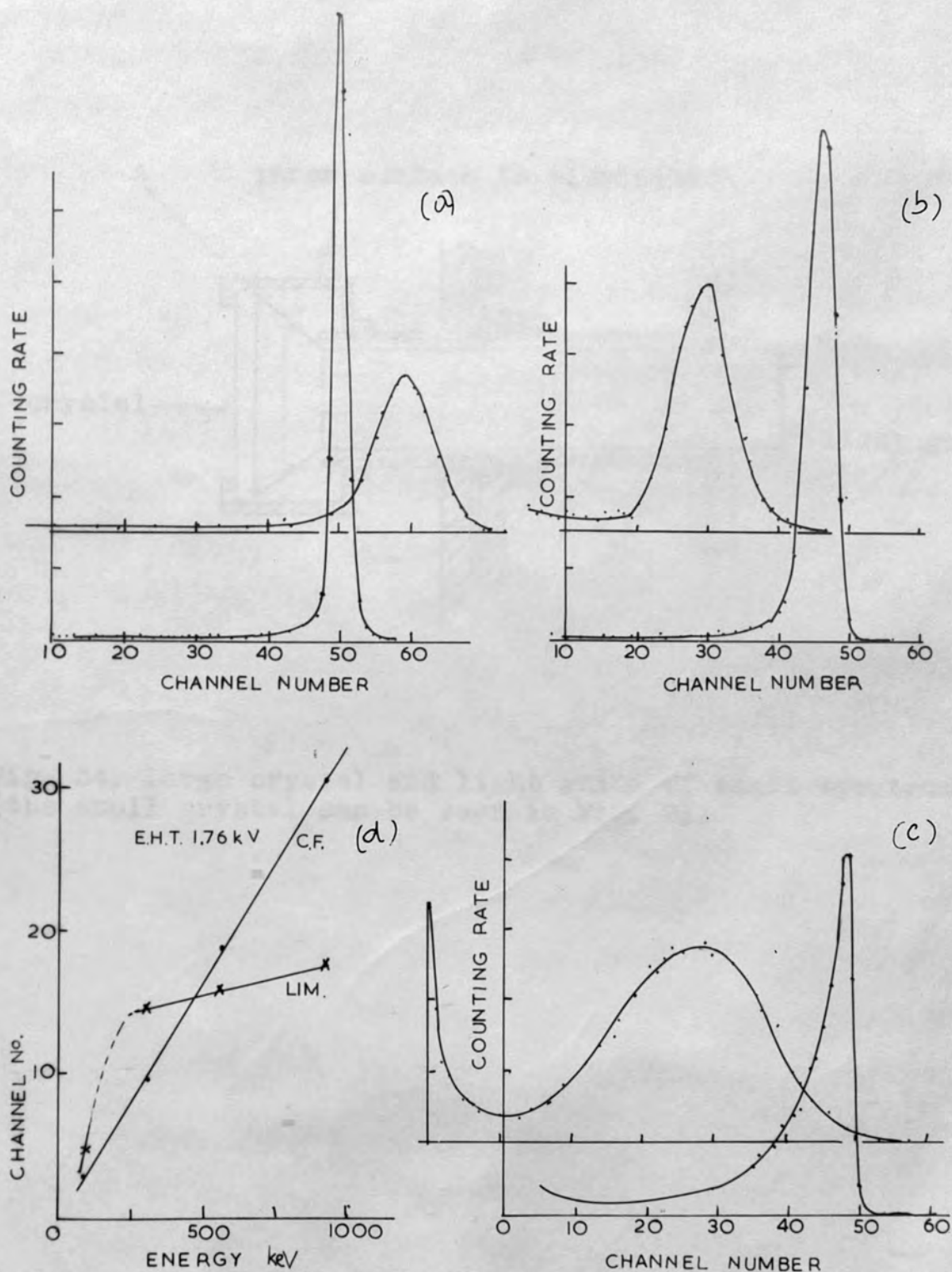
Fig. 33(a),(b),(c). Pulse height spectra taken with the large spectrometer focused for different energies. The gain of the amplifier is the same for (a) and (b), but had to be raised to obtain (c).

Fig. 33(d). Variation of pulse height (channel number corrected for gain of amplifier) with energy focused.
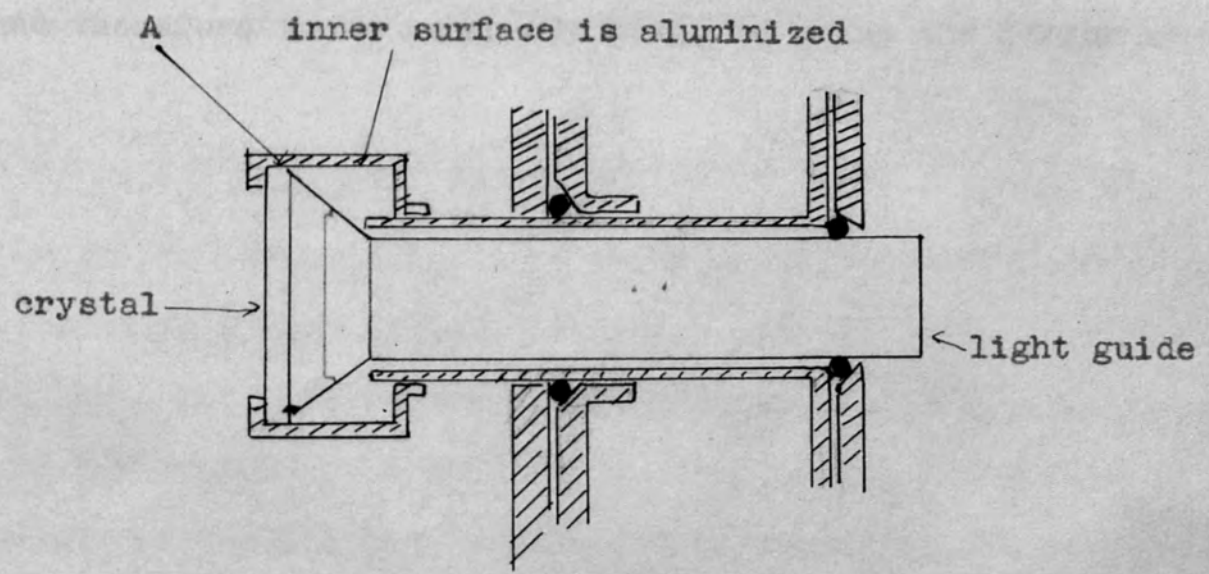
Fig. 34. Large crystal and light guide of small spectrometer (the small crystal can be seen in Fig. 2).

counting rate at the peak of the F line measured with respect to that in the large spectrometer did not increase appreciably and therefore there is no advantage in using the larger crystal.

(1)   Measurement of e^- - e^- coincidences.

The block diagram is shown in Fig. 35. The coincidence circuit is a form of Bell and Petch circuit [25] described in [57]. The electronics was first tested with a pulse generator and ThB sources were used for further tests. The effect of the length of the clipping cables at the output of the limiter on the pulse height of the coincidences was investigated using the 100 channel pulse height analyser. Pulse height spectra were plotted for various lengths of clipping cables with the spectrometers focused on the ThB F line. A pulse spectrum taken with 10 mμ sec clipping cables is shown in Fig. 36. It was found that with shorter clipping cables the energy loss between the singles and coincidences was smaller than for the longer cables, however, 10 mμ sec cables were chosen to reduce the resolving time of coincidence circuit and thus the number of chance coincidences ($N_{ch} = 2\tau N_1 N_2$, where 2τ is the resolving time of the coincidence circuit).

The E.H.T. on the photomultiplier of the small spectrometer had to be raised to 1.96 kV in order to equalise the output pulses from the limiters from each spectrometer. The pulse height spectra were measured with the single channel

V

Measurement of e^- - e^- coincidences and experiments with Ce^{144}.

(i)   Measurement of e^- - e^- coincidences.

The block diagram is shown in Fig. 35. The coincidence circuit is a form of Bell and Petch circuit [25] described in [37]. The electronics was first tested with a pulse generator and ThB sources were used for further tests. The effect of the length of the clipping cables at the output of the limiter on the pulse height of the coincidences was investigated using the 100 channel pulse height analyser. Pulse height spectra were plotted for various lengths of clipping cables with the spectrometers focused on the ThB F line. A pulse spectrum taken with 10 mμ sec clipping cables is shown in Fig. 36. It was found that with shorter clipping cables the separation between the singles and coincidences was smaller than for the longer cables, however, 10 mμ sec cables were chosen to reduce the resolving time of coincidence circuit and thus the number of chance coincidences ($N_{ch} = 2\tau N_1 N_2$, where 2τ is the resolving time of the coincidence circuit.

The E.H.T. on the photomultiplier of the small spectrometer had to be raised to 1.94 kV in order to equalize the output pulses from the limiters from both spectrometers. The pulse height spectra were measured with the single channel
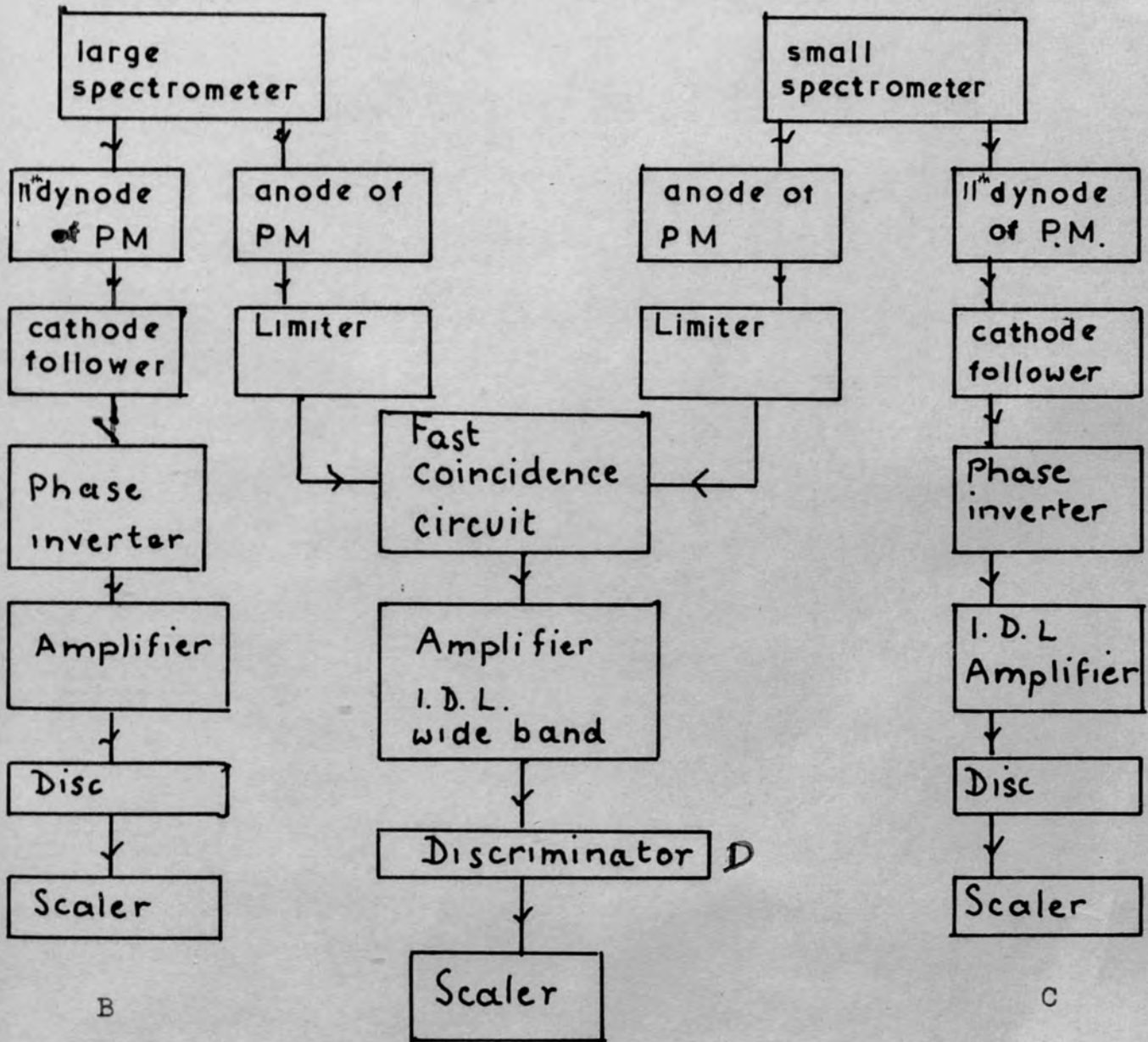
Fig. 35. Block diagram of the electronics for counting $e^- - e^-$ coincidences.
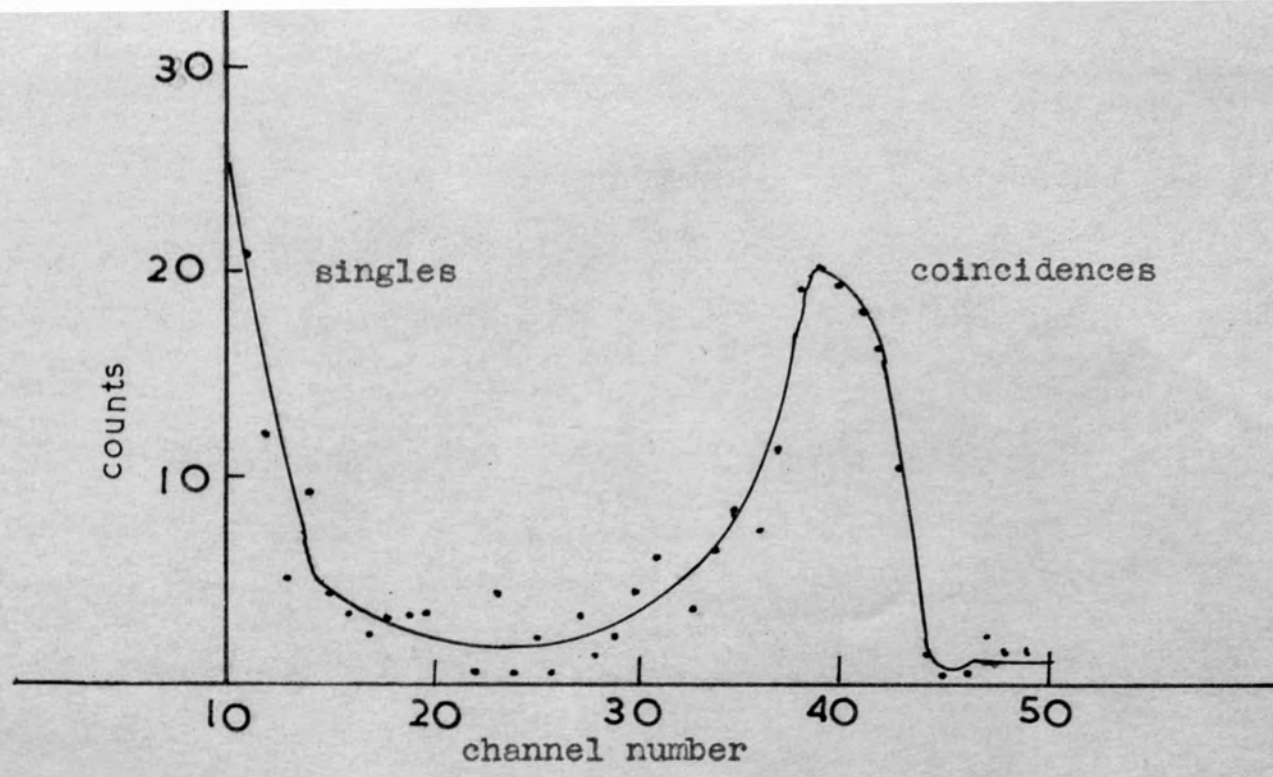
Fig. 36. Pulse height spectrum for ThB coincidences.
Both spectrometers were focused on the F line.
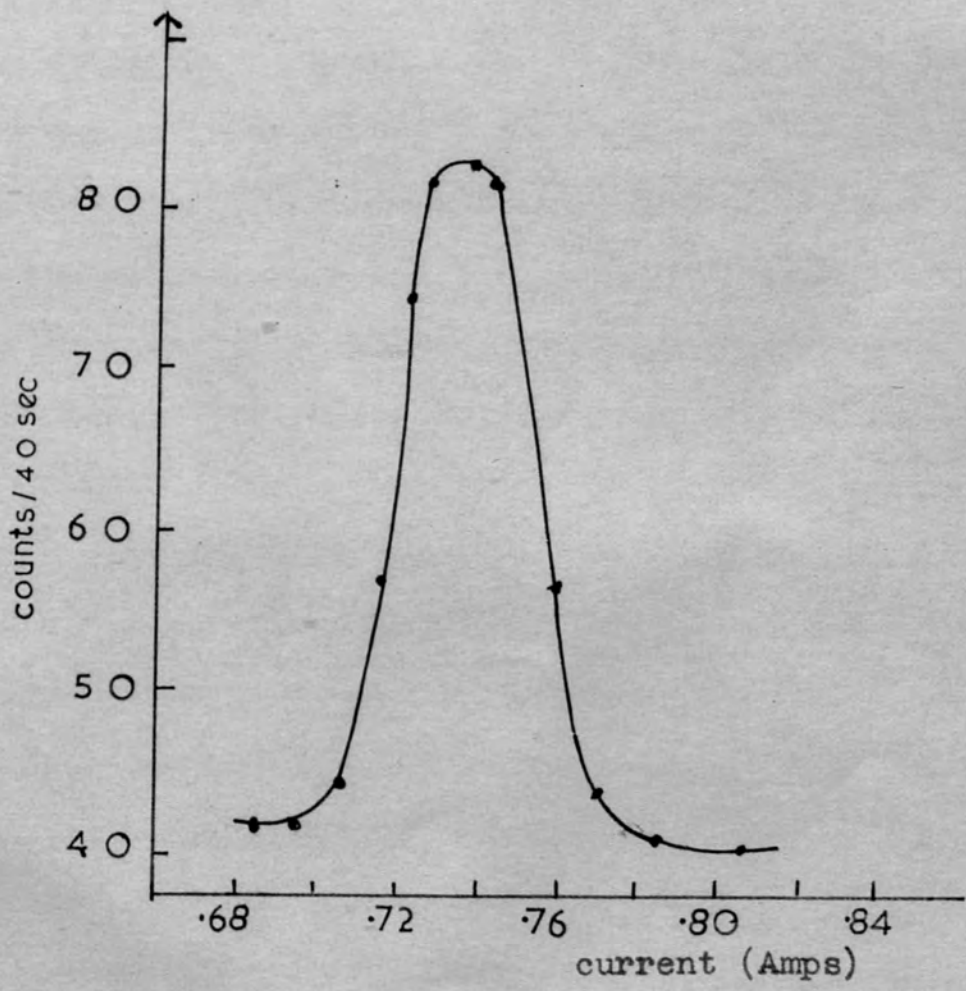
Fig. 37. 91 keV (K 133) line in small spectrometer.

pulse height analyser D in Fig. 35 after switching off the E.H.T. on one photomultiplier so that the impedances were unchanged and no reflections were introduced. This was done with each spectrometer in turn. It was not sufficient to measure the pulse height spectra of each line after the pulses had passed through the limiter and amplifier because any difference in pulse height in the fast line A is multiplied by 10^4.

To find the difference in transit time between the two spectrometers for the energies to be used in investigating the coincidences between the 91 keV (K133) and the 26 keV (L_I33) conversion lines of Pr^{144}, the delay curve shown in Fig. 38 was plotted. The 10 mμ sec clipping cables were used. The small spectrometer was at the peak of the 91 keV conversion line and the large one on the portion of the continuous spectrum at 41 keV. These conditions were chosen because they were close to the required conditions.

It was found that the E.H.T. on the photomultiplier of the large spectrometer had to be raised from 1.76 kV to 1.90 kV to equalize the pulses owing to the smaller pulse heights at 26 keV. The method described above was used. The change in transit time between 41 keV and 26 keV β-rays in the large spectrometer was calculated using the delay curve and the path length of 180 cm found by Freeman [37]. The calculated values were in agreement with those found experimentally in reference 37.
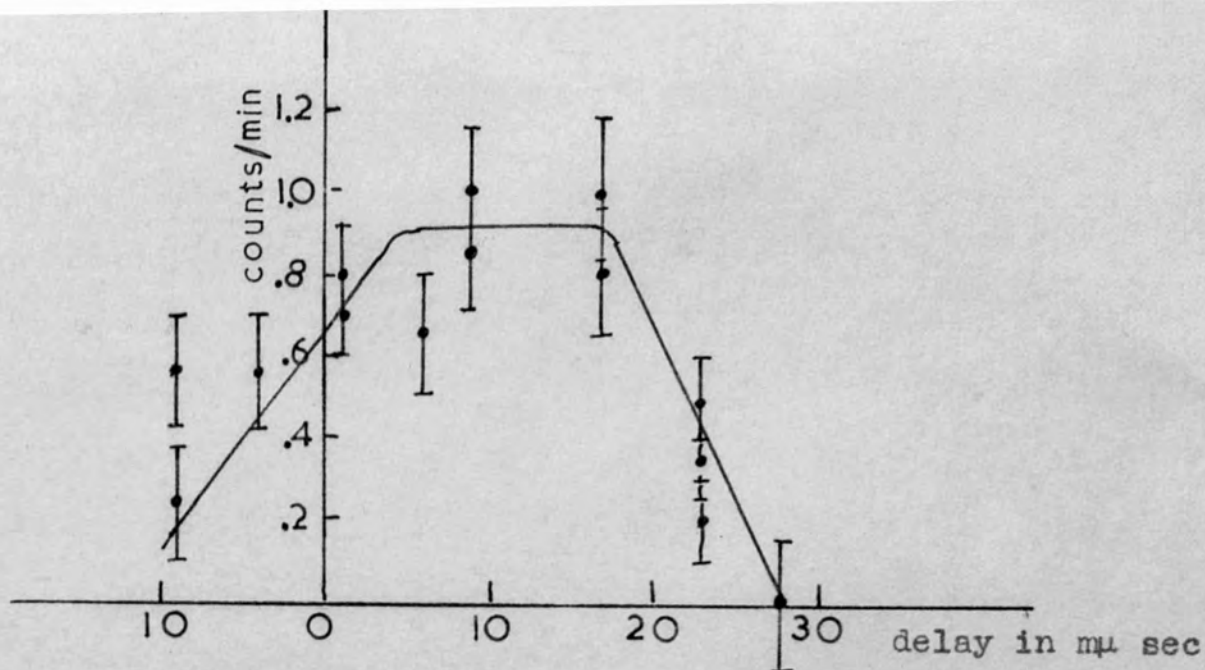
Fig. 38. Delay curve with small spectrometer focused on the 91 keV (K 133) conversion line and the large spectrometer on the continuous spectrum at 41 keV.
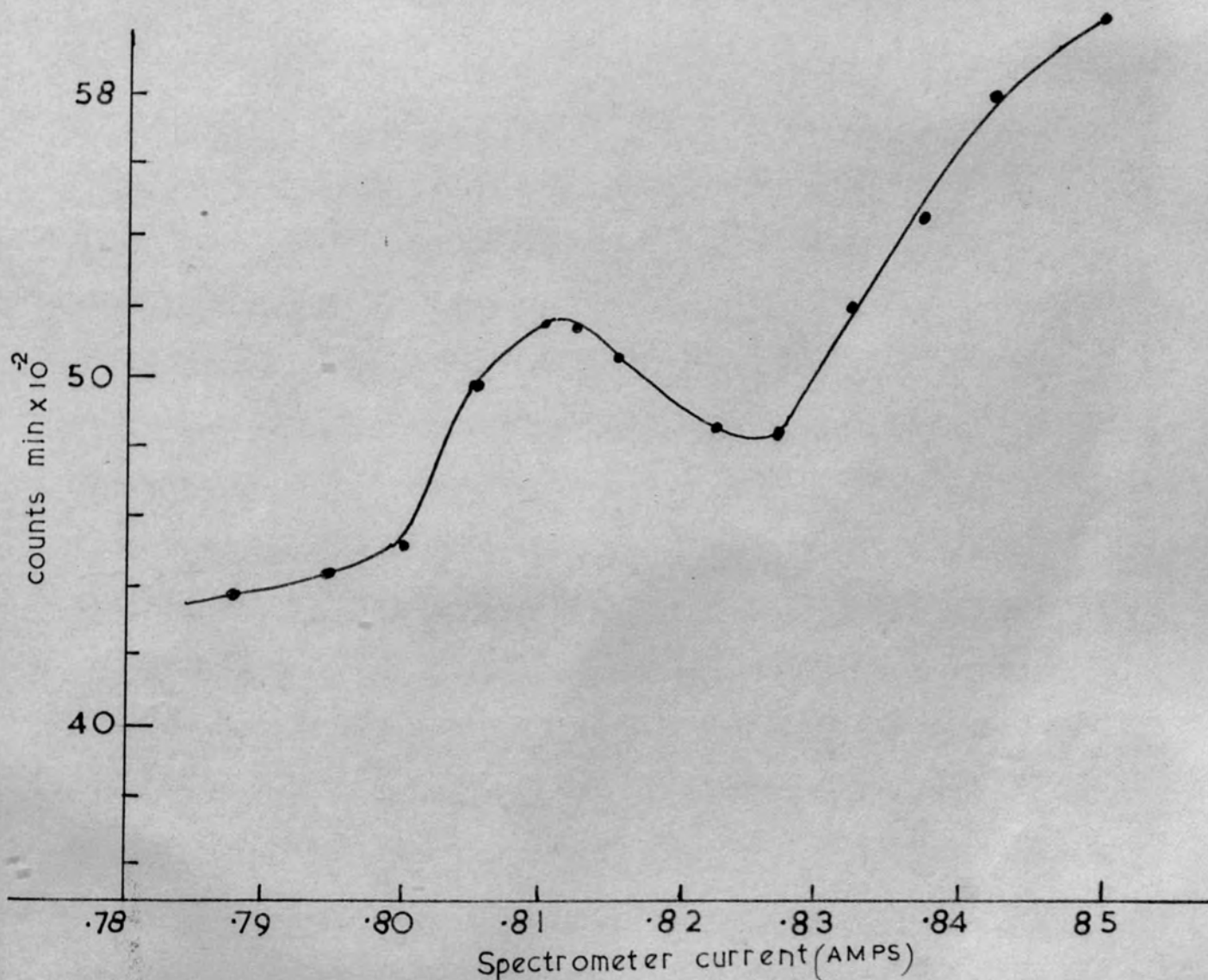
Fig. 39. 26 keV (L$_1$ 33) line measured with the large spectrometer.

The change in time over the investigated range was found to be 3 mμ sec which was conveniently low, and therefore the same delay lines could be used for the whole investigation without moving off the plateau of the delay curve. The resolving time of the coincidence circuit was ~2 x 10^{-8}sec. The maximum number of chance coincidences was calculated to be 0.1 count/hr. The resolution of the 91 keV conversion line was 0.9% for the large spectrometer and 5% for the small spectrometer.

(ii)   Experiments with Ce^{144}.

To verify the existence of a 166 keV level in the excited state of Pr^{144}, the decay product of Ce^{144}, an attempt was made to find e$^-$- e$^-$ coincidences between the internal conversion lines of the 33 keV and 133 keV γ-rays, because one mode of de-excitation of the 166 keV level was thought to take place by the successive emission of these two γ-rays [10]. The available information about this decay scheme has been summarized in Figs. 1(i) and 1(ii), and Tables I and II. If the 166 keV level exists as suggested by Freeman [10], the 133 keV level is fed partly by the 33 keV γ-ray and partly by the disintegration electrons from Ce^{144}. Since the other γ-rays from the 166 keV level are weak compared with the 33 keV γ-ray and the intensity of the 53 keV γ-ray coming from the

133 keV level is $\leq 10\%$ of the intensity of the 133 keV γ-ray, $\sim 33\%$ of the 133 keV transitions are preceded by the 33 keV γ-rays, i.e. the probability that the 33 γ-ray precedes the 133 keV γ-ray is $\sim 33\%$ (see Appendix, [32]). Provided that the resolving time of the coincidence circuit is long in comparison with the lifetime of the 133 keV state, the cascade will be observable as a prompt coincidence. The half life of the 133 keV transition was found in [10] to be less than 5×10^{-10} sec which is two orders of magnitude less than the resolving time of the coincidence circuit used in the present investigation ($\sim 2 \times$ $\times 10^{-8}$ sec).

If the lifetime of the 166 keV level is sufficiently short, the 33 keV gamma ray (or 26 keV internal conversion line) will be in coincidence with the 135 keV continuous β-ray component feeding the 166 keV level. The contribution to the total counting rate of this β-ray component at an energy of the K133 conversion line (91 keV) was calculated from Freeman's Fermi analysis and was found to be 5% of the total counting rate. It was found that the ratio of the height of the 91 keV conversion line to the total continuous spectrum underneath it (Fig. 37) in the small spectrometer was 1.1/1, therefore the ratio of the height of the line to the 135 keV β-ray component at 91 keV is 1.1/5%. If the coincidences between the portion of the spectrum including the 26 keV ($L_I 33$) conversion
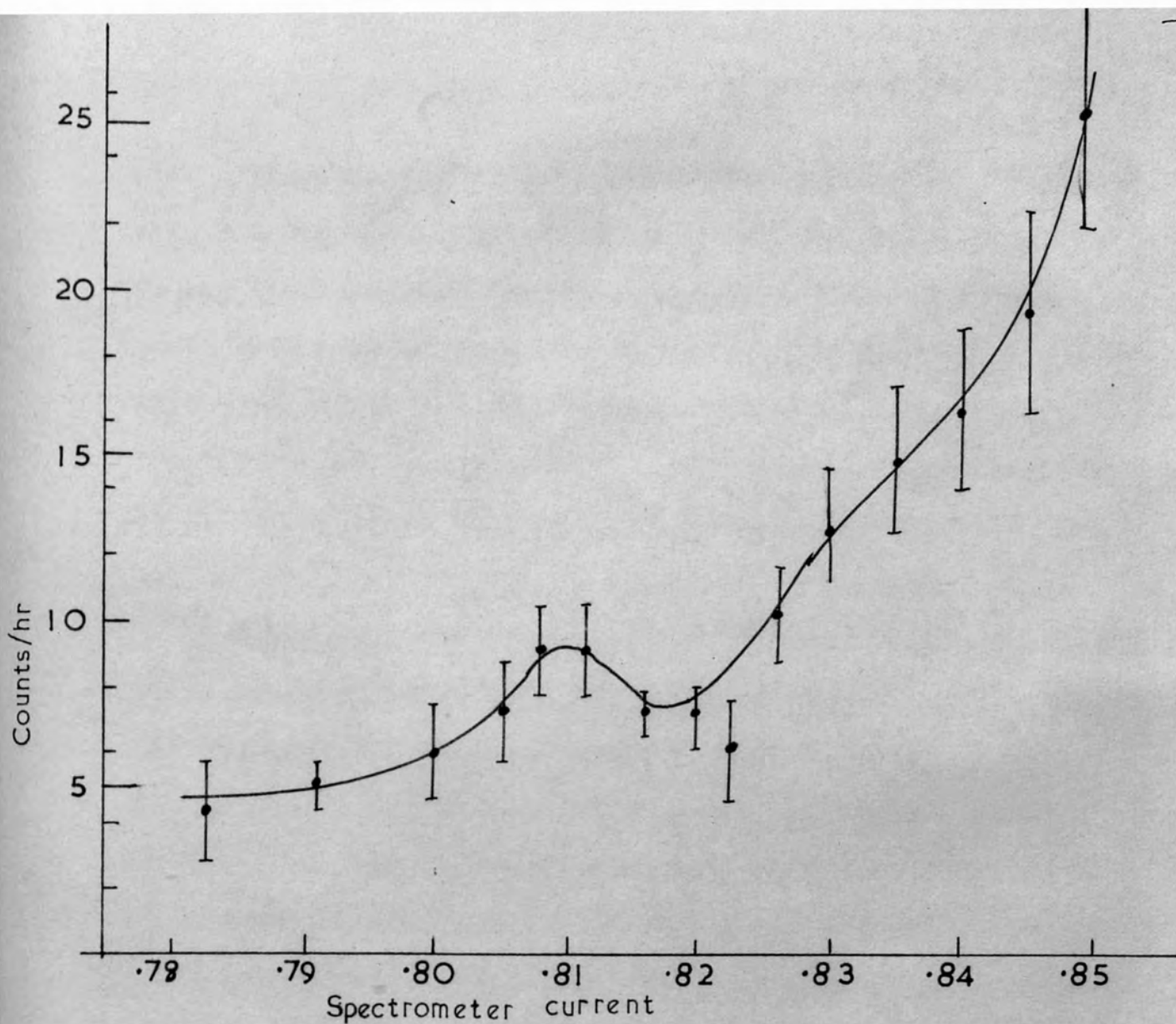
Fig. 40. Spectrum in coincidence with the 91 keV (K 133) conversion line.
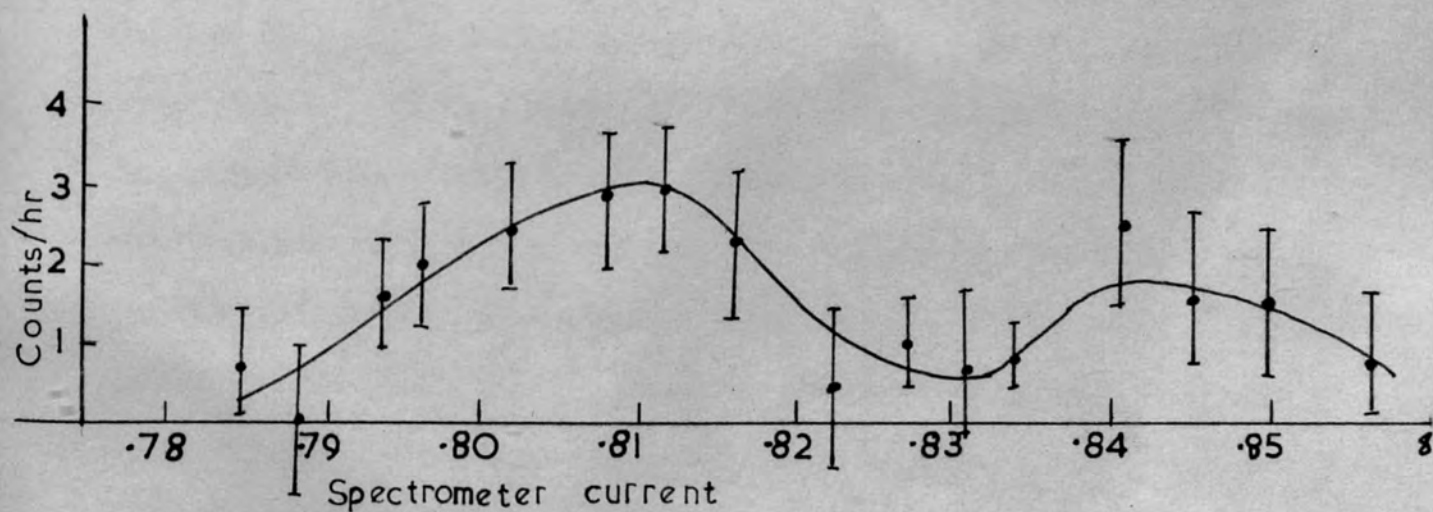
Fig. 41. Spectrum in coincidence with the continuous spectrum just above the 91 keV conversion line.

line are measured with the large spectrometer when the small
spectrometer is first focused at an energy just above the
91 keV line and then the measurements are repeated with the
small spectrometer on the 91 keV line, the expected increase
in the height of the 26 keV conversion line is 7.3 (1.1 x 33/5),
i.e. it should be 8.3 times as high in the second experiment
as in the first if the percentage assignements in [10] are
correct.

The spectrum in coincidence with the portion of the
β-ray spectrum just above the 91 keV line is shown in Fig. 41.
The spectrum above the line was used because there is less
likelihood of having a contribution from the tail of the line
on the high energy side of the line. The fact that coincidences
were detected confirms the assumption that the lifetime of
the upper state of the 33 keV γ-ray is short. The small peak
at a current 0.84 A was interpreted as the Auger line at an
energy 28 keV. The 26 keV (L_I33) conversion line is at 0.81 A.
During the coincidence measurements the singles counts were
taken with both spectrometers from the cathode follower outputs
to ensure that there was no drift in current and that the
spectrometers were focused for the correct energies with respect
to the lines. The coincidence spectrum with the small spectro-
meter on the peak of the line is shown in Fig. 40. The con-
tinuous spectrum underneath the 26 keV line is due to the
β-ray component in coincidence with the K133 conversion line.

The results do not show the expected increase in the height
of the $L_I 33$ conversion line. Due to the experimental error,
the upper limit of the probability that the 133 keV β-ray
is preceded by the 33 keV γ-ray is reduced to 3% from the
33% suggested by Freeman [10]. The results show no evidence
for the existence of the 166 keV state.

The sensitivity of the experiment could be increased
if the height of the 91 keV conversion line above the continuous
spectrum could be increased by raising the resolving power
and improving the statistics of the counts.

If the 33 keV γ-ray is in coincidence with the 135 keV
β-ray component (as suggested in ref. 10), no coincidences
should be found if one spectrometer is focused to an energy
above the latter and below 185 keV and the other spectrometer
is focused on the $L_I 33$ conversion line. If, however, the 33 keV
γ-ray is in coincidence with the 185 keV β-ray component
(Geiger et al., 1960), coincidences should be detected.

The results obtained are not in conflict with the decay
schemes b, c, f, e, g, k of Fig. 1.

It would be interesting to verify the 41-133 keV gamma
cascade and prove the existence of the 175 keV level which so
many authors have found.

Appendix.

The $e^- - e^-$ coincidence counting rate is

$$C = N_0 \delta_A \omega_1 \epsilon_1 \chi_{KA} {}_A q_B \delta_B \omega_2 \epsilon_2 \chi_{KB} \epsilon_c f(\theta) \chi_{KB}$$

provided spectrometer II is focusing the K-conversion line corresponding to the transition B and spectrometer I is focusing the K-conversion line corresponding to the transition A, where

N_0 is the number of nuclear disintegration per unit time,

δ_A is the probability per disintegration that a transition A will occur,

χ_{KA} is the K-conversion probability,

ω_1 is the effective transmission of the corresponding spectrometer channel I,

ϵ_1 is the efficiency of the detector of spectrometer I,

$f(\theta)$ represents the angular correlation effect,

ϵ_c is the coincidence counting efficiency.

The product ${}_A q_B \delta_B$ gives the probability per nuclear decay that, if the transition A has occured, the transition B will precede or follow it.

References.

1.   W.S. Emmerich, G. John and J.D. Kurbatov, Phys. Rev.
                              82 (1951) 968

2.   H.B. Keller and J.M. Cork, Phys. Rev. 84 (1951) 1079

3.   W.S. Emmerich, W.J. Auth and J.D. Kurbatov, Phys. Rev.
                              94 (1954) 110

4.   J.M. Cork, M.K. Brice and L.C. Schmid, Phys. Rev.
                              96 (1954) 1295

5.   W.E. Kreger and C. Sharp Cook, Phys. Rev. 96 (1954) 1276

6.   I. Pullman and P. Axel, Phys. Rev. 102 (1956) 1366

7.   V.P. Parfenova, N.V. Forafontov and V.S. Shipinel,
                Izv. Akad. Nauk (SSSR), Ser. Fiz. 21(1957)1601

8.   R.L. Hickok, W.A. McKinley and S.C. Fultz, Phys. Rev.
                              109 (1958) 113

9.   A.K. Sengupta, R. Bhattacharyya, J. Lahiri and R.M.
      Mukherjee, Indian Jour. of Phys. 33 (1959) 388

10.   N.J. Freeman, Proc. Phys. Soc., 74 (1959) 449

11.   R.V. Gnedich, L.N. Kryukov and V.V. Murav'eva, Jour. Exp.
                and Theor. Phys. (SSSR), 36 (1959) 329

12.   N.V. Forafontov and A.A. Sorokin, J.E.T.P. (SSSR) 36 (1959)
                                                              330

13.   J.S. Geiger, R.L. Graham and G.T. Ewan, Nuclear Physics
                              16 (1960) 1

14.   K. Siegbahn, Physica 18 (1952) 1043

15.   K. Siegbahn, β- and γ-ray Spectroscopy, Amsterdam, (1955),
                                                              p. 52

16.   T.R. Gerholm, Encyclopaedia of Physics, Ed. Flugge (1956),
                                              Vol. 33, p. 668

17.   P.R. Evans, N.J. Freeman, G.K. McGinty, B.H. Armitage and
      H.O.W. Richardson, Proc. Phys. Soc. 72(1958) 949

18.   R.L. Graham, G.T. Ewan and J.S. Geiger, Nucl. Inst. and Meth.
                              9 (1960) 245

19. M. Mladjenovic, Nucl. Inst. and Meth. 7 (1960) 11

20. N. Feather, Proc. Camb. Phil. Soc. 36 (1940) 224

21. N. Feather, J. Kyles and R.W. Pringle, Proc. Phys. Soc.
                                    (Lond.) 61 (1948) 466

22. L.V. Groshev and L.Ya. Shaftvalov, Dokl. Akad. Nauk (SSSR)
                                    68 (1949) 257

23. R. Katz, R.D. Hill and M. Goldhaber, Phys. Rev. 78 (1950) 9

24. C. Fowler and R. Scheffer, Rev. Sci. Inst. 21 (1950) 740

25. R.E. Bell, R.L. Graham and H.E. Petch, Can. Jour. of Phys.
                                    30 (1952) 30

26. K. Siegbahn, Ark. f. Fysik, 4 (1952) 223

27. S. Kageyama, J. Phys. Soc. Japan, 8 (1953) 689

28. C.G. Campbell and J. Kyles, Proc. Phys. Soc. (LOnd.)
                                    B 66 (1953) 911

29. J. Kyles, C.G. Campbell and W.J. Henderson, Proc. Phys. Soc.
                                    (Lond.) A 66 (1953) 519

30. T. Gerholm, Rev. Sci. Inst. 26 (1955) 1069

31. T.R. Gerholm, Ark. f. Fys. 11 (1956) 55

32. T.R. Gerholm, Proc. Rehovoth Conf. Nucl. Structure
                                    (Amsterdam 1958) p. 483

33. A.E. Blaugrund, Proc. Reh. Conf. (1958) p. 542

34. V.A. Sergienko, Izv. Akad. Nauk (SSSR) Ser. Fiz. 22 (1958)
                                    198

35. E. Bashandy, Nucl. Inst. and Meth. 6 (1960) 289

36. H.O.W. Richardson, Phil. Mag. 40 (1949) 233

37. N.J. Freeman, PhD. Thesis (1960) Univ. of Exeter

38. F.P. Bowden and D. Tabor, The Friction and Lubrication of
                                    Solids, Oxford (1954) p. 165

39. Holland, Vacuum Deposition of Thin Films (Chapman and Hall
                                    1956) p. 46

40. A. Hedgran, K. Siegbahn and N. Svartholm, Proc. Phys. Soc. A 63 (1950) 960

41. A. Hedgran, Ark. f. Fysik 5 (1952) 1

42. J.M. Sturtevant, Rev. Sci. Inst. 18 (1947)

43. Ginzton and Hollingsworth, Proc. I.R.E. 29 (1941) 43

44. R.H. Martin and R.D. Hill, A Manual of Vacuum Practice, Melbourne Univ. Press,(1949)

45. J.R. Davy, Industrial High Vacuum, Pitman (1951)

46. B.D. Pate and L. Jaffe, Can. Jour. of Chem. 33 (1955) 15

47. Strong, Modern Laboratory Practice, Blackie (1946) p. 542

48. Holland, Vacuum Deposition of Thin Films (Chapman and Hall) (1956) p. 110

49. W. Parker, M. De Croes and K. Sevier Jr., Nucl. Inst. and Meth. 7 (1960) 22

50 a.L.M. Langer, Rev. Sci. Inst. 20 (1949) 216
 " b.H. Slätis, β- and γ-ray Spectroscopy (Ed. K. Siegbahn, Amsterdam, 1955) p.259

52. V.A. Gorodinskii, Yu.F. Romanov, A.V. Sorokina and M.I. Yakunin, Prib. i Tekh. Exp. Sept-Oct. (1959) 128

53. Elektrie, March (1961) p.61

54. J.M. Meek and J.D. Craggs, Oxford (1953) p. 148

55. R.P. Connor and M.K. Husain, Nucl. Inst. and Meth. 6 (1960) 337

56. Childs, Physical Constants (Methuen) (1933)

57. Parsons, Handbook of Electrochemical Constants (Butterworth) (1959)

58. Vickery, Chemistry of the Lanthanons (Butterworth) (1953) p.228

59. G. Bertiolini, F. Cappellani and A. Rota, Nucl. Inst. and Meth. 9 (1960) 107

60. Yu.A. Egorov and D.S. Chychorev, Prib. i Tekh. Exp. No. 4 (1960) 136

61. E.E. Baroni et al., Prib. i Tekh. Exp. No. 3 (1961) 159

Part II

Key to Figures.

Fig. 1.   Diagram showing the relation between bipolar, spheroidal and cylindrical co-ordinates.

Fig. 2.   Variation of the potential of a particle in a spheroidal field with η at a constant ξ .

Fig. 3.   Contours of equal vector potential in the meridional (y z) plane for a particle projected from the axis of symmetry.

Fig. 4.   Flow diagram for the integration of the equations of motion for a particle starting on the axis.

Fig. 5.   Trajectories for a particle with (momentum)^2 = p^2 = 42.5 and initial co-ordinates ξ_o = -0.6 (z_o/a = -0.6) η_o = 1 (y = 0).

Fig. 6.   Motion in the equatorial plane of a particle shown in Fig. 5 with an angle of projection α = 75°.

Fig. 7.   Set of trajectories for p^2 = 45 and ξ_o = -0.8 (z_o/a = -0.8) η_o = 1 (y = 0).

Fig. 8.   Set of trajectories for p^2 = 45 and ξ_o = -0.7 (z_o/a = -0.7).

Fig. 9.   Continuation of rays from Fig. 8.

Fig. 10.   Set of trajectories for p^2 = 50 and ξ_o = -0.4 η_o = 1.

Fig. 11.   Continuation of trajectories from Fig. 10.

Fig. 12.   Trajectories for a particle starting at ξ_o = 0 η_o = 1 with p^2 = 35.

Fig. 13.   Trajectories for particles starting at different points along the axis but with the same energy (p^2 = 20).

Fig. 14.   Complete set of caustics for ξ_o = -0.7, η_o = 1 corresponding to Figs. 8 and 9.

I

(i)   Introduction.

The knowledge of the motion of an electron in electric
and magnetic fields is of importance in the design of apparatus
which make use of electron focusing such as photomultipliers,
electron microscopes and nuclear spectrometers. In beta ray
spectrometers, magnetic fields of various forms have been more
widely used than electrostatic fields because very high values
of the latter are necessary to produce the same curvature as
conveniently small values of the magnetic fields.

To investigate the focusing properties of a magnetic
field, it is necessary to find the electron trajectories from
the equations of motion. Due to the form of the differential
equations [18] representing the motion, a complete electron
optical solution is often difficult and approximate solutions
have to be found or the electron paths have to be plotted
experimentally [18, 30].

The β-spectrometers fall into two groups, the 'flat'
type and the 'helical' type. In the 'flat' type the electron
paths are perpendicular to the field [7, 8, 25, 28] , and in
the 'helical' type the electrons have a considerable component
of velocity along the direction of the field and the path is in
the form of a helix (Verster 1952, [36]). The analysis of the
focusing properties of a 'flat' spectrometer is simpler because

the focusing properties are governed by B(r) (r being the distance to the axis of symmetry) which can be expanded in the form of a series, of which the first term determines the momentum of the electrons and higher terms determine the focusing quality, i.e. the aberrations. A form of focusing in a 'flat' spectrometer first suggested by Myamoto, where the electron trajectories are determined by B(r) at every point, have been recently investigated by Bastard [1, 2], Burdet [5] and Lukashev [20].

In the 'helical' or lens spectrometers the analysis is difficult because the motion of the electrons is governed by the whole function B(z) which is the field in the direction of the z axis. The focusing properties of a uniform field can be given an exact form because they can be analysed theoretically. These have been studied by Witcher (1941) [37], Du Mond (1949) [12], Persico (1951) [24] and Hubert (1952) [16]. A modified form of field was studied by Ramburg and Blaugrund (1957) [26].

An analytical form of a field (the spheroidal field) in which the function B(z) is known and the equations of motion can be integrated numerically has been suggested by Richardson (1949) [27]. The spheroidal field is of special interest because it was used as a basis in the design of the spheroidal field spectrometer [4] and the large spectrometer [13] used in the work described in Part I. In [27] only a few trajectories were found because the equations were very cumbersome. In the present

work the focusing properties of the spheroidal field were investigated by integrating the equations of motion numerically using the 'Mercury' electronic computer of the University of London. It was found from the trajectories that the field in the spectrometer is not truly spheroidal and an attempt was made to find the theoretical field form by superposing a uniform magnetic field on the spheroidal field.

(ii)   Equations of motion of a particle in an axially symmetric magnetic field.

It has been shown by Dosse (1936) [11], Klemperer [18a], that the problem of the motion of an electron in a field with axial symmetry can be simplified by considering the two-dimensional motion in two perpendicular planes, the ~~equatorial~~ *azimuthal* plane at right angles to the axis of symmetry which travels with the component of velocity along the axis, and the meridional plane containing the axis and rotating with the particle about the axis.

The general equations of motion of a particle mass m and charge e (e.m.u.) were obtained from the relativistic Lagrangian L [23]

$$L = -m_o c^2 \sqrt{(1 - v^2/c^2)} + e(v \cdot A) \tag{1}$$

where A is the vector potential defined by B = curl A (if μ = 1 in vacuo B will be numerically equal to the field

intensity H), and **v** is the velocity of the particle. Using

the cylindrical co-ordinates y, ϕ, z,

$$v = V_z \dot{i}_1 + V_y \dot{i}_2 + V_\phi \dot{i}_3 \qquad (2)$$

(i_1, i_2, i_3 are the unit vectors)

and Lagrange's equation

$$\frac{d}{dt}\left(\frac{\partial L}{\partial \dot{q}_r}\right) = \frac{\partial L}{\partial q_r} \qquad (r = 1, 2 \ldots) \qquad (3)$$

(q_r - generalized co-ordinate)

the equations of motion were found.

The differentiation of L is simplified if the field

has axial symmetry, since A_ϕ only exists ($A = A\phi$) [31] and

$$\text{since } \frac{\partial A}{\partial \phi}\phi = 0 \text{ but } \frac{\partial A}{\partial y}\phi \neq 0 \quad \frac{\partial A\phi}{\partial z} \neq 0.$$

On differentiating (1) and substituting into (3) the equations

of motion become

$$m\ddot{y} = -\frac{1}{2m}\frac{\partial}{\partial y}\left(\frac{c}{y} - eA\right)^2 \qquad (4)$$

$$m\ddot{z} = -\frac{1}{2m}\frac{\partial}{\partial z}\left(\frac{c}{y} - eA\right)^2 \qquad (5)$$

$$m y\dot{\phi} = \frac{c}{y} - eA \qquad (6)$$

where C is a constant depending on the initial conditions.

From the form of the equations it can be seen that the motion in the y z (meridional) plane is that of a particle obeying Newton's laws of motion in a conservative field with a scalar potential energy

$$V = \frac{1}{2m}\left(\frac{C}{y} - eA\right)^2 \tag{7}$$

and the problem can be treated as if the particle is not relativistic.

$$\text{if} \quad \frac{1}{2}m\left(\dot{y}^2 + \dot{z}^2 + (y\dot{\phi})^2\right) = \frac{1}{2}mv^2 = \text{const}$$

$$\frac{1}{2}m\left(\dot{y}^2 + \dot{z}^2\right) + \frac{1}{2m}\left(\frac{C}{y} - eA\right)^2 = \text{const} \tag{8}$$

since the speed of a particle in a magnetic field is constant. $1/2\ m(\dot{z}^2 + \dot{y}^2)$ is the kinetic energy in the meridional plane and the second term on the left hand side of (8) is the potential energy which is in fact the kinetic energy in the equatorial plane.

(iii)   Relation between the co-ordinate systems.

Three co-ordinate systems were used in the equations simultaneously to simplify their form, the bipolar co-ordinates, cylindrical co-ordinates and spheroidal co-ordinates [22, 32].

If the co-ordinates of a point P, Fig. 1, are

Fig. 1. Diagram showing the relation between the three sets of the co-ordinates used.
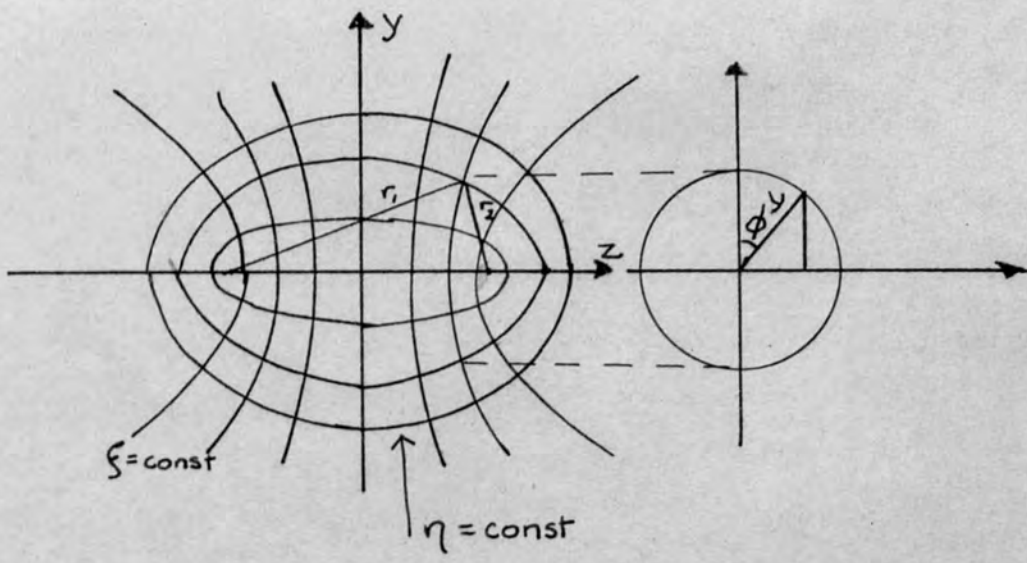
$\xi = const$

$\eta = const$

Fig. 2
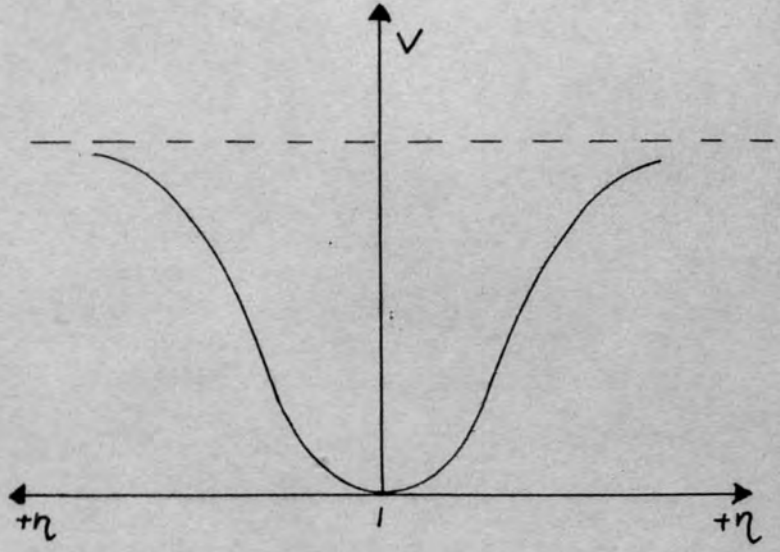
(a) Case of particle starting on the axis, C = 0.

Variation of the potential V with η at constant ξ. Dotted line is the limit of V when $\eta \to \infty$ which is given by

$$V_0 = \frac{e(a^2 H_0)^2}{(1-\xi^2)\, 2m}$$
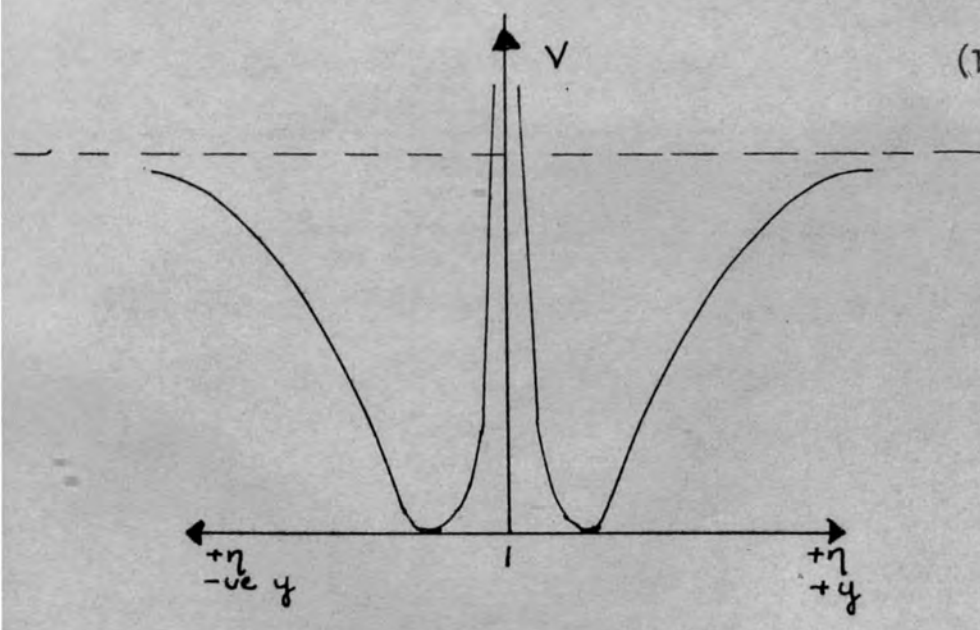
(b) Case of particle starting on a ring source, $C \neq 0$. Variation of potential V with η at constant ξ.

Dotted line shows limit of V as $\eta \to \infty$ which is given by

$$V_0 = \frac{(e a^2 H_0)^2}{2m\,(1-\xi^2)}$$

$+\eta$ 1 $+\eta$

$+\eta$
$-ve\ y$ 1 $+\eta$
$+y$

r_1, r_2, ϕ, in bipolar co-ordinates

y, z, ϕ, in cylindrical co-ordinates

η, ξ, ϕ, in prolate spheroidal co-ordinates

the relations between them can be obtained from Fig. 1 and
are

$$\eta = \frac{r_1 + r_2}{2a} \qquad \xi = \frac{r_1 - r_2}{2a} \tag{9}$$

$$r_1^2 = y^2 + (z+a)^2 \qquad r_2^2 = y^2 + (a-z)^2 \tag{10}$$

$$z = a\eta\xi \qquad y = a\sqrt{(1-\xi^2)(\eta^2-1)} \tag{11}$$

where 2a is the distance between the foci of the spheroids.
The range of values taken by η and ξ are

$$\eta \geq 1 \quad , \quad -1 \leq \xi \leq 1 \tag{12}$$

(iv)   The spheroidal field.

The scalar potential energy of the spheroidal field
can be found at any point by substituting the value of A
for the spheroidal field into (7). A was determined by
Richardson [27] and is given by

$$A = \frac{a^2 H_0 (\eta-1)}{y} \tag{13}$$

where H_0 is the field at the centre of co-ordinates.

Therefore

$$V = \frac{1}{2m}\left(\frac{C - ea^2 H_0(\eta - 1)}{y}\right)^2 \tag{14}$$

Some general ideas on the motion of the electron can be obtained from the properties of V.

For a particle starting on the axis C = 0 and

$$V = \frac{1}{2m}\left(ea^2 H_0 \frac{(\eta - 1)}{y}\right)^2 \tag{15}$$

The nature of the variation of V with η , at a constant value of ξ , is shown in Fig. 2a. If y = 0 (η = 1) then V = 0 (if z $\neq$ a), since $\frac{\eta - 1}{y} \sim \frac{y}{2(a^2 - z^2)}$ for $\frac{y}{a} \ll 1$ which is zero if y = 0. V is infinite at z = a.

The variation of V with η at constant ξ for a particle starting on a ring, i.e. C $\neq$ 0, is shown in Fig. 2b. If the initial co-ordinate $\eta = \eta_0$ and the particle has no component of velocity perpendicular to the meridional plane $\left[(y\dot{\phi})_{\eta = \eta_0} = 0\right]$ V is zero when $\eta = \eta_0$. If, however, the particle starts with a velocity at an angle to the meridional plane, Fig. 26 and 27, V will go through a minimum as η varies but may not become zero. C depends on the angle between v and the meridional plane, and may become negative. V will then be zero for a value of η determined by the numerator of (14) only if C is positive, and will have a minimum if C < 0.

V rises steeply as $\eta \to 1$ (i.e $y = 0$) if $C \neq 0$.
This is due to the term C/y in (14) since C is finite and
$y \to 0$. V is now infinite along the z axis, which means that
if a particle starts on a ring and has initial conditions such
that $C \neq 0$, its path cannot intersect the axis.

In both the above cases ($C = 0$, $C \neq 0$) V tends to the
finite limit $V_0 = \dfrac{(e a^2 H_0)^2}{2m(1-\xi')}$ as $\eta \to \infty$. This means that
the particle is trapped in the field and will only be able to
escape if it has an energy exceeding the minimum value of

$$V_0 = \frac{(ea^2 H_0)^2}{2m}$$

(v)   The equipotentials of the spheroidal field.

Some contours for which V is constant with $C = 0$ are
shown in reference [27]. Several of these have been recal-
culated with the value of H_0 used in the present work and are
shown in Fig. 3. Those for $C \neq 0$ have also been computed by
separating the variables in equation (14) which may be written
as

$$2mV = \left(\frac{C - ea^2 H_0(\eta - 1)}{y} \right)^2$$

$$\frac{2mV}{(ea^2 H_0)^2} = \frac{\left(C/ea^2 H_0 - (\eta - 1) \right)^2}{y^2} \tag{16}$$
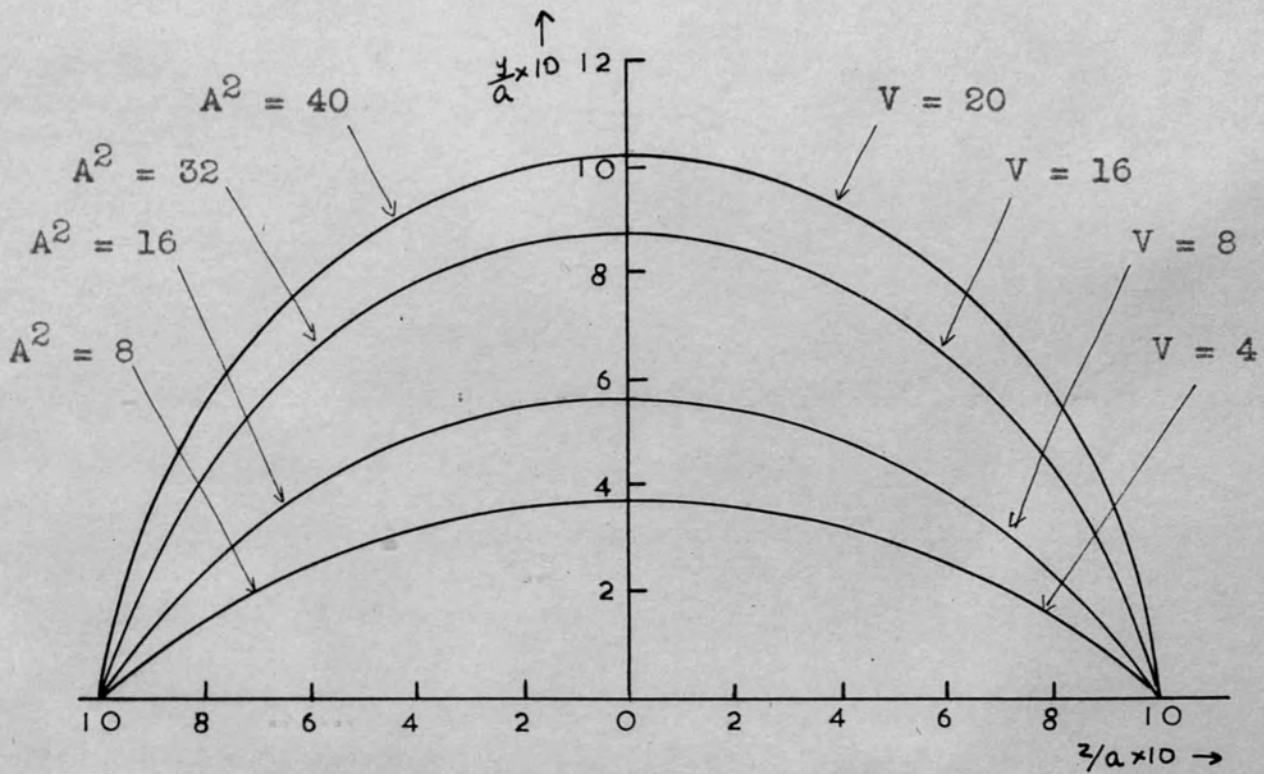
Fig. 3. Contours of equal vector potential in the meridional (yz) plane for a particle projected from the axis of symmetry z. Since $V = e^2A^2/2m$, these also represent contours of equal V ($e/m = 1$ and $m = 1$).

putting

$$\frac{2mV}{(ea^2H_0)^2} = V' \quad \text{and} \quad \frac{C}{ea^2H_0} + 1 = C' \tag{17}$$

$$V' = \frac{(C'-\eta)^2}{y^2} \tag{18}$$

On substituting for y using equation (11) and rearranging, (18) takes the form

$$V'a^2(1-\xi^2) = \frac{(C'-\eta)^2}{\eta^2-1} \tag{19}$$

The variables are now conveniently separated and the values of ξ and η , and therefore z and y for any locus of constant V can be found. ξ was chosen as the independent variable and after evaluating the left hand side of (19), the quadratic equation for η was solved, with the conditions that η must be real and $\eta \geq 1$ for the solutions to be significant. It was confirmed by calculations that there is only one real root for $V > V_o$, i.e at $\eta < \eta_o$, and two for $V < V_o$.

II

Case for a particle starting on the axis of symmetry.

(i)   Equations of motion.

For a particle starting on the axis of symmetry, the z axis $C = 0$ and the equations (4), (5) and (6) take the following form

$$m\ddot{y} = -\frac{e^2}{2m} \frac{\partial}{\partial y} A^2 \tag{20}$$

$$m\ddot{z} = -\frac{e^2}{2m} \frac{\partial A^2}{\partial z} \tag{21}$$

$$m y^2 \dot{\phi} = -eAy \tag{22}$$

where $A = \dfrac{a^2 H_0 (\eta - 1)}{y}$

H_0 is the field at the centre of the co-ordinates

y, z are co-ordinates in the rotating meridional plane.

When A is substituted into (20), (21), (22), the equations take the following form

$$\ddot{y} = -\left(\frac{a^2 H_0 e}{m}\right)^2 \left(\frac{\eta - 1}{y}\right) \left[\frac{1}{2a}\left(\frac{1}{r_1} + \frac{1}{r_2}\right) - \frac{\eta - 1}{y^2}\right] \tag{23}$$

$$\ddot{z} = -\left(\frac{a^2 H_0 e}{m}\right)^2 \left(\frac{\eta - 1}{2ay^2}\right) \left(\frac{z + a}{r_1} - \frac{a - z}{r_2}\right) \tag{24}$$

$$\dot{\phi} = -\left(\frac{e a^2 H_0}{m}\right) \left(\frac{\eta - 1}{y^2}\right) \tag{25}$$

Fig. 4. Flow diagram for the programme for integrating the
equations of motion of a particle starting on the axis.
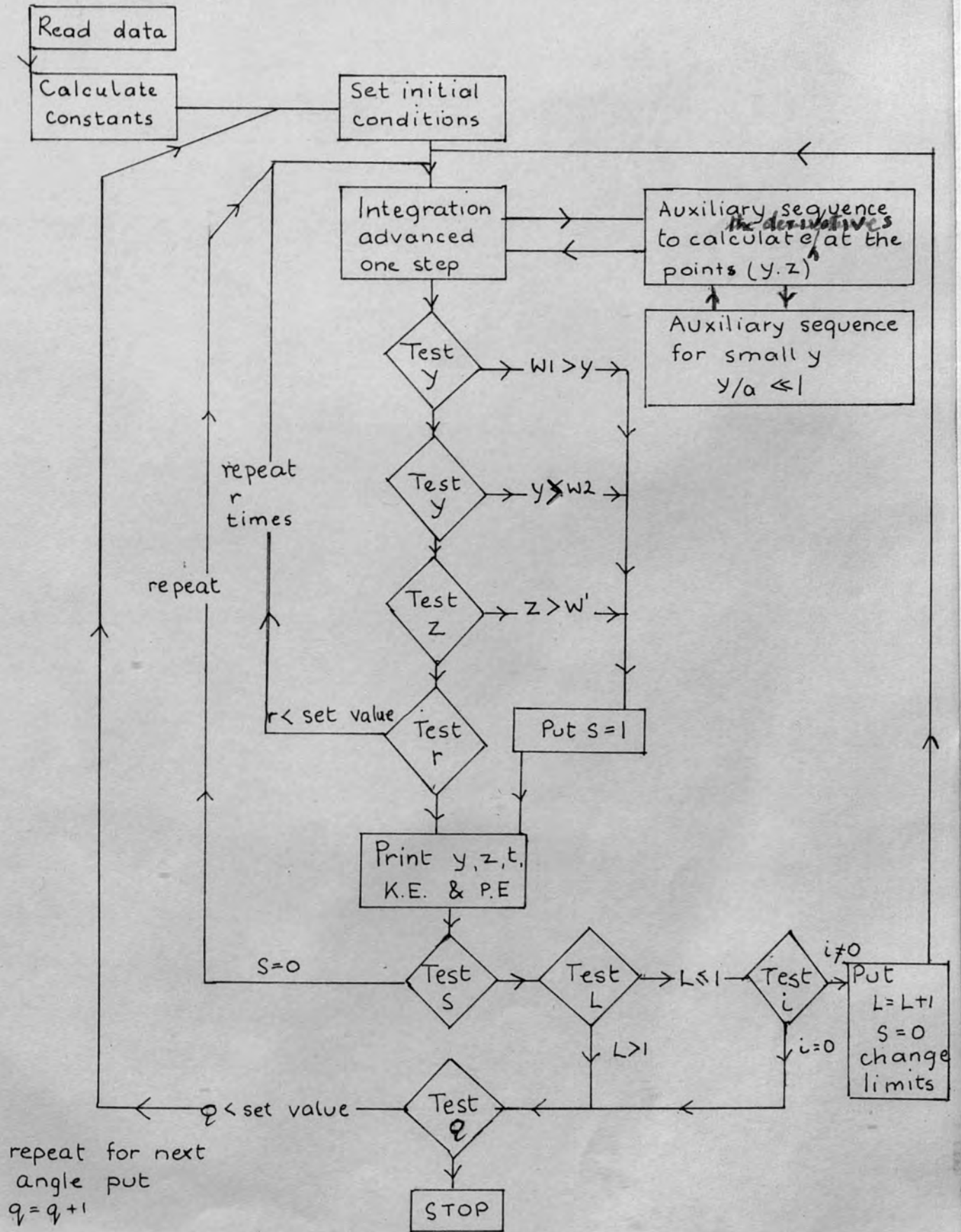
where the co-ordinates used are defined in I (iii). 2a is
the distance between the foci of the system of spheroids.

(ii)   Solution of the equations of motion.

The two second order equations (23) and (24) were
written as for first order simultaneous equations. If we put
$y = y_1$ and $z = y_3$, then the equations can be written as

$$\frac{dy_1}{dt} = y_2 = f_1$$

$$\frac{dy_2}{dt} = f_2$$

$$\frac{dy_3}{dt} = y_4 = f_3 \tag{26}$$

$$\frac{dy_4}{dt} = f_4$$

and integrated using a modified form of the Runge-Kutta
method [15, 21]. The truncation error per step was u^5, where
u is the step size. The flow diagram for the integration is
shown in Fig. 4. The initial data were first read in. These
included the initial momentum, angle of projection denoted
by α, initial position, the limits of y and z (w_1, w_2 and w')
at which the integration is to stop, the number of steps (r)
that the integration is advanced before the results are printed
(frequency of printing) and the number of trajectories (q) to
be found with the same initial conditions but differing in the
angle of projection by a predetermined amount.

It was pointed out by Richardson [27] that the size
of the orbits are invariant under any transformation which
leaves $\frac{He}{mv}$ unchanged, where the momentum $p = mv$. We may
therefore choose $m = 1$ for the computation and vary v, then

$$v = \frac{v'}{\sqrt{1 - \frac{v'^2}{c^2}}} \quad,$$ where v' is the velocity of the particle.

Only the ratio $\frac{e}{m}$ appears in the equation, and this was chosen
to be equal to unity. The above choice is equivalent to choosing
the Bρ since B$\rho = \frac{mv}{e}$. In all the computations $H_o = 1.5$, $a = 10$.

The points on the trajectory near the caustic, where
the curvature is a minimum, are more closely spaced even though
the step length (in time) is the same due to the fact that the
velocity in the y-z plane decreases and the particle covers
less distance in the same time.

It can be seen from the flow diagram that the integ-
ration will stop after the particle has crossed the axis once
if $i = 0$, where i is an integer set with the initial conditions,
and three times if $i \neq 0$, so that the focusing of a particle
which had crossed the axis more than once could be investigated
by a method analogous to that used for flat spectrometers by
H. Daniel (1960) [7] and Daniel and Laslett (1960) [8].
Approximate relations were used in place of (23) and (24) for
very small values of y, $y/a \ll 1$, since y appears in the denominator
and there is a danger of exceeding the range of the computer
when the particle is very close to the axis. The following

expression were used for $y/a < 0.001$

$$\ddot{z} = - \left(\frac{a^2 H_0 e}{m} \right)^2 \frac{z\, y^2}{2(a^2-z^2)^3} \tag{26}$$

$$\ddot{y} = - \left(\frac{a^2 H_0 e}{m} \right)^2 \frac{y}{4(a^2-z^2)^2} \tag{27}$$

The hand computed trajectories of reference 27 were used
to check the programme.

The integration was checked by computing the potential
and kinetic energy in the meridional plane (the physical
significance of which was mentioned earlier) every r steps.
The sum of these should remain constant to the required
accuracy since the particle moves in a conservative field.
The deviation from the initial energy was not allowed to
exceed 5 parts in 20 000. If the step size was too large,
the programme incorrect or the initial data not correct,
large deviations from the initial total energy were immediately
observed.

(iii) <u>Properties of the trajectories for a particle starting
on the axis.</u>

Sets of trajectories (i.e. trajectories with angles
of projection differing by 10° or less and other identical
conditions) were computed for various initial conditions.
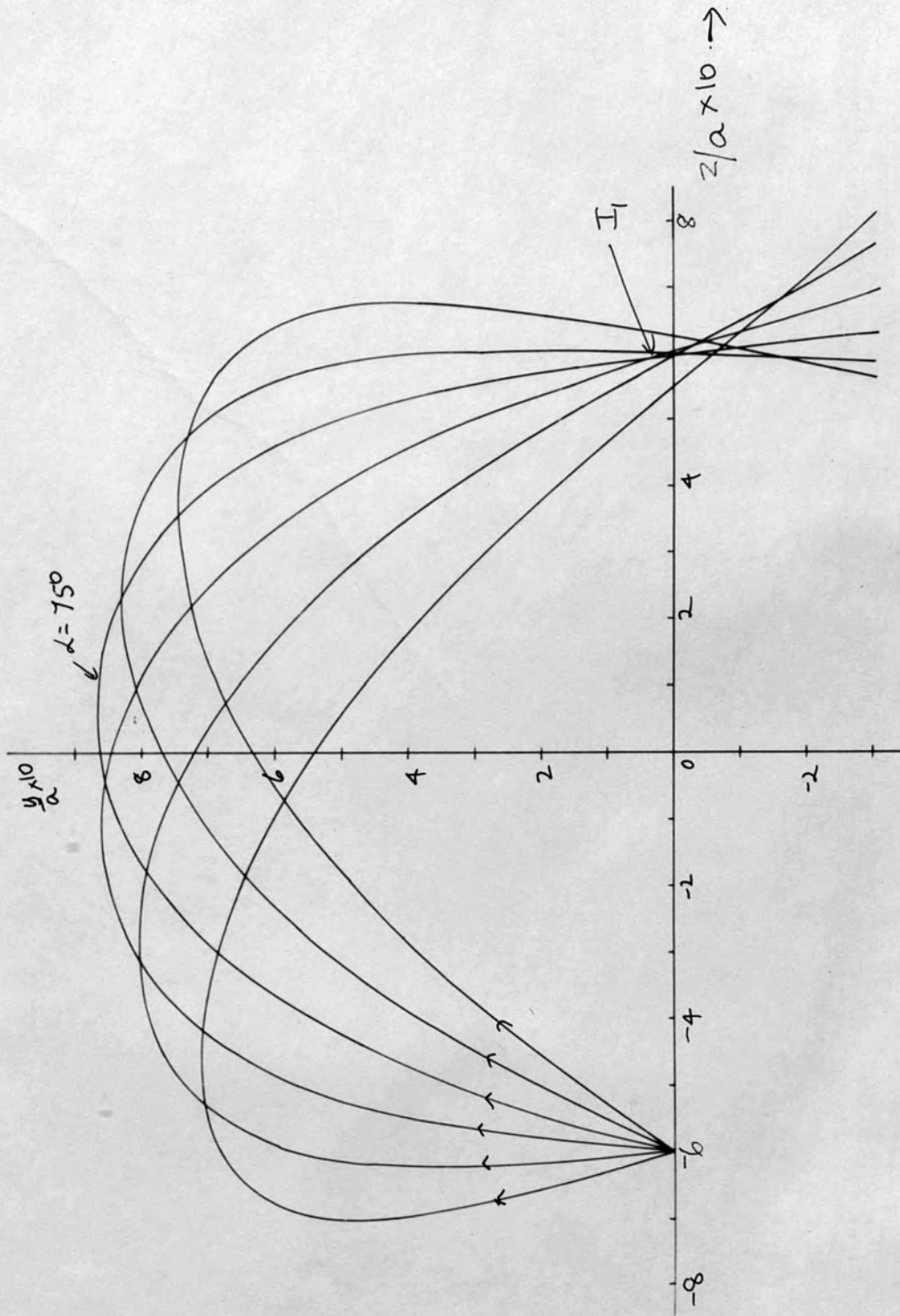
Fig. 5. A set of trajectories with $(momentum)^2 = p^2 = 42.5$. The values of α are 55, 65, 75, 85, 95, 105.
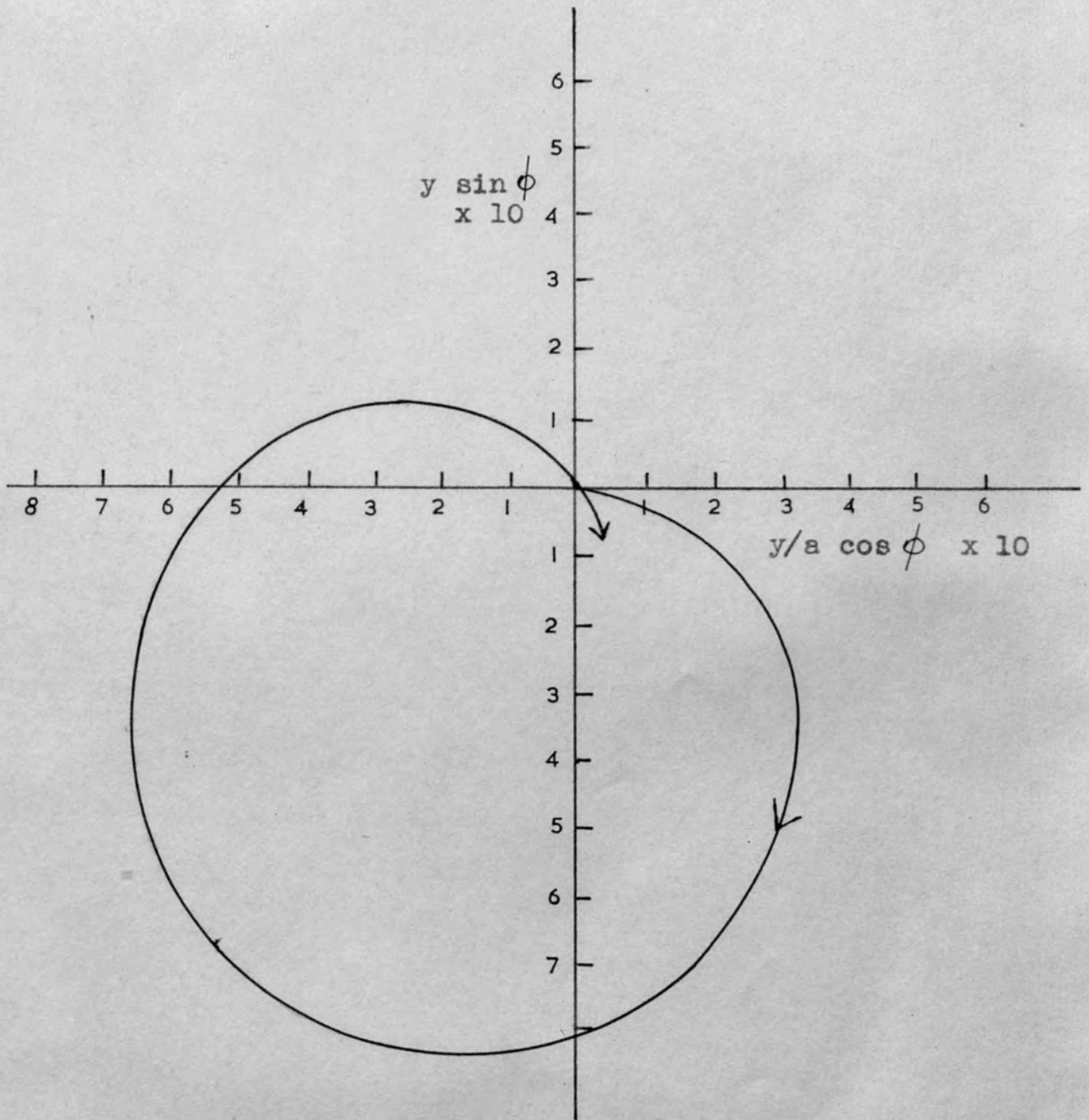
Fig. 6. Motion in the equatorial plane of a particle arrowed
in Fig. 5. The angle of projection α = 75°.
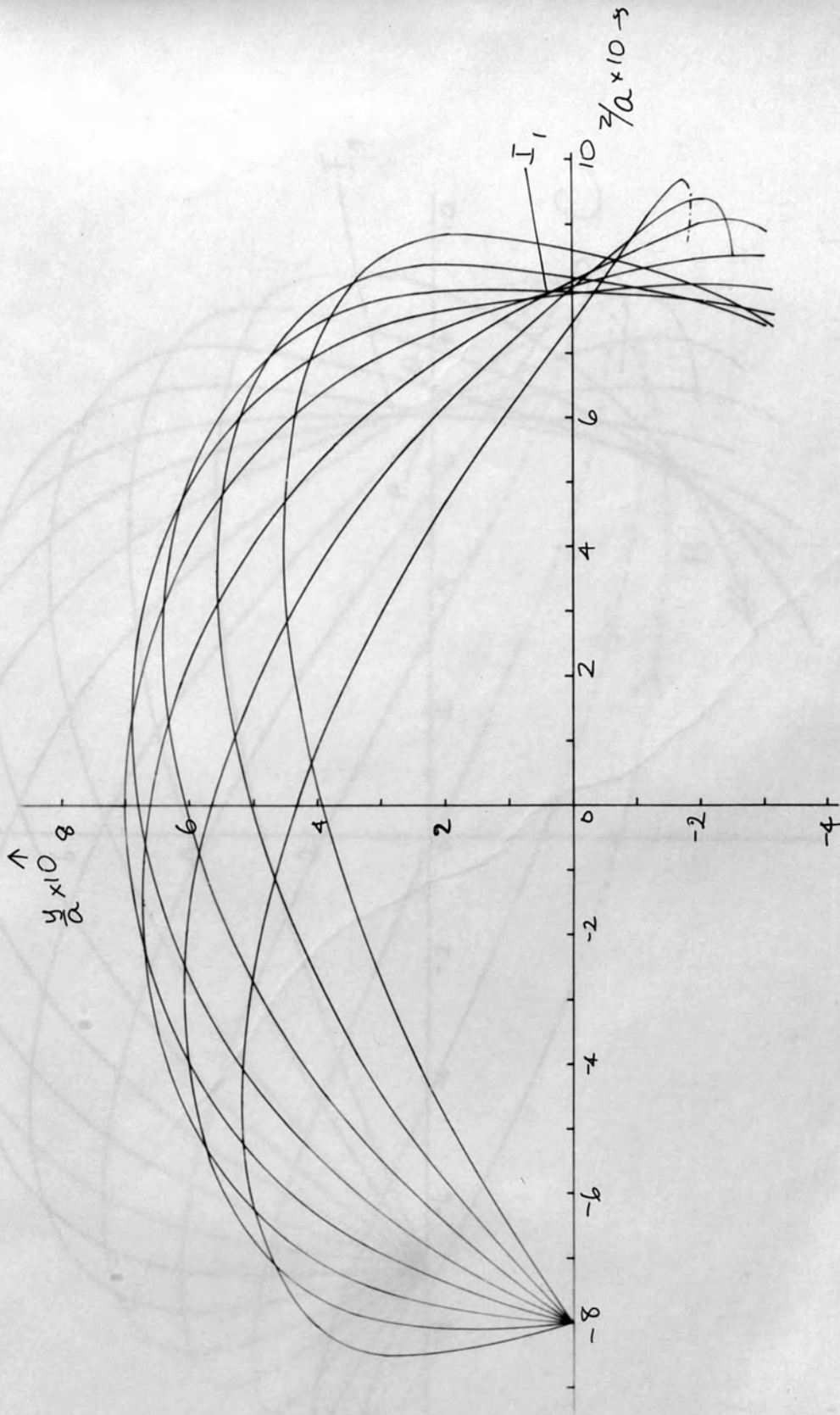
Fig. 7. Set of trajectories in the meridional plane for $p^2 = 45$ and $\xi_0 = -0.8$.
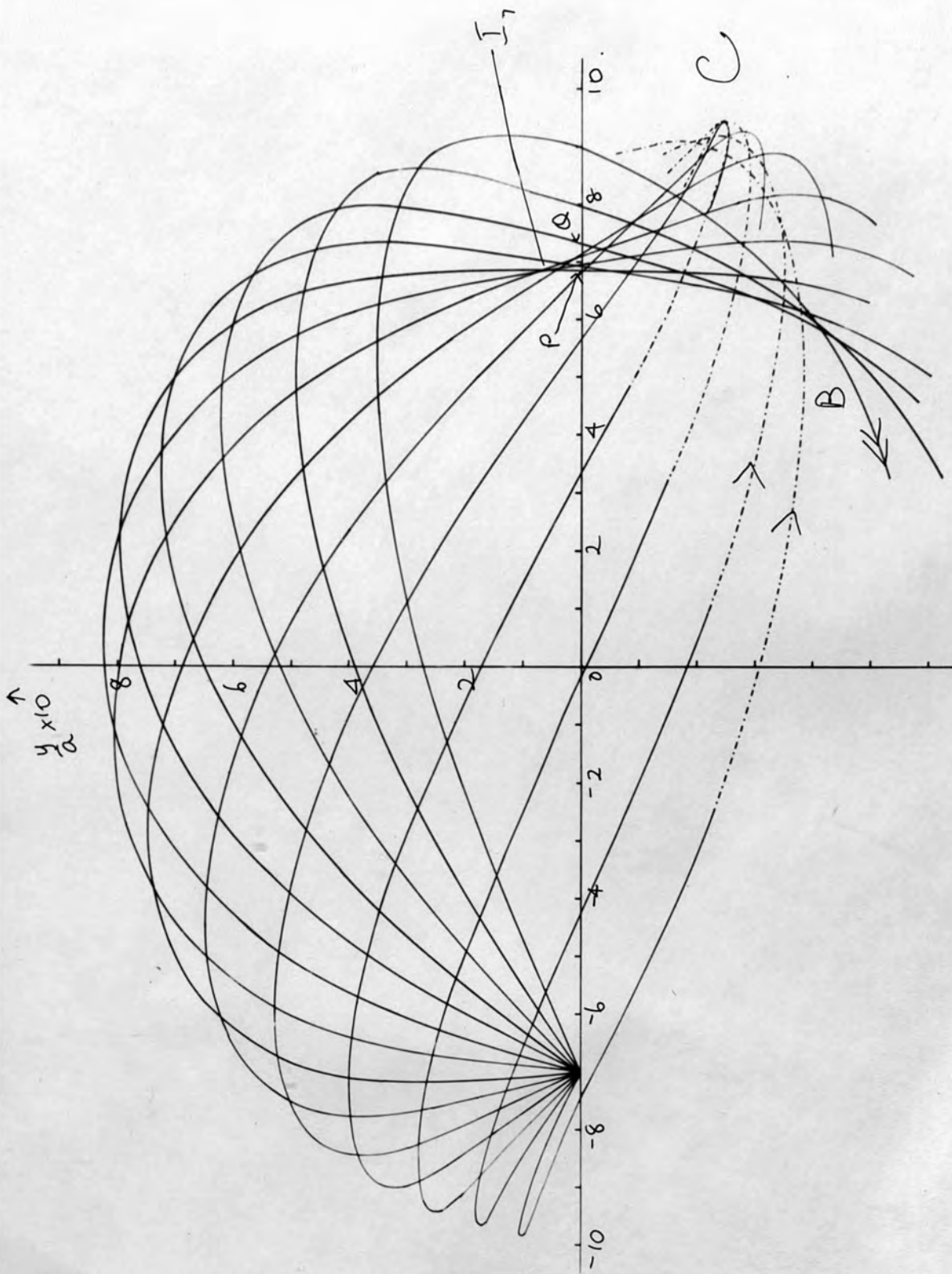
Fig. 8. Trajectories in the meridional plane for a particle with (momentum)^2 = p^2 = 45 and ξ_o = -0.7. The points B and C are marked in Fig. 9.
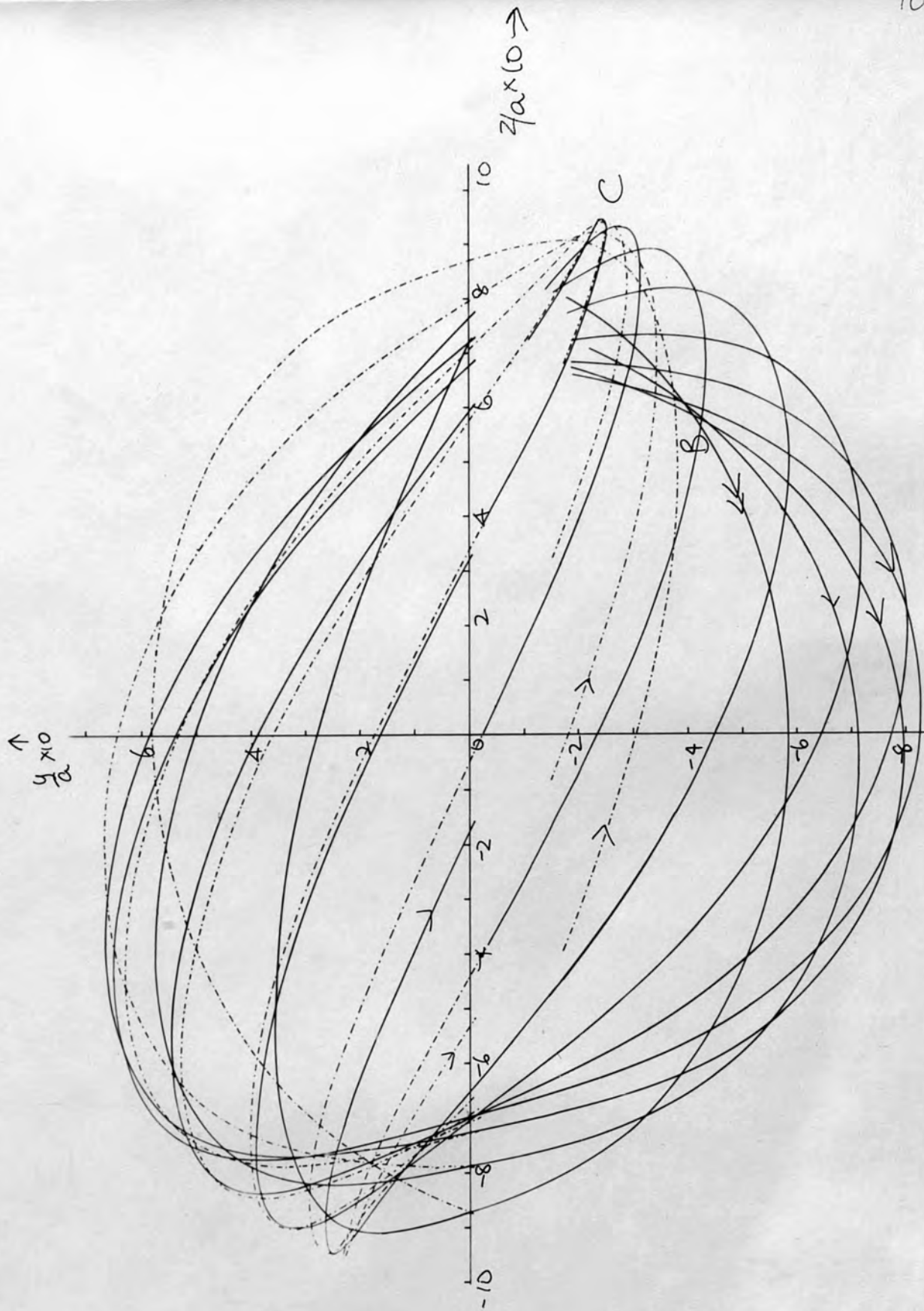
Fig. 9. Continuation of trajectories in Fig. 8. The points B and C are the same as in Fig. 8. The trajectory with the double arrow has been similarly marked in Fig. 8.
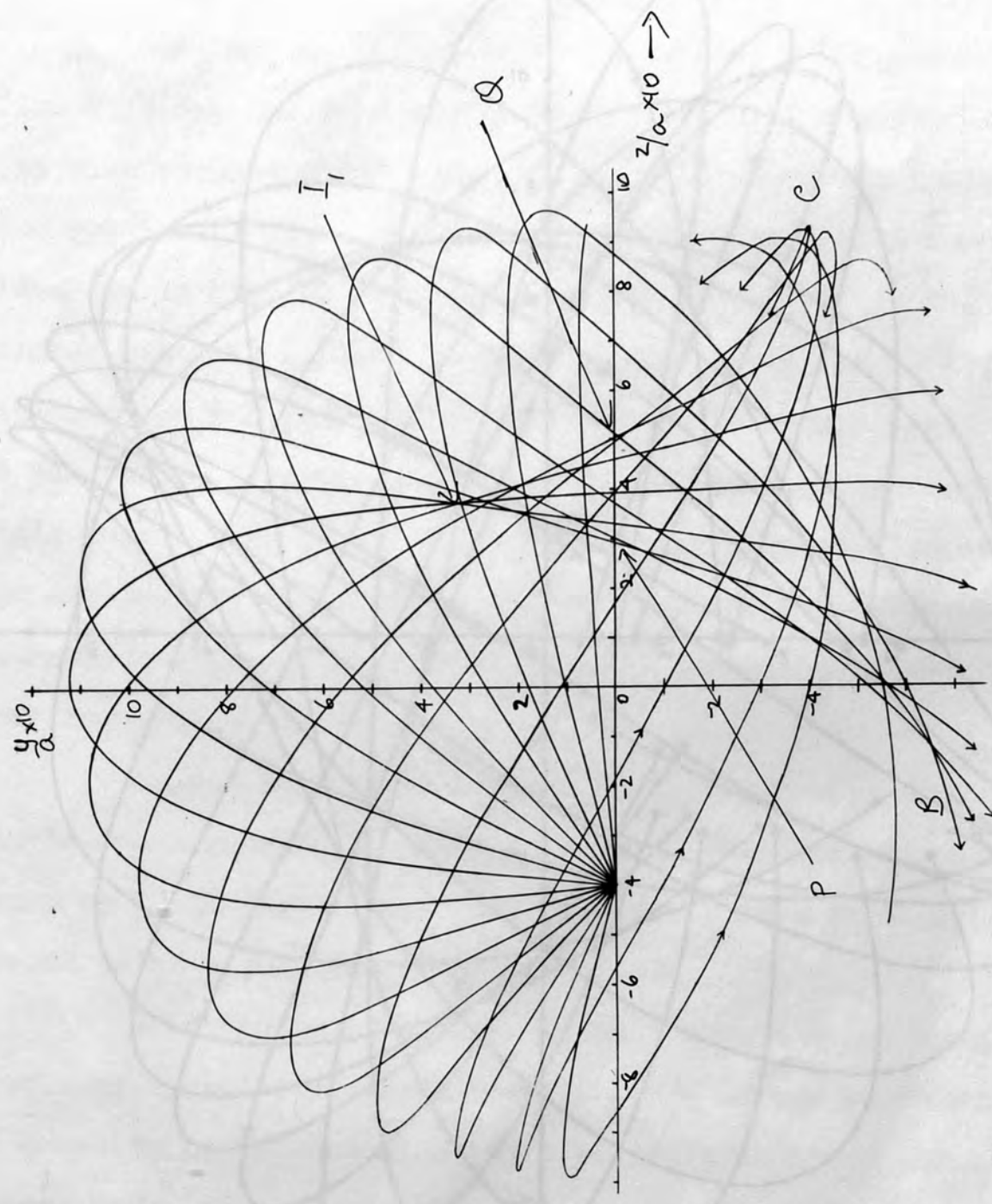
Fig. 10. Trajectories in the meridional plane for a particle with $p^2 = 50$. The formation of the cusp I_1 by two caustics can be seen easily.

Fig. 11. Continuation of trajectories in Fig. 10 in the
meridional plane, $p^2 = 50$. B and C are marked as in Fig. 10.

Some of the trajectories are shown in Fig. 5-13.
Fig. 5 is typical of a set of trajectories of a particle that
has been stopped after crossing the axis once. The motion in
the equatorial plane of the particle projected with $\alpha = 75^{\circ}$
is shown in Fig. 6. The corresponding trajectory in the meri-
dional plane is arrowed in Fig. 5. In Figs. 8 and 10 the
integration has been continued further. To obtain Figs. 8 and
9 the integration was stopped after the particle crossed the
axis three times ($i \neq 0$ in the programme). The continuation
of any trajectory in Fig. 8 can be found by following the
corresponding path in Fig. 9. Fig. 11 shows the continuation
of trajectories in Fig. 10.

It can be seen from Figs. 5, 7, 8, 10 that the trajec-
tories have certain features in common. They all have a focus
such as I_1 in Fig. 7 where the density of rays is high. I_1
seems to be a junction of two caustics.

Each trajectory is reflected from the upper caustic
(primary caustic) whose position depends on the momentum.
A complete set of caustics for a particle crossing the axis
three times is shown in Figs. 14 and 15. Fig. 14 was obtained
from Figs. 7 and 8. The corresponding points have been labelled
with the same letters. Fig. 15 was obtained from Figs. 10 and
11. It can be seen that the Figs. 14 and 15 have similar
features.

The position of the focus I_1 varies with momentum.
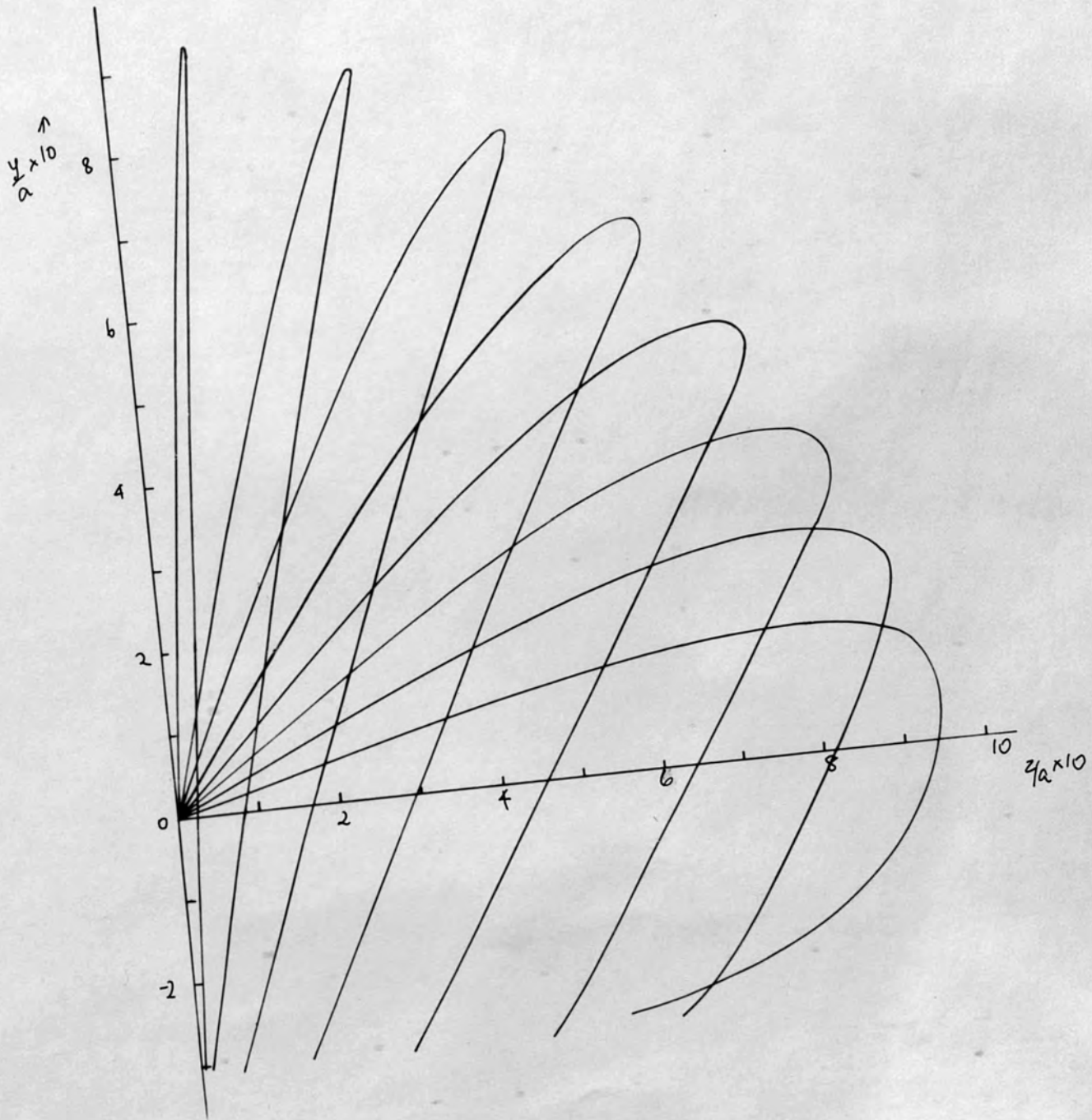
Fig. 12. Trajectories for a particle in the meridional plane in the spheroidal field with $p^2 = 35$.
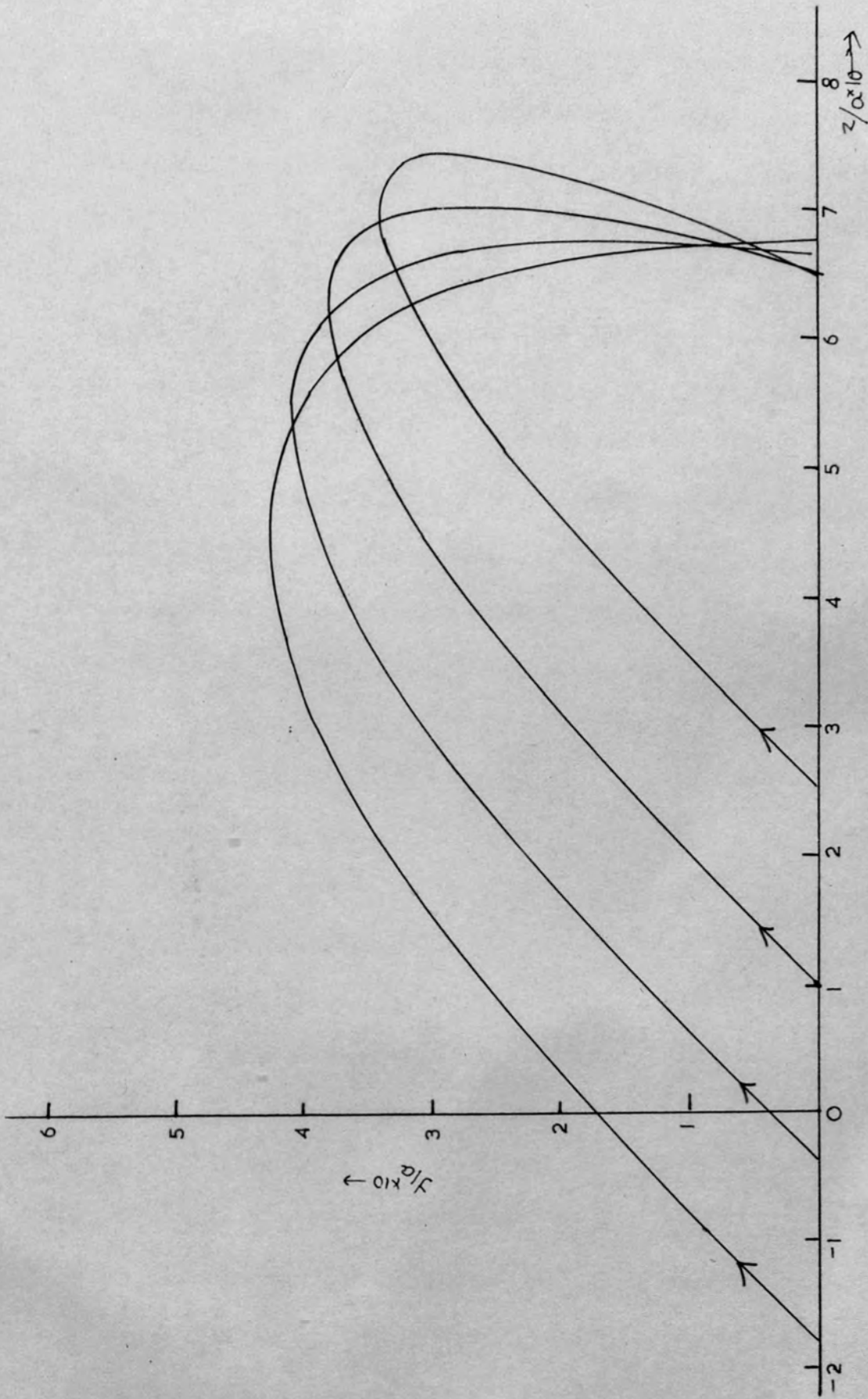
Fig .13. Trajectories for a particle starting at different points along the axis with equal angles of emission and the same momentum ($p^z = 20$)

It moves away from the z axis with increasing energy and nearer to the axis with decreasing energy and may be below the axis for sufficiently small momenta. The variation of the position of the focus I_1 with energy for particles starting at $\xi_o = -0.6$ ($z_o/a = -0.6$) is shown in Fig. 18 curve (a). The curve (b) shows the variation of the position of I_1 with the starting point for trajectories having the same momentum ($p^2 = 45$).

The variation of the length of the intercept such as PQ in Fig. 14 with momentum is plotted in Fig. 16 (for $\xi_o = -0.6$). PQ clearly becomes zero when I_1 is on the axis. From this curve, the momentum corresponding to a chosen position of the focus I_1 can be found. It is very close to the axis for $p^2 = 42.5$. For this position of I_1, $\dfrac{B}{H_o} = \dfrac{\sqrt{42.5}}{1.5}$ (= 4.346) (H_o was chosen as 1.5). Therefore to focus electrons with $B\rho = 4346$ starting at $\xi_o = -0.6$ using a detector on the axis at the position of I_1, the field at the centre must be 1000 oersteds.

The positions of the primary caustic for different momenta for a particle starting at $\xi_o = -0.6$ are shown in Fig. 20. Such sets of curves were used for finding the dispersion in the plane of the slit. The variation of the y co-ordinate with (momentum)$^2 = p^2$ in different z planes has been plotted in Fig. 21 using the curves of Fig. 20. It appears that y_c (value of y at the caustic) varied linearly with p^2 in the
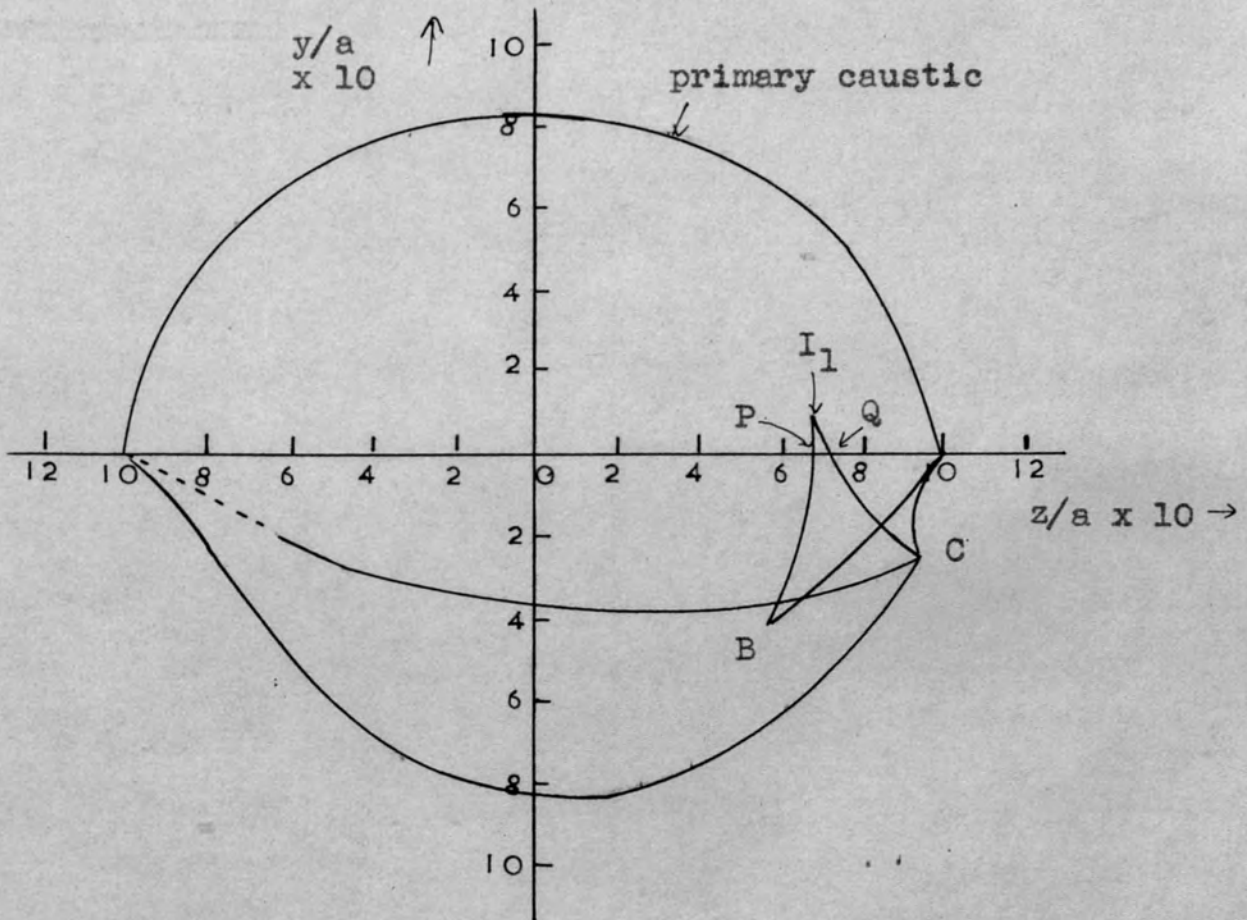
Fig. 14. Complete set of caustics for a particle starting at $\xi_0 = z_0/a = -0.7$, $y_0/a = 0$ with $p^2 = 45$ obtained from Fig. 8 and 9.
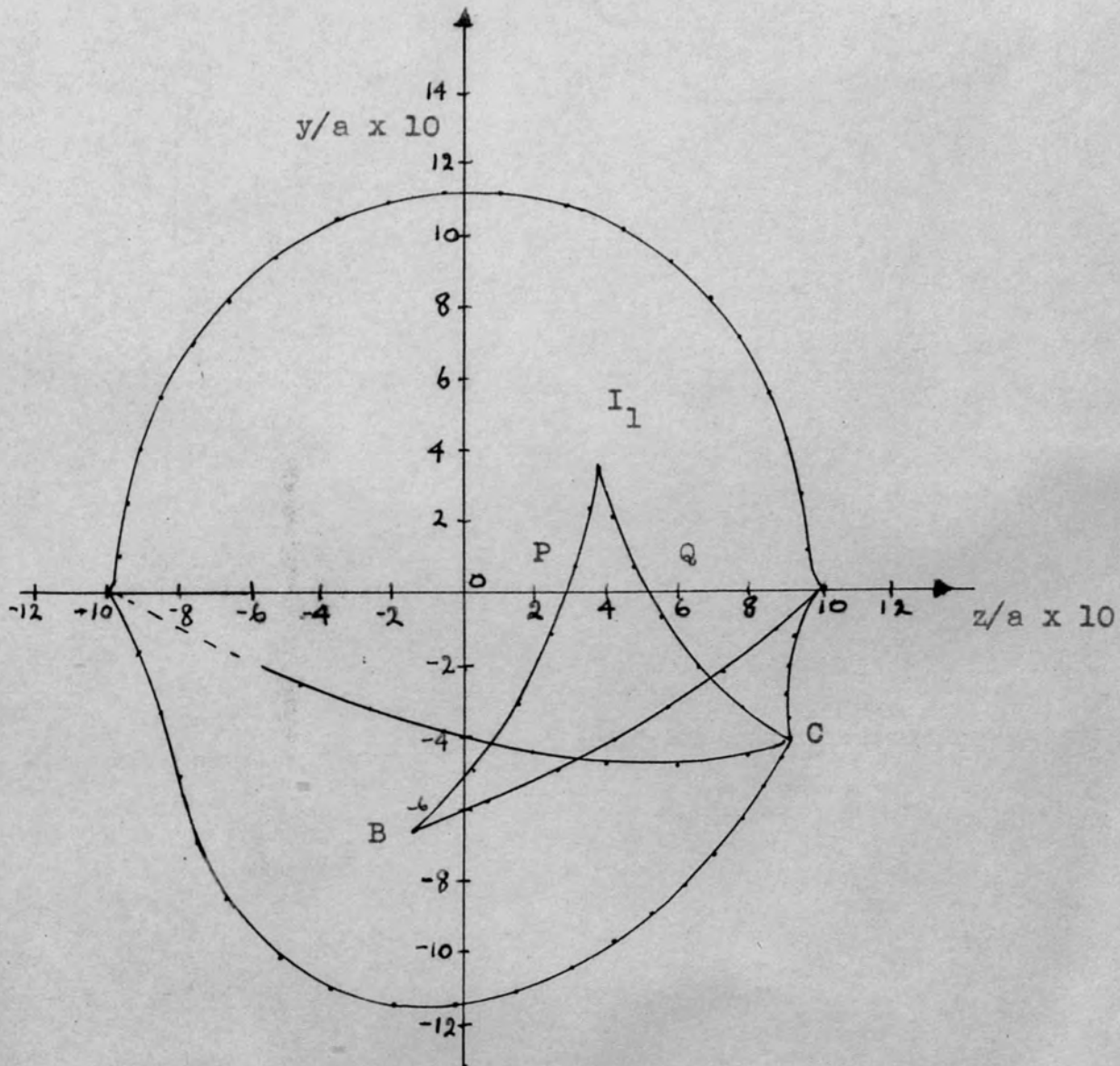
Fig. 15. Complete set of caustics for a particle starting on the axis at $z_0/a = -0.4$ and $(momentum)^2 = p^2 = 50$ and crossing the axis three times. The caustics were obtained from Figs. 10 and 11.

Fig. 16. Variation of the length of the intercept such as PQ in Fig. 15 with p².
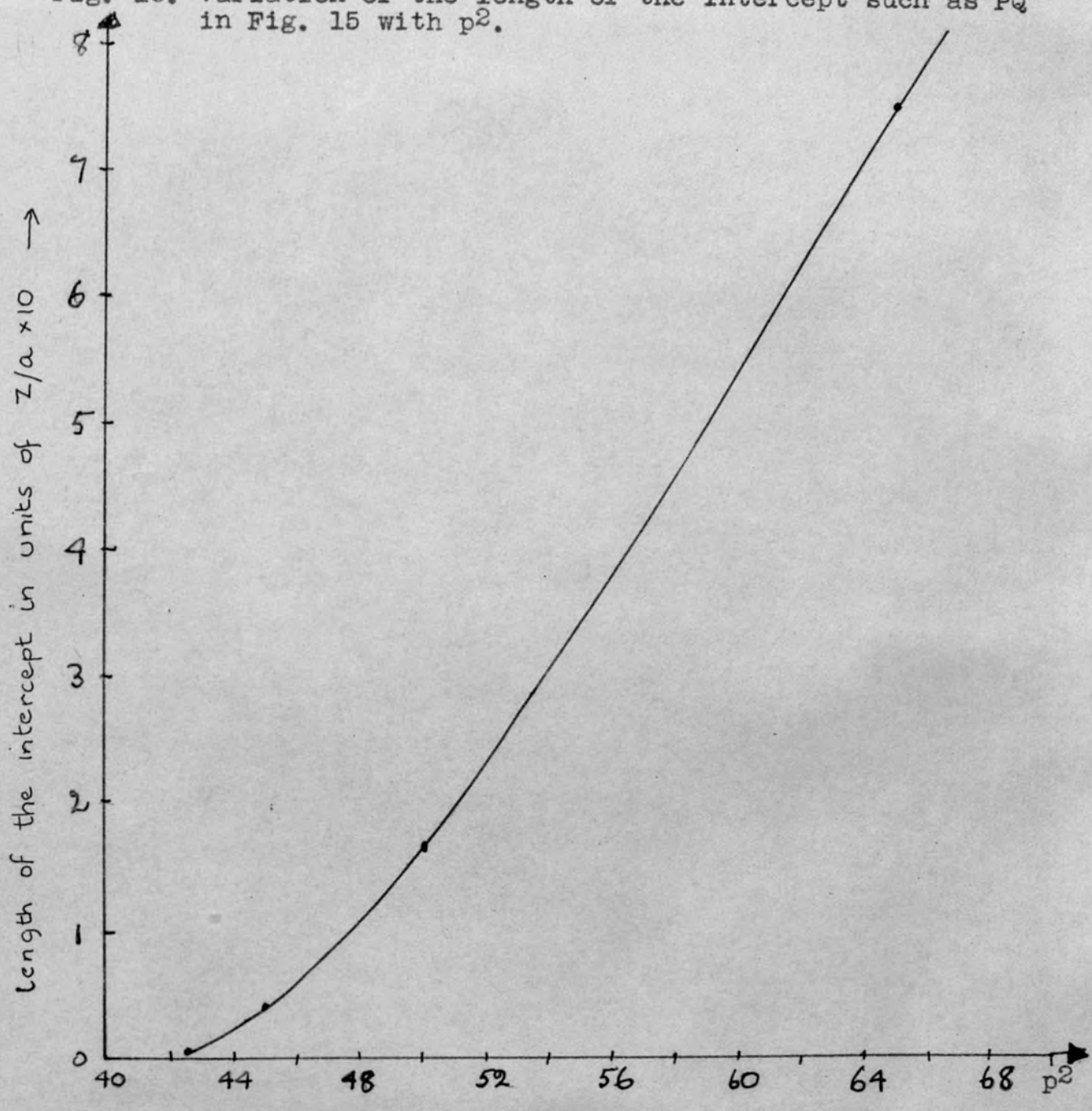
Fig. 17. Variation of the length of the intercept PQ on the z axis starting point for particles with the same p².
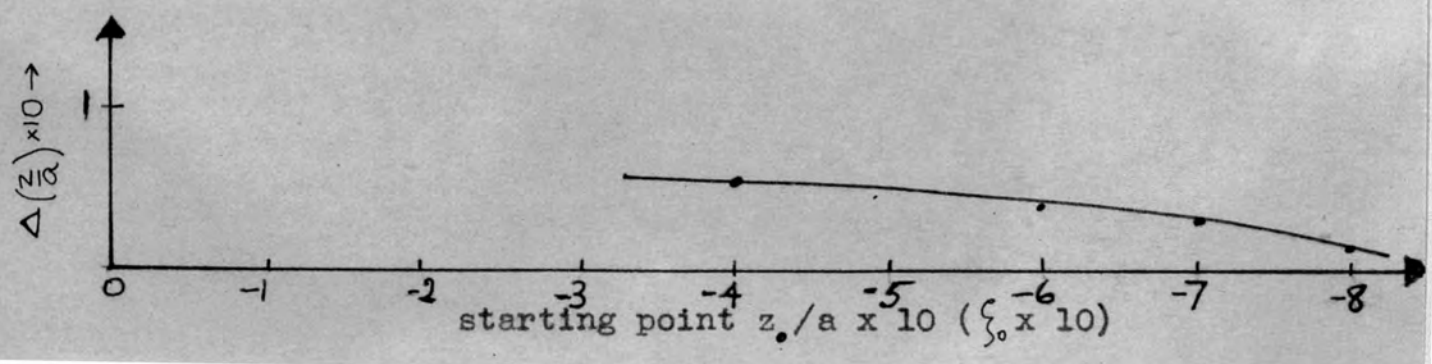
with

investigated range, and that the dispersion is greater in the z planes on the right of the mid plane, z positive, than on the left.

The change of the position of the primary caustic for sets of trajectories with different starting points and same momentum is shown in Fig. 19. The caustic rises as the starting point approaches the origin.

Another common feature of the trajectories is that the cusp of focus I_1 is always formed by rays with angles of emission between 75° and 85° ($\sim 80^o$). This was found experimentally for the spheroidal field spectrometer described by Braid and Richardson [4]. This is somewhat of a disadvantage because the self-absorption in the source may become significant for low energy electrons.

(iv)   Performance of a spheroidal field spectrometer.

The performance of a β-ray spectrometer is assessed from the resolving power and the corresponding transmission [36] or luminosity (source area x transmission) [25]. The resolution which is a measure of the accepted momentum band is determined from the line width. The line broadening is caused by three factors: 1) 'spherical aberration' arising from the use of a finite angular aperture, 2) use of a finite width of the slit, and 3) broadening due to the radius of the source disc [3, 12, 24].

Fig. 18 (a). Variation of the position of the focus I_1 with p^2.

(b). Variation of the position of I_1 with starting point at constant $p^2 = 45$.
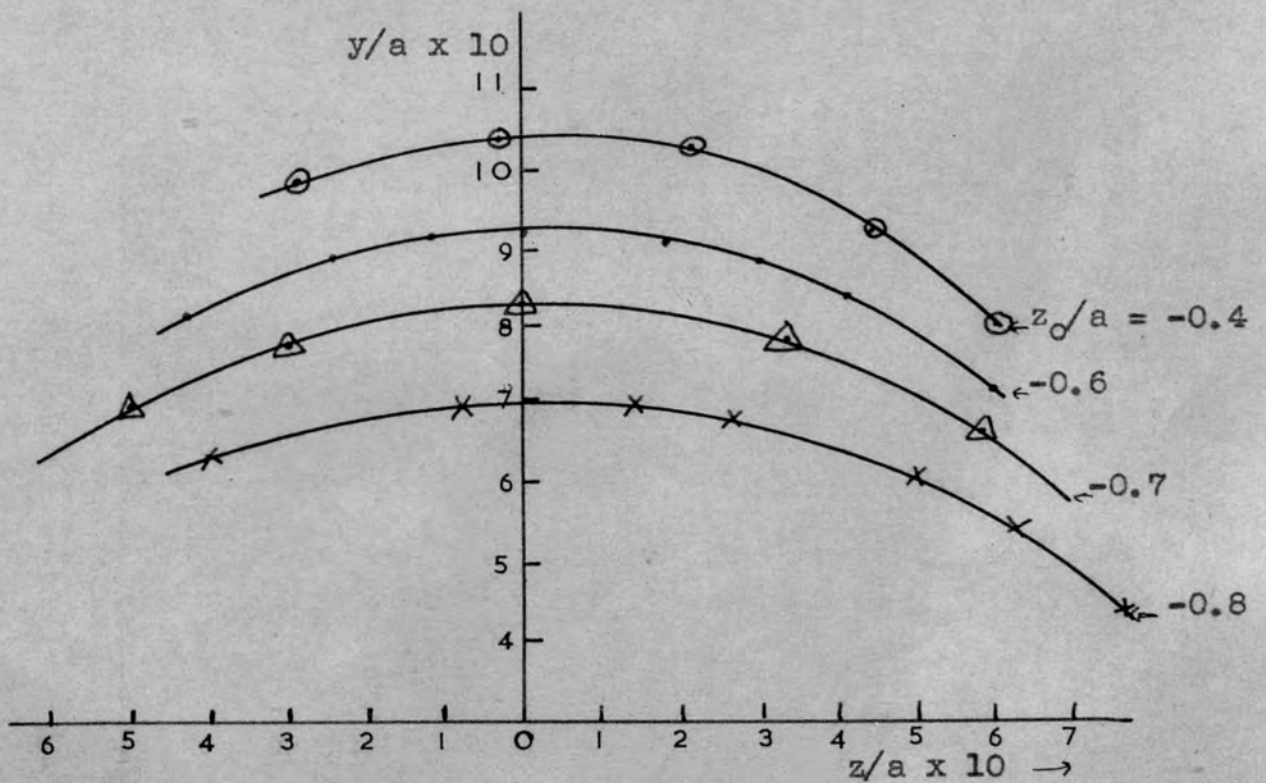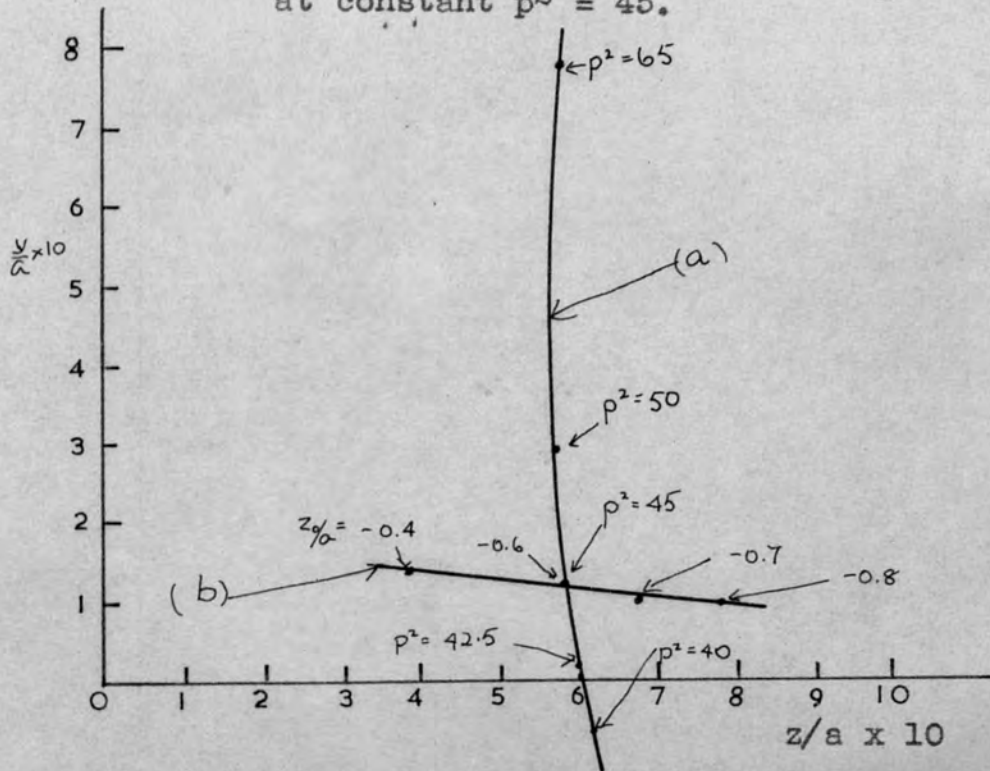
Fig. 19. Positions of the primary caustic for different starting points. p^2 is the same for all the curves. The values of z_0/a (ξ_0) of the starting point have been indicated.
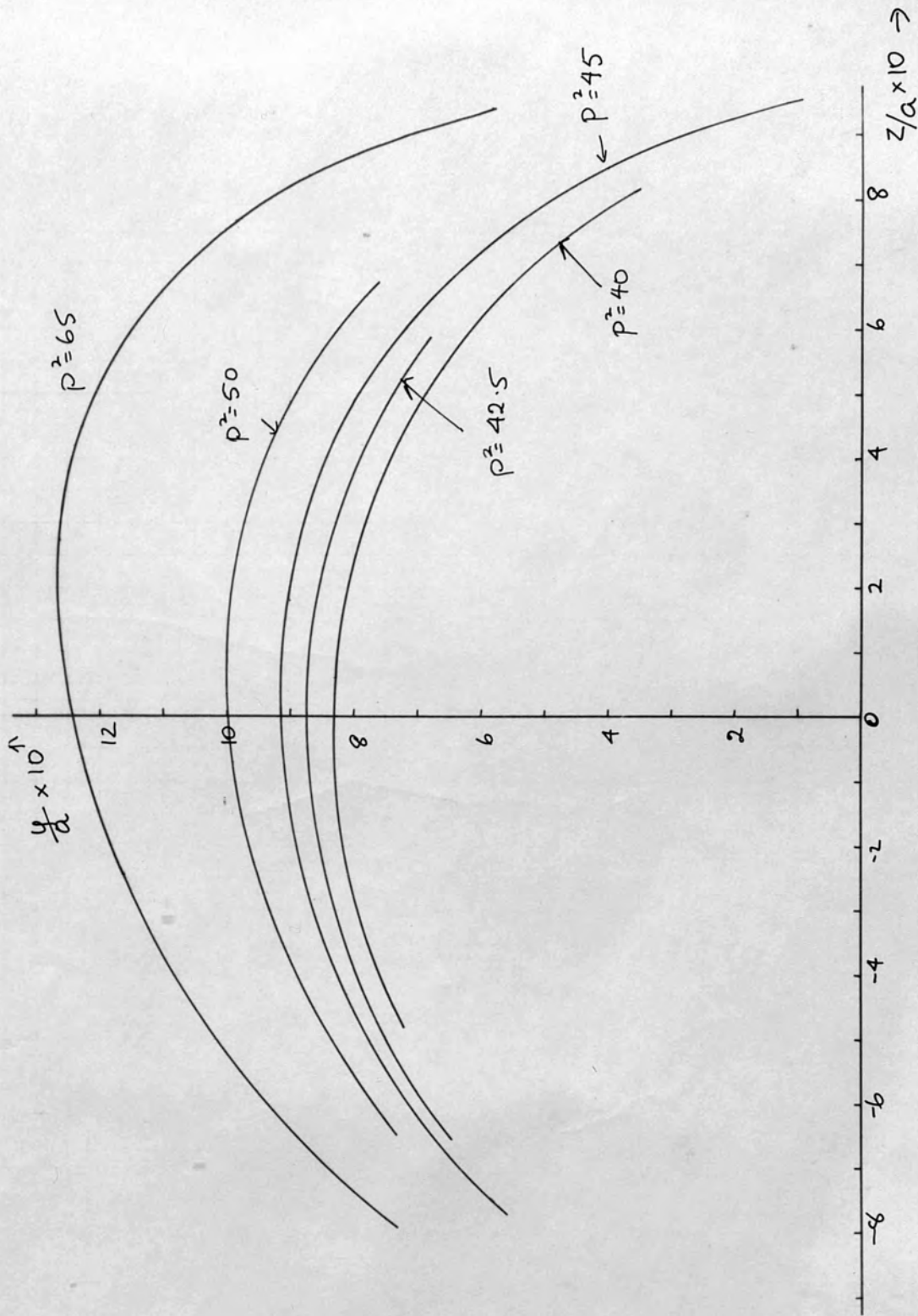
Fig. 20. Variation in the position of the primary caustic with p^2 for a particle starting at $z_0/a = -0.6$ ($\xi_0 = -0.6$). The curves are used to find the dispersion (see Fig. 21).
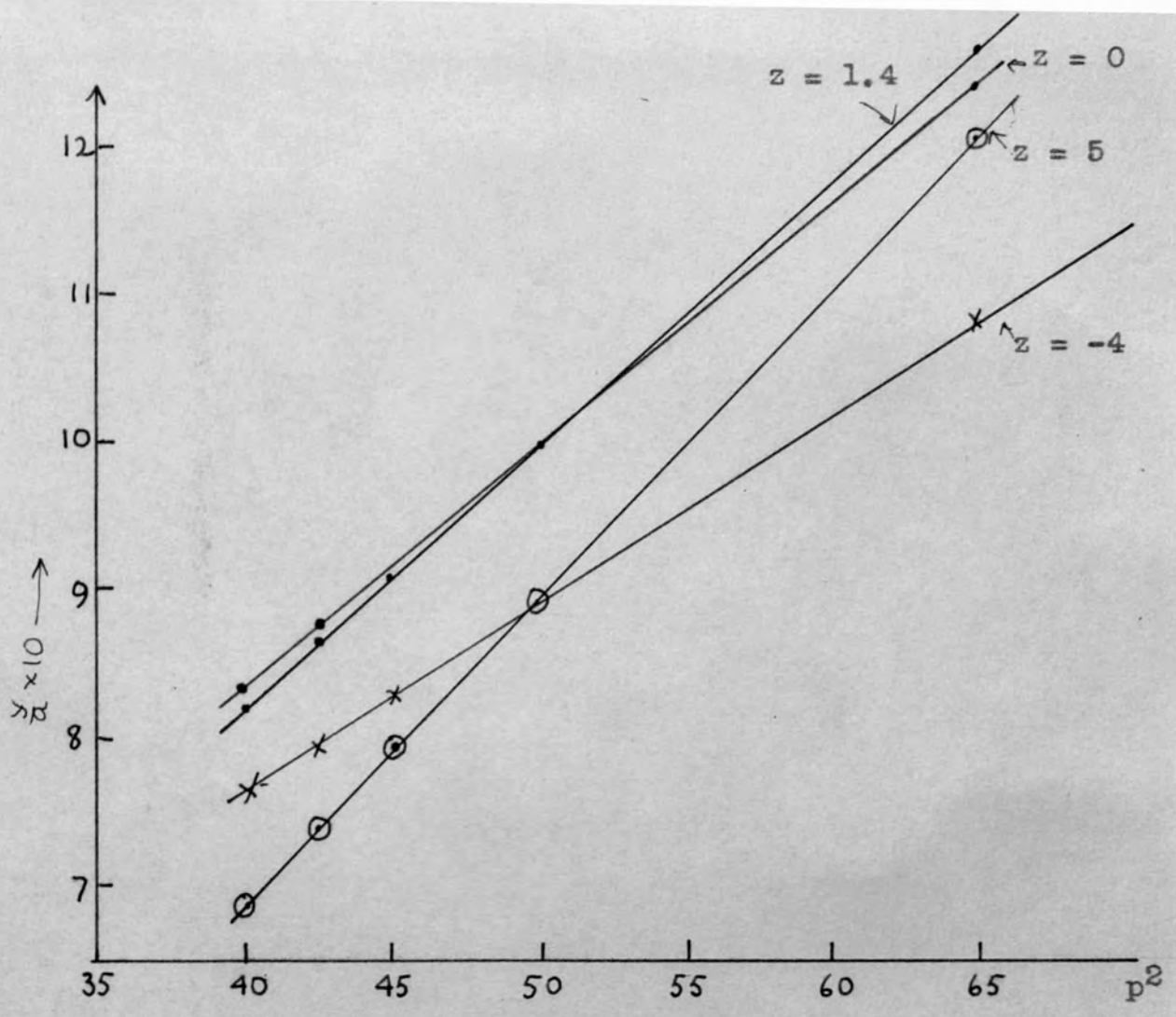
Fig. 21. Intersections of the caustics in Fig. 20 with different z planes plotted against p^2 ($z_0/a = -0.6$).
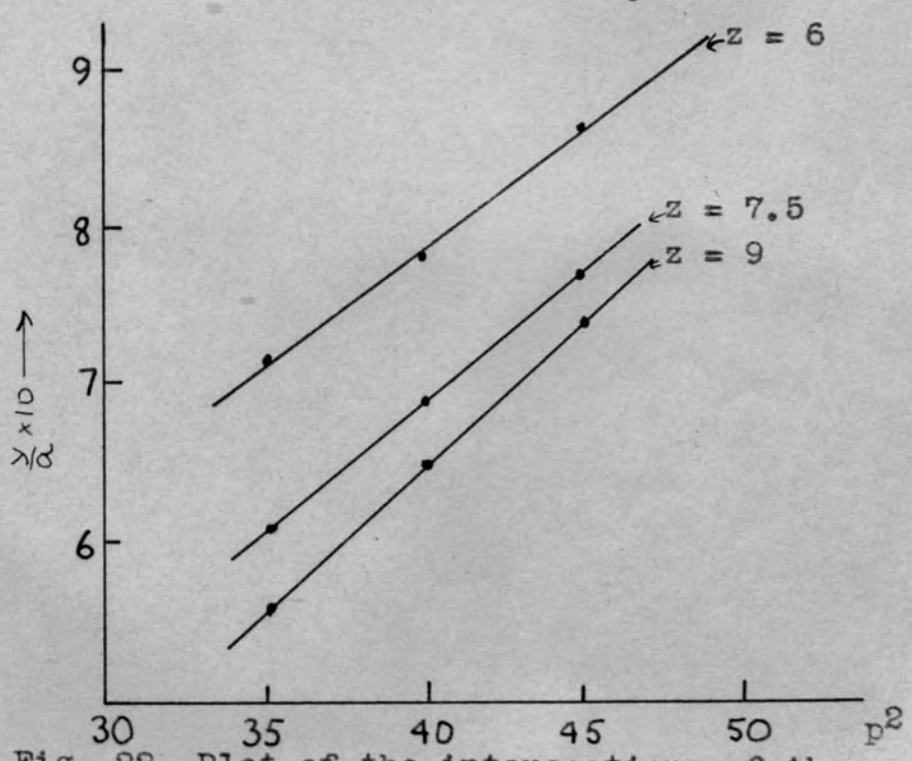
Fig. 22. Plot of the intersections of the caustics of Fig. 39 with different z planes against p^2 (combined field, $z_0/a = 0$).
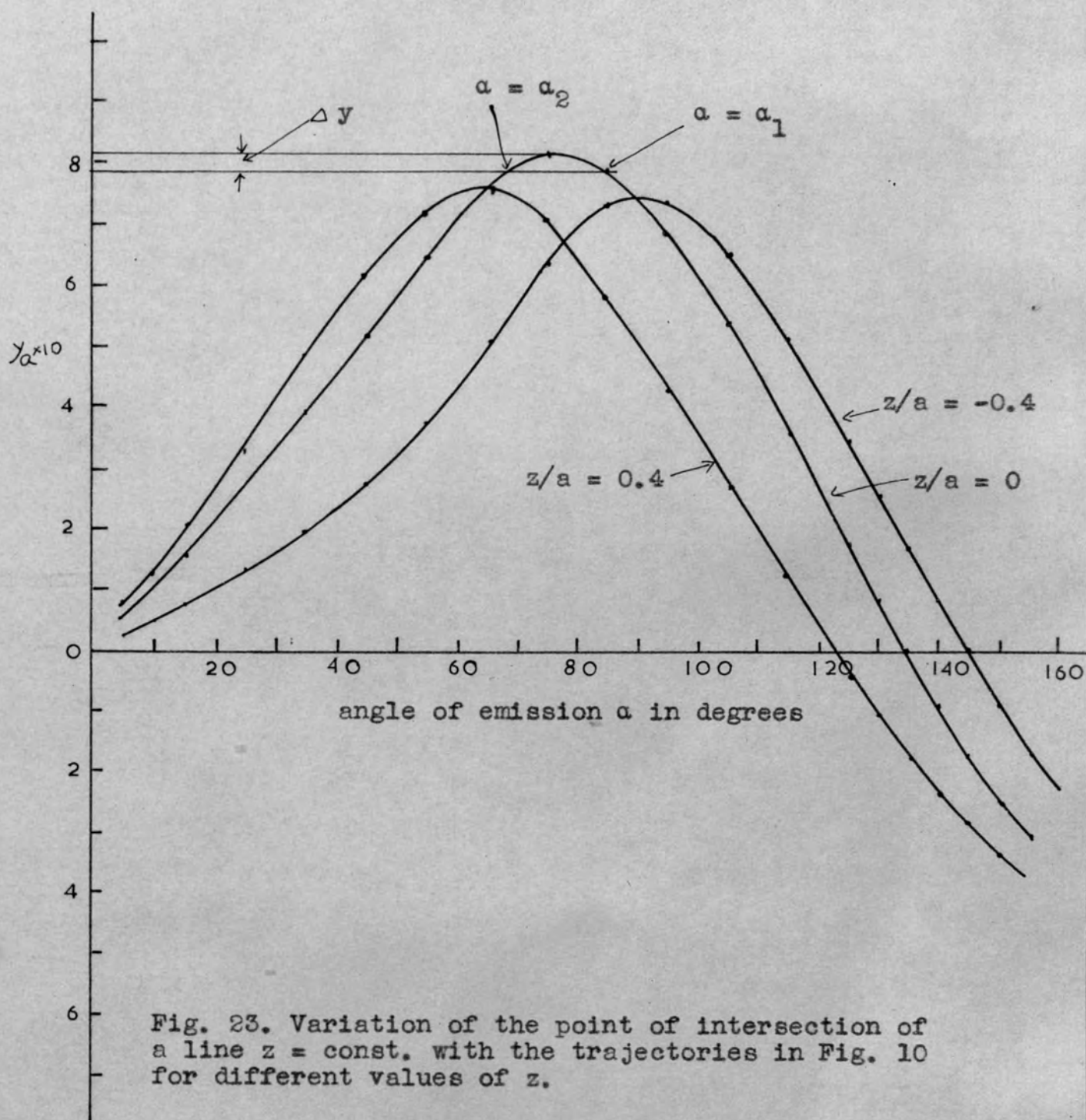
Fig. 23. Variation of the point of intersection of a line z = const. with the trajectories in Fig. 10 for different values of z.

In the spheroidal field the detector can be placed at a point such as P or I_1 (see, for example, Figs. 8 and 14). The spherical aberration as defined by Verster (1952) [36] was calculated as follows. The performance of a spectrometer with annular focusing according to Verster is described by

$$W = sT^2 + \frac{d}{D} \tag{28}$$

where d is the diameter of the source, W is the half width of the line, T is the transmission and s the spherical aberration parameter. For a point source, equation (28) becomes

$$W = sT^2 \tag{29}$$

W is defined by $\frac{\Delta p}{p}$ and $T = \frac{\Delta\Omega}{4\pi}$, where $\Delta\Omega$ is the solid angle accepted. The solid angle between two cones with a common apex and half angles α_1 and α_2 is $\Delta\Omega$ and is given by

$$\Delta\Omega = 2\pi \int_{\alpha_1}^{\alpha_2} \sin\alpha\, d\alpha = 2\pi\left(\cos\alpha_1 - \cos\alpha_2\right) \tag{30}$$

Δp will be proportional to the base width of the line $\Delta p'$ (say) and $\frac{\Delta p}{\Delta p'}$ will depend on the baffle arrangement used (Hubert 1952) [16]. Putting $\frac{\Delta p}{\Delta p'} = b$, then $W = b\frac{\Delta p'}{p}$ and equation (29) takes
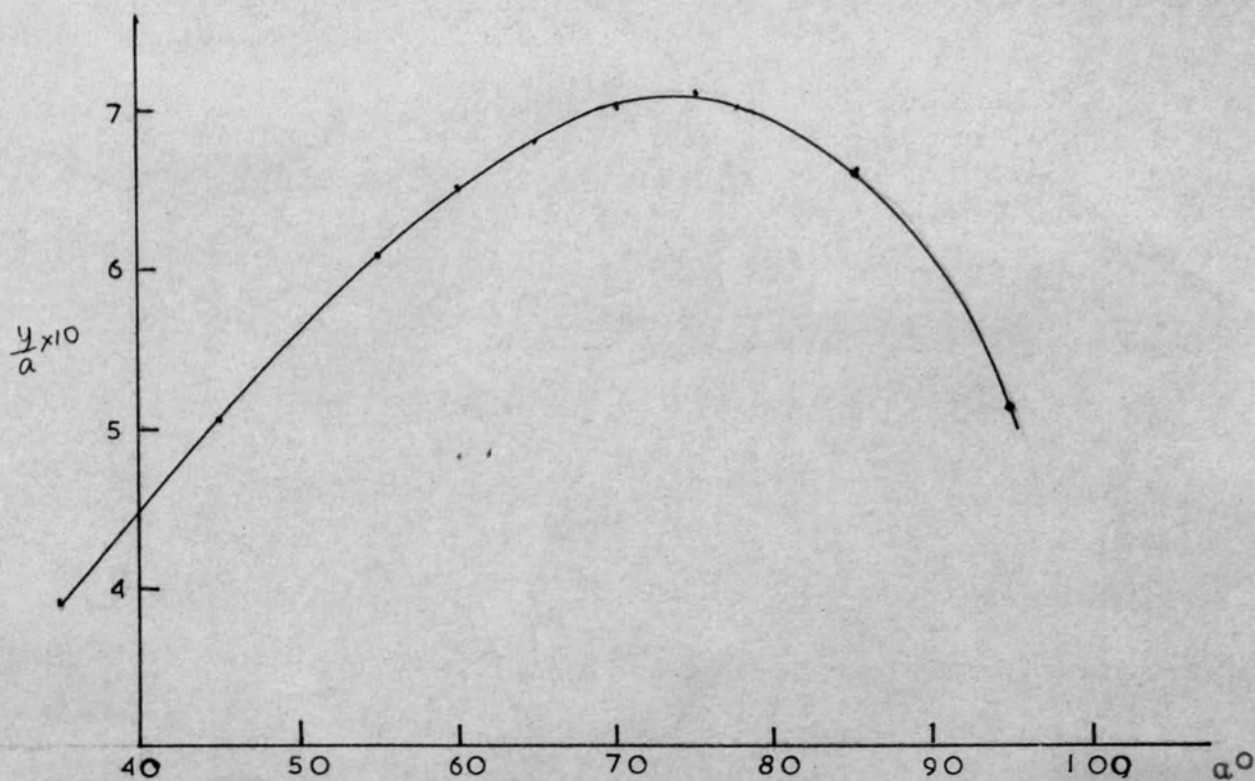
Fig. 24. Small portion of the peak of a curve such as Fig. 7. The initial conditions are different. $p^2 = 45$, $z_0/a = -0.8$.
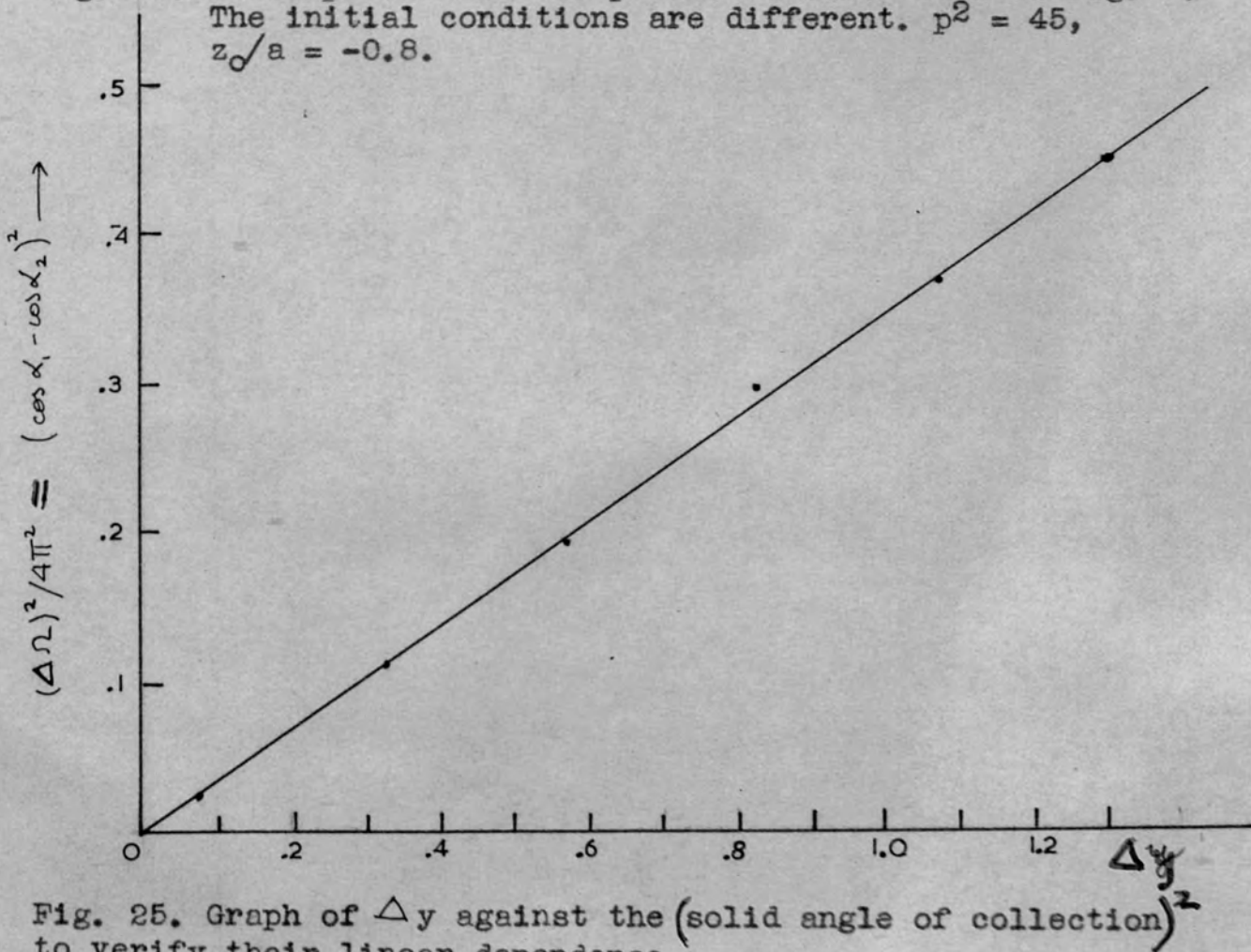
Fig. 25. Graph of $\triangle y$ against the (solid angle of collection)^2 to verify their linear dependence.

the following form

$$b \frac{\Delta p'}{P} = s \left(\frac{\Delta \Omega}{4\pi} \right)^2 \qquad (30a)$$

If the dispersion is defined by $D = \frac{P}{Y} \frac{\partial \lambda}{\partial p}$, where Y is

the y co-ordinate of the ring of the slit touching the primary

caustic and λ is a co-ordinate in the meridional plane in the

plane of the ring slit, such that the width of the slit is

$\Delta \lambda = \sqrt{\Delta z^2 + \Delta y^2}$, then one obtains

$$\frac{\Delta p'}{P} = \frac{1}{D} \frac{\Delta \lambda}{Y} \qquad (31)$$

and on substituting (31) into (30a) one obtains

$$S = 4b \frac{\Delta p'}{P} \frac{\Delta \lambda}{DY (\cos \alpha_1 - \cos \alpha_2)^2} \qquad (32)$$

The assumptions were verified graphically by plotting

the square of the solid angle or $(\cos \alpha_1 - \cos \alpha_2)^2$ against $\Delta . \lambda$,

the width of the slit. To find the solid angle accepted by a

certain slit, the plane of the slit is drawn in the meridional

plane as a line, and the intersection of the trajectories with

this line are found and plotted against α. Such curves are

shown in Fig. 23 for slits in three z planes. The maximum of

each curve corresponds to the co-ordinate of the primary caustic and to obtain the maximum solid angle of collection for a given slit width, one ring of the slit should be placed at a position corresponding to this peak. If the slit is Δ y wide, then the limiting values of α, α_1 and α_2 will be given by the values at the intersection of the curve with the horizontal line drawn Δ y below the first ring (maximum of the curve). The solid angle is then calculated from (30). A small portion of the peak used to verify the quadratic relation between Δ y (= $\Delta\lambda$ in this case) and $(\Delta\Omega)^2$ is shown in Fig. 24. The plot is shown in Fig. 25.

Table I shows the values of s' = s/4b calculated at different energies and slit positions for the foci I_1 and P. The resolution ε, and $\frac{\varepsilon}{T}$ are also tabulated for the corresponding conditions. ε is defined in the following way similar to that used by Lingen [19]

$$\varepsilon = \frac{\Delta\lambda}{P}\left(\frac{\partial p}{\partial\lambda}\right) \tag{33}$$

where $\frac{\partial p}{\partial\lambda}$ was evaluated in the plane of the slit. It can be seen that s' and ε/T are smaller for the focus I_1 than for P, and increase in s' implies an increase in ε/T. They also decrease as the starting point moves away from the mid plane, thus the focusing is better for a particle starting at $\xi_0 = -0.8$

$\frac{z_0-\xi_0}{a}$	p^2	Type of focus	$\alpha_1 - \alpha_2$ °	coordinates of slit at caustic		at inner edge		width of slit $\Delta\lambda$	Dispersion D	Coordinates of focus		T. % of 4π	S'	resolution ε %	$\frac{\varepsilon}{T}$
				z	Y	z	y			y_f	z_f				
-0.6	50	P	55-65	5.76	8.40	5.64	8.26	.18	2.02	0.26	5.20	7.5	.48	1.1 %	.14
-0.6	42.5	I_1	75-85	-0.4	8.76	-0.4	8.56	.20	1.55	0.2	5.96	8.5	.50	1.47	.17
-0.6	45	P	55-65	5.16	7.84	5.04	7.64	.23₃	1.97	0.0	5.8	7.5	.68	1.53	.20
-0.6	45	I_1	75-85	0.1	9.14	0.1	8.96	.18	1.61	1.20	5.76	8.5	.42	1.2	.14
-0.6	65	P	45-55	8.32	8.80	7.44	8.34	.99	2.07	-0.4	1.20	6.6	3.25	2.6	.40
-0.4	50	I_1	75-85	1.40	11.20	1.40	10.7	.45	1.66	3.25	3.70	8.5	.85	2.4	.28
-0.4	50	P	55-65	5.70	9.35	5.30	8.75	.72	1.82	-0.50	2.75	7.5	1.98	3.5	.47
-0.4	40	I_1	75-85	0.48	9.52	0.48	9.08	.34	1.55	-0.48	4.08	8.5	.82	2.3	.27
-0.8	45	I_1	75-85	-2.52	6.80	-2.52	6.68	.12	1.48	0.52	7.84	8.5	.41	1.2	.14
-0.8	50	I_1	75-85	-1.40	7.60	-1.40	7.50	.10	1.63	2.0	7.60	8.5	.28	.81	.09
-0.8	55	I_1	75-85	-0.5	8.4	-0.5	8.28	.10	1.73	3.28	7.54	8.5	.24	.69	.08
0	35	I_1	25-30	10.1	2.70	9.85	2.65	.20	1.16	0.1	7.4	2.0	41.6	6.3	3.2
0	35	I_1	25-35	9.90	3.05	9.45	2.80	.51	1.49	0.1	7.4	4.5	16.8₃	11.2	2.5
0	45	I_1	35-45	9.92	5.16	9.20	4.68	.86	1.57	1.5	7.0	5.6	9.4	10.6	1.9
0	45	P	45-55	8.70	6.72	8.12	6.20	.78	1.54	0	6.0	6.6	4.5	7.4	1.11

Table 1 Table of parameters indicating the focusing properties of the spheroidal and combined fields. The range of ε/T for the spectrometer described in ref[13] varied from 1.0 to .58 and in ref [4] it is 1.1 if it is assumed that the width at half height is half the width of the base.

than for that at ζ_o = -0.6 or -0.4. It also appears that s'
is smaller at the higher energies if other conditions are the
same.

III

Case of a particle starting on a ring.

(i)   Introduction.

In order to investigate the aberrations and line
broadening produced by the finite area, it is necessary to
know the trajectories of a particle which starts on a ring.
In the present work trajectories for particles starting on
a large ring were computed to investigate the possibility
of using large sources and also so that the properties could
be seen more clearly.

(ii)   Initial conditions.

For a particle starting on a ring the constant C is
not usually zero and the general equations (4), (5) and (6)
represent the motion. If v is the velocity, α the angle of
projection in the meridional plane and γ the angle between
the velocity and the meridional plane, the relations between
the position of the velocity vector and α and γ are shown in
Figs. 26 and 27. $v \cos \gamma$ is the component of velocity in the
meridional plane and $v \sin \gamma$ the component in the equatorial
plane.

When the velocity vector lies in the plane ABCD (Fig. 26),
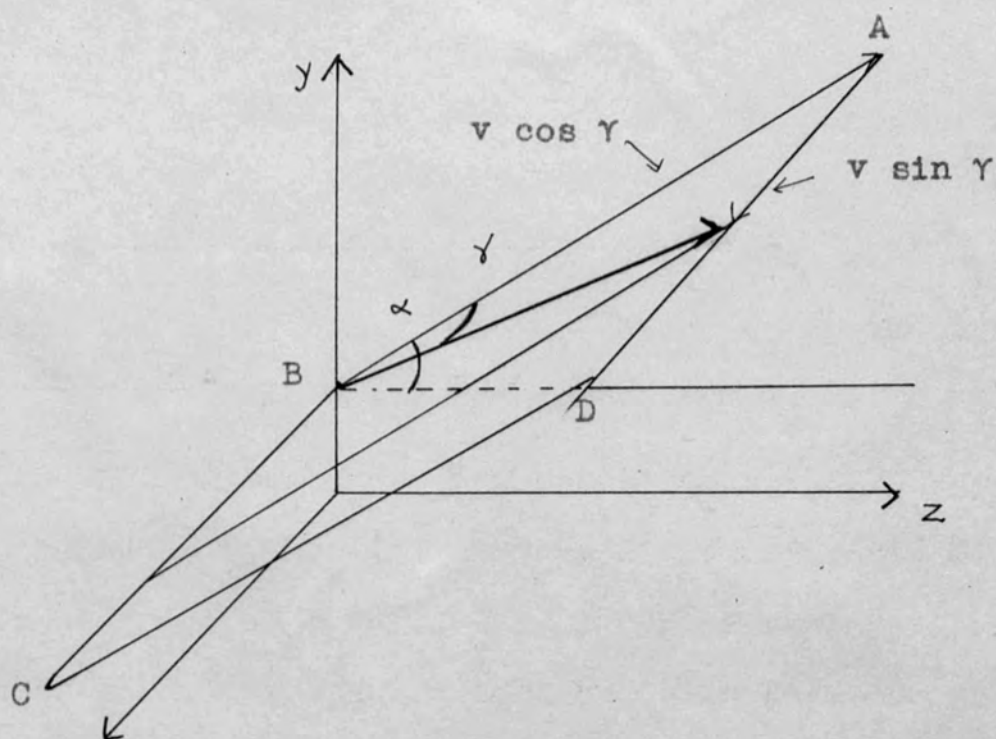
Fig. 26. Diagram showing the relation between α and γ if the velocity vector lies in the plane ABCD.
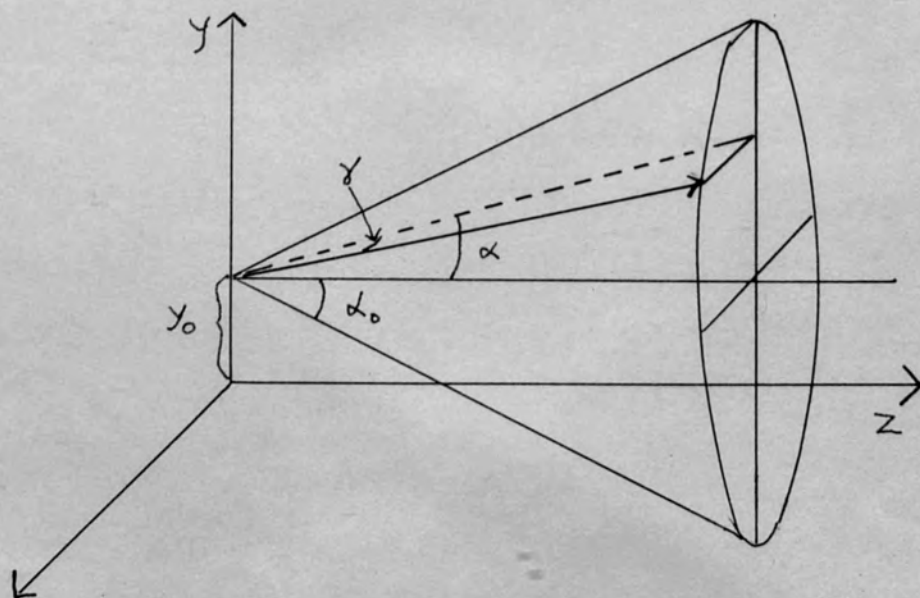
Fig. 27. Diagram showing the relation between α and γ if the velocity vector lies on a cone with half angle α_0.

a is constant and γ varies from 0 to 2π. In the case, more useful in β-spectrometry, in which particles are emitted into a cone such that the velocity vectors lie on cones with a common apex, the relation between a, γ and a_o, where a_o is the half angle of any chosen cone, is given by

$$\cos \gamma \cos a = \cos a_o, \tag{34}$$

where $0 \le \gamma \le a_o$, $0 \le a \le a_o$.

If the particle starts with no component of velocity in the equatorial plane, i.e. $(y\dot{\phi}) = 0$ at $y = y_o$ and $z = z_o$ $(\eta = \eta_o)$, where z_o and y_o are the co-ordinates at the starting point, it follows from eq. (6) that

$$C = C_o = eA_o y_o \tag{35}$$

A_o, the vector potential at $(y_o z_o)$, is given by

$$A = \frac{a^2 H_0 (\eta_o - 1)}{y_o}$$

If, however, the initial velocity of the particle is at an angle γ to the meridional plane

$$(y_o \dot{\phi}_o) = v \sin \gamma \quad \text{and}$$

$$m y_o v \sin \gamma = C - e A_o y_o \tag{36}$$
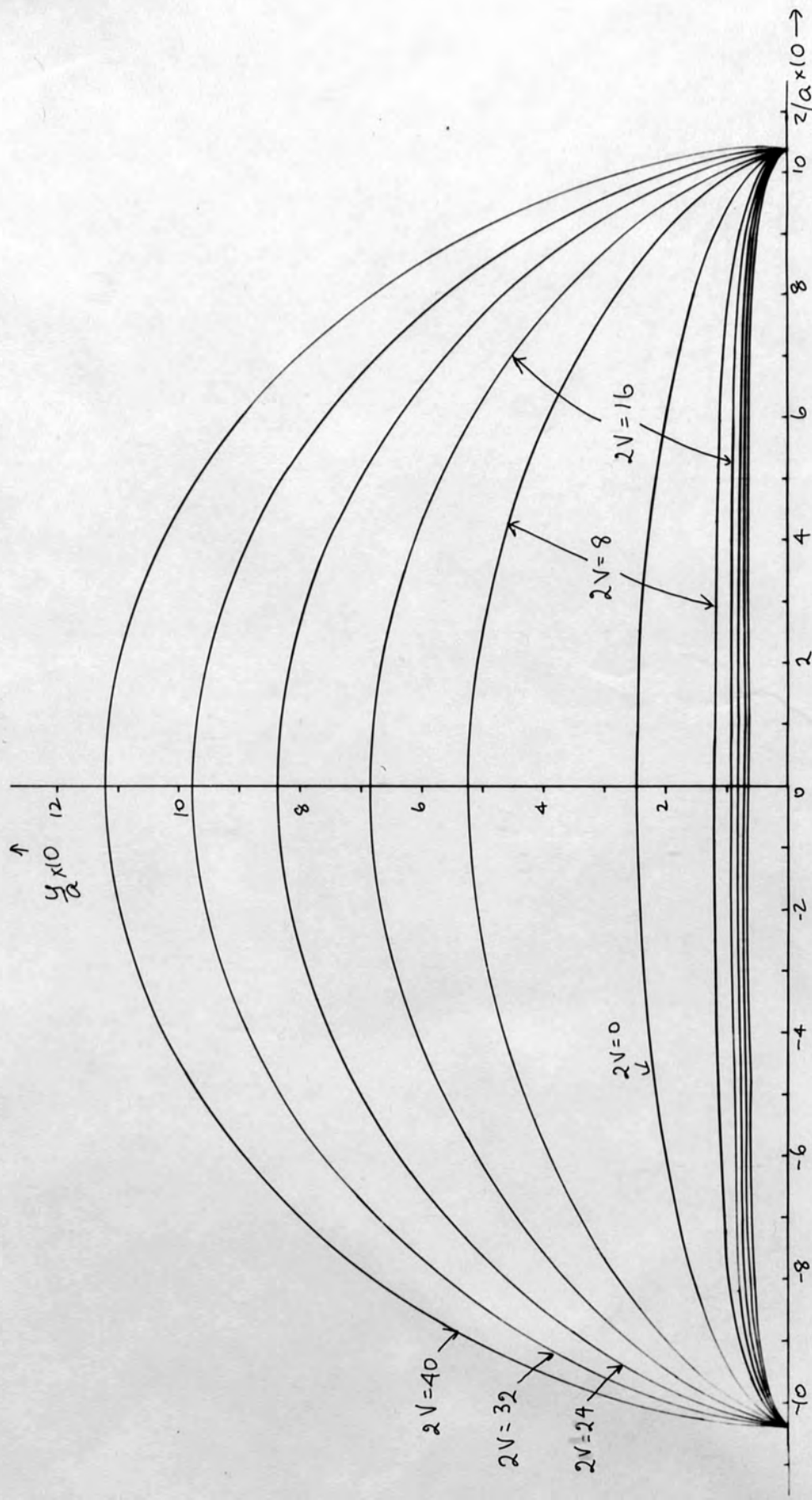
Fig. 28. Equipotentials V for a particle starting on a ring with the following initial conditions: $y_o/a = 0.2$, $z_o/a = -0.6$, $p^2 = 45$ and $\gamma = 0$.
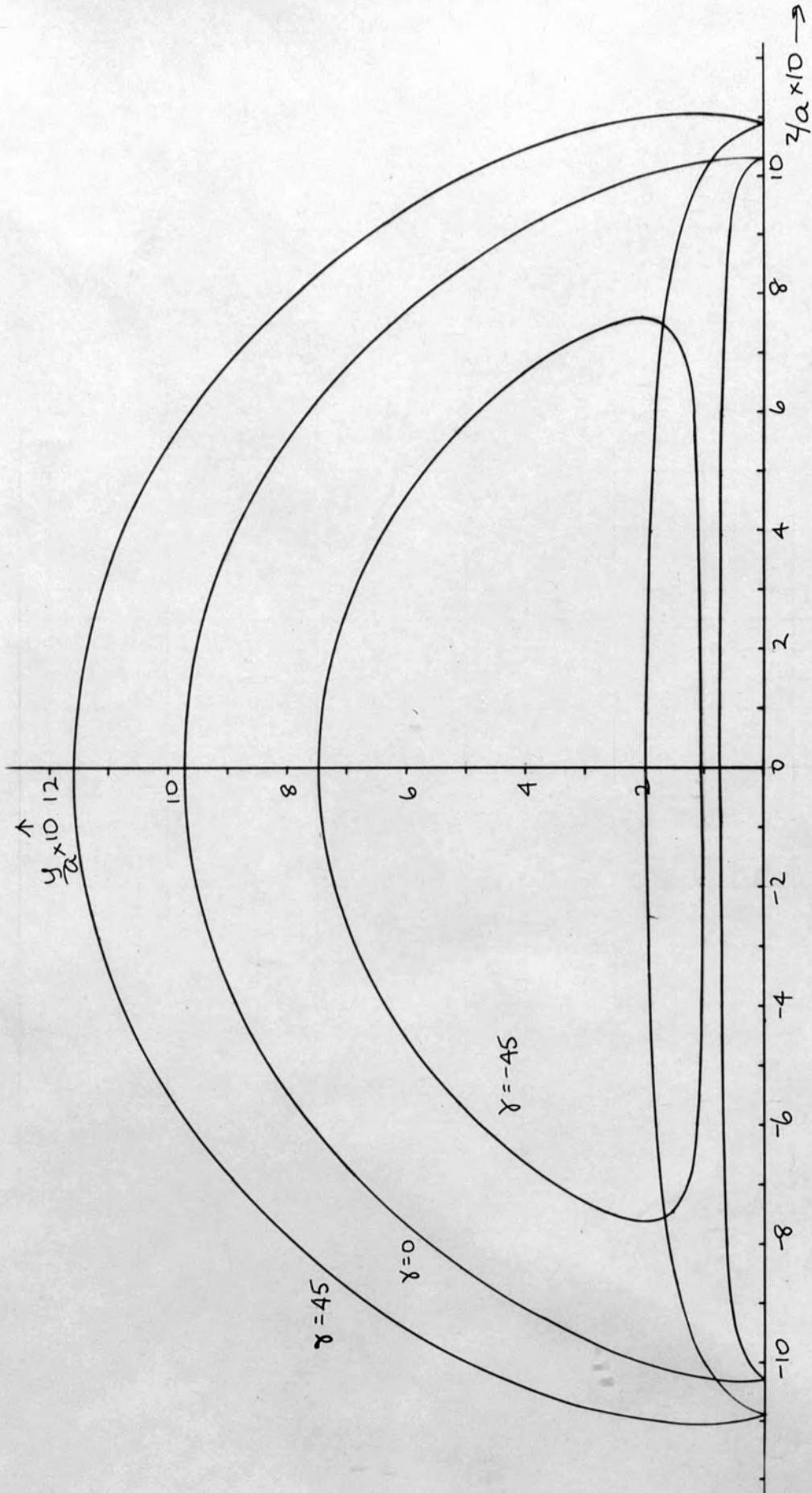
Fig. 29. Equipotentials V for three values of γ = 0°, 45°, -45°. The other conditions are the same as in Fig. 28. 2V for this set is equal to 32.

131

The value of C in general is given by

$$C = e A_0 y_0 + m v y_0 \sin \gamma \qquad (37)$$

where $0 \le \gamma \le 2\pi \qquad y_0 \ge 0$

On substituting for A, one obtains

$$C = e a^2 H_0 \left[(\eta_0 - 1) + \frac{m v y_0 \sin \gamma}{e a^2 H_0} \right] \qquad (38)$$

If we put

$$C = e a^2 H_0 K = e a^2 H_0 k (\eta_0 - 1) \qquad (39)$$

then $\quad K = (\eta_0 - 1) + \dfrac{m v y_0 \sin \gamma}{e a^2 H_0} \quad$ and $\quad k = \dfrac{K}{\eta_0 - 1} \qquad (40)$

It is more convenient to use k in the equations and K for computation because in the latter $\eta_0 - 1$ appears in the numerator only. From (40) it can be seen that k = 1 if γ = 0, i.e. if the particle starts with a velocity in the meridional plane. k may be positive or negative, depending on sin γ, and may be zero even if $\eta_0 \neq 1$. This corresponds to the values of the parameters that a particle, which had started on the axis, would have at the co-ordinate η_0.
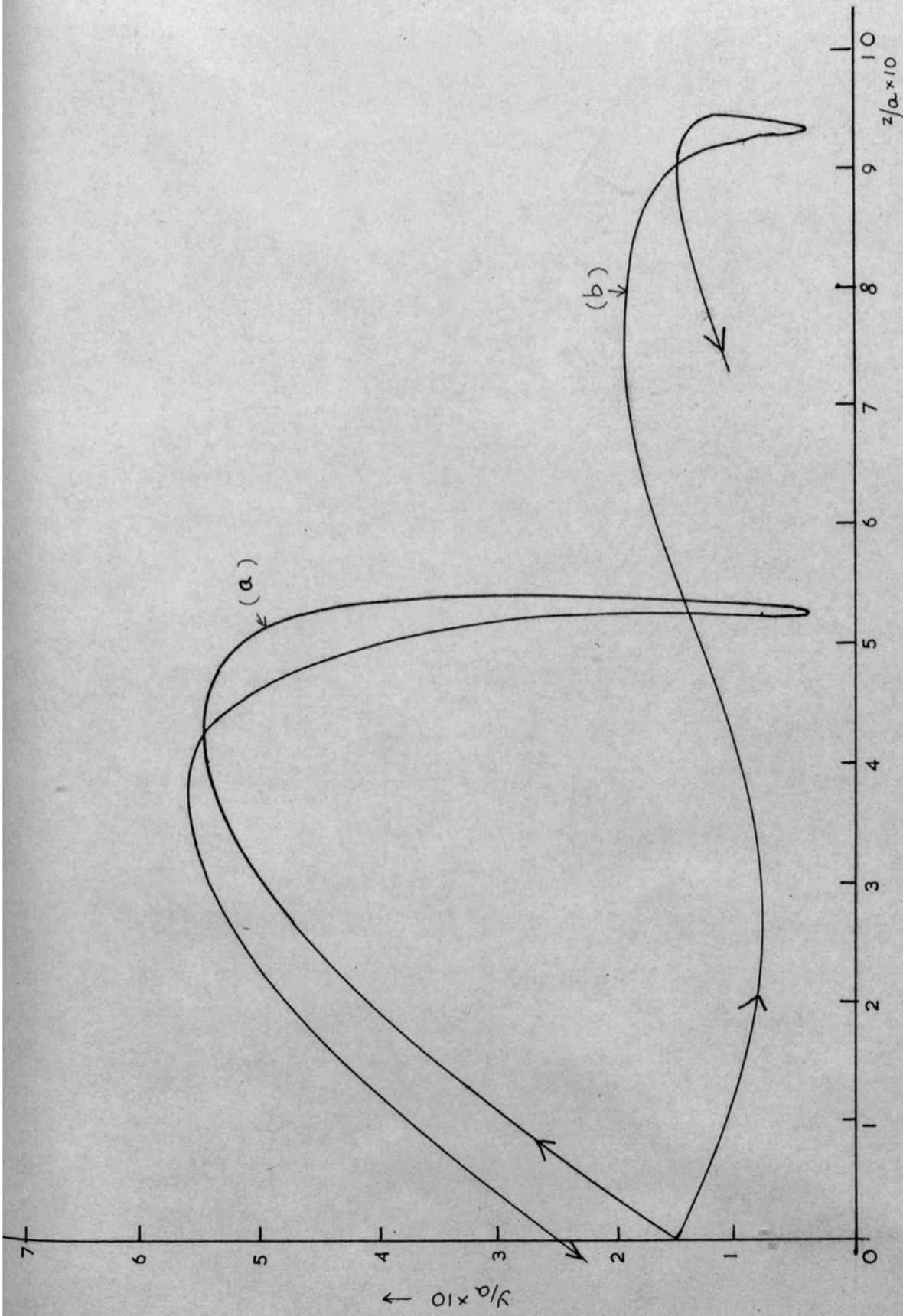
Fig. 30. Two trajectories for a particle starting in the mid plane. $y_0/a = 0.15$ and $p^2 = 20$. For (a), $\alpha = 20°$ and for (b) $\alpha = -20°$

132

(iii)   The equipotentials.

The function V takes the following form when the value
of C is substituted into the equation (14)

$$V = \frac{(e\,a^2 H_0)^2}{2m}\left[\frac{k(\eta_0-1)-(\eta-1)}{y}\right]^2 \qquad (41)$$

The shape of the equipotentials for various initial
conditions is shown in Figs. 28 and 29. Fig. 28 is a set of
equipotentials for one starting point with $\Upsilon = 0$. The equi-
potential 0 passes through the initial co-ordinates. In Fig. 29 the
equipotential with V = 16 (2V = 32) is plotted for three values
of Υ, $\Upsilon = 0$, $\Upsilon = 45°$, $\Upsilon = -45°$. The equipotential for $\Upsilon = 0$
also appears in Fig. 28. It can be seen that the effect of Υ,
if $\Upsilon > 0$, is the same as that of increasing C by increasing
η_0. The forms of the equipotential confirm the predictions
made in Chapter I. No solution for η can be found for V = 0
if C is negative.

(iv)   The equations of motion.

The equations of motion, which were found by substituting
the value of C given in equation (39) into (4), (5) and (6),
are given by

$$\ddot{y} = \left(\frac{e a^2 H_0}{m}\right)^2\left\{\frac{k(\eta_0-1)-(\eta-1)}{y}\right\}\left\{\frac{k(\eta_0-1)-(\eta-1)}{y^2}+\frac{1}{2a}\left(\frac{1}{r_1}+\frac{1}{r_2}\right)\right\} \qquad (42)$$

$$\ddot{z} = \left(\frac{ea^2H_0}{m}\right)^2 \left\{ \frac{k(\eta_0-1)-(\eta-1)}{2ay^2} \right\} \left\{ \frac{a+z}{r_1} - \frac{a-z}{r_2} \right\} \qquad (43)$$

$$\dot{\phi} = \left(\frac{ea^2H_0}{m}\right) \left\{ \frac{k(\eta_0-1)-(\eta-1)}{y^2} \right\} \qquad (44)$$

A programme similar to that used for the axial case was used. In this case there is a sharp turning point as the minimum value of y is approached, and therefore the step length had to be considerably reduced at this turning point. Two typical trajectories are shown in Fig. 30. For both (a) and (b) the initial velocity is in the meridional plane and is the same in both cases. For (a) $\alpha = 20^\circ$ and for (b) $\alpha = -20^\circ$. The radius of curvature of (a) at its lowest point is very small.

The energy was checked at each step of the integration and if the check failed the next set of data was read in. This programme was more general because it could also be used for the axial point source if the integration was stopped after the particle crossed the axis once, i.e. i = 0.

(v)   <u>Some properties of trajectories for a particle starting on a ring.</u>

A typical set of trajectories for which $Y = 0$ is shown in Fig. 31. For this set $p^2 = 55$. For lower energies, for
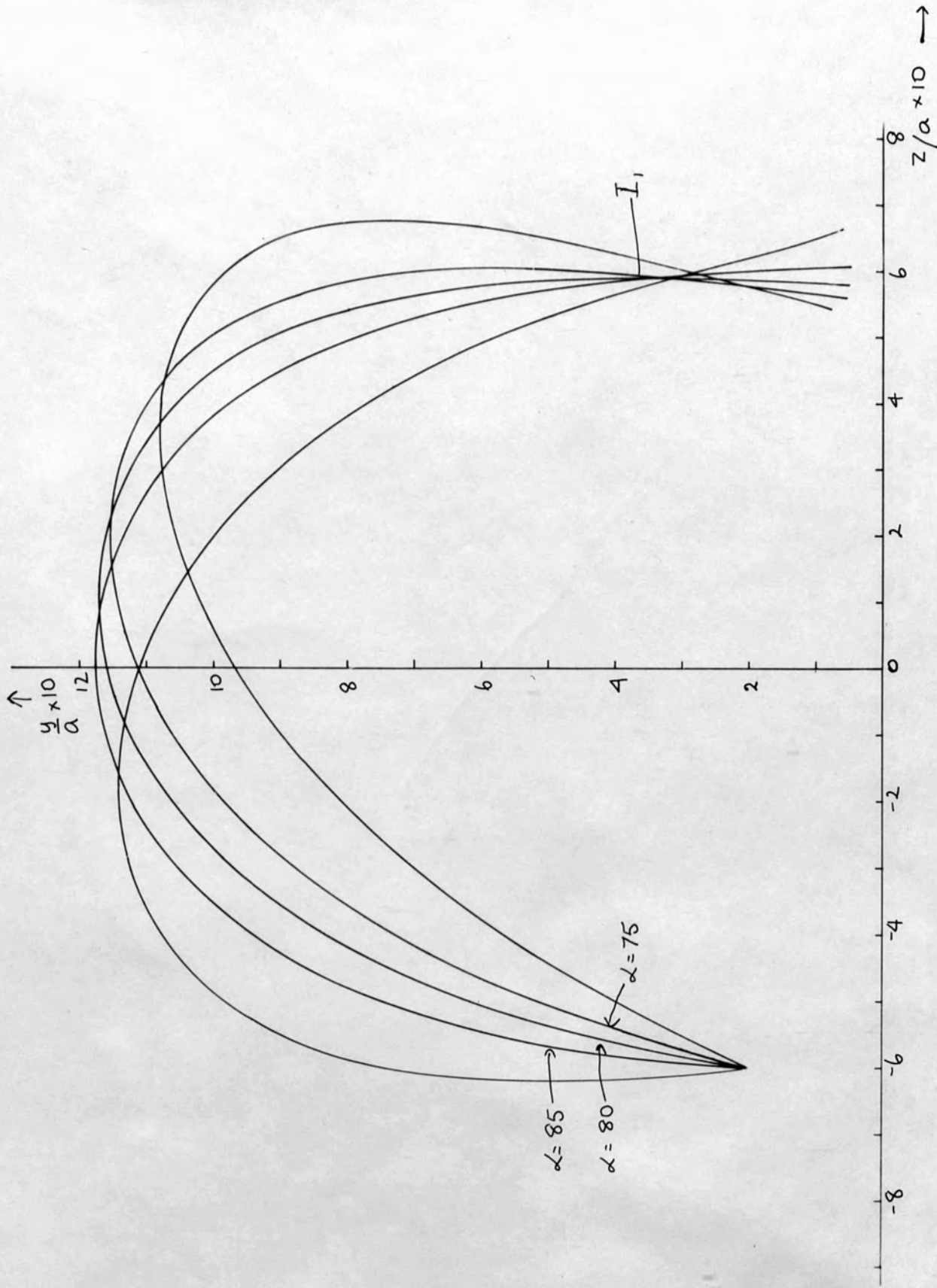
Fig. 31. Trajectories for a particle starting on a ring with the initial velocity in the meridional plane ($z_0/a = -0.6$, $y_0/a = 0.2$, $p^2 = 55$, $\gamma = 0$).
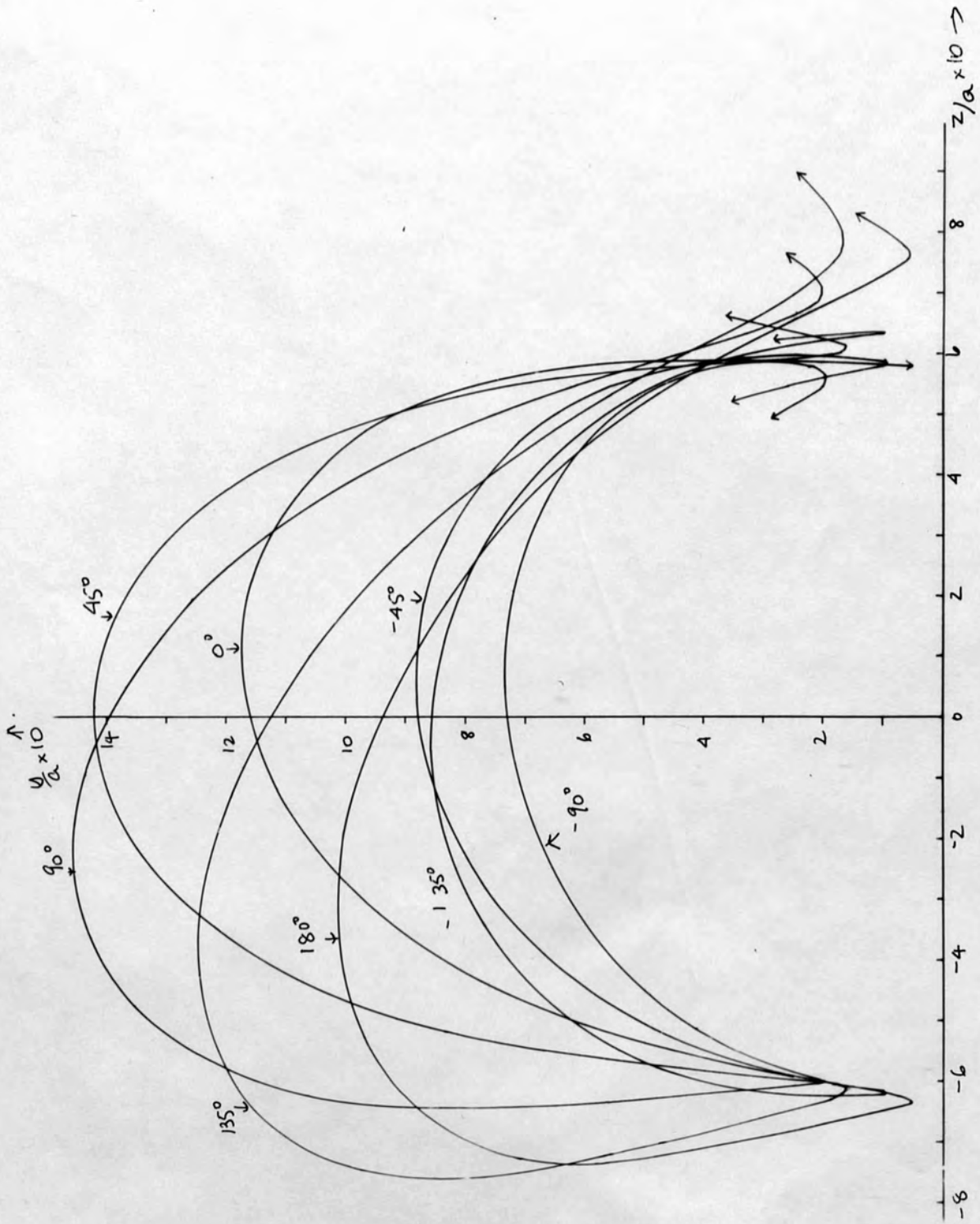
Fig.32. Trajectories for a particle with $p^2=55$ for various values of γ ($\swarrow=80$) The initial coordinates are the same as in Fig.33 but the initial velocity lies in a plane.
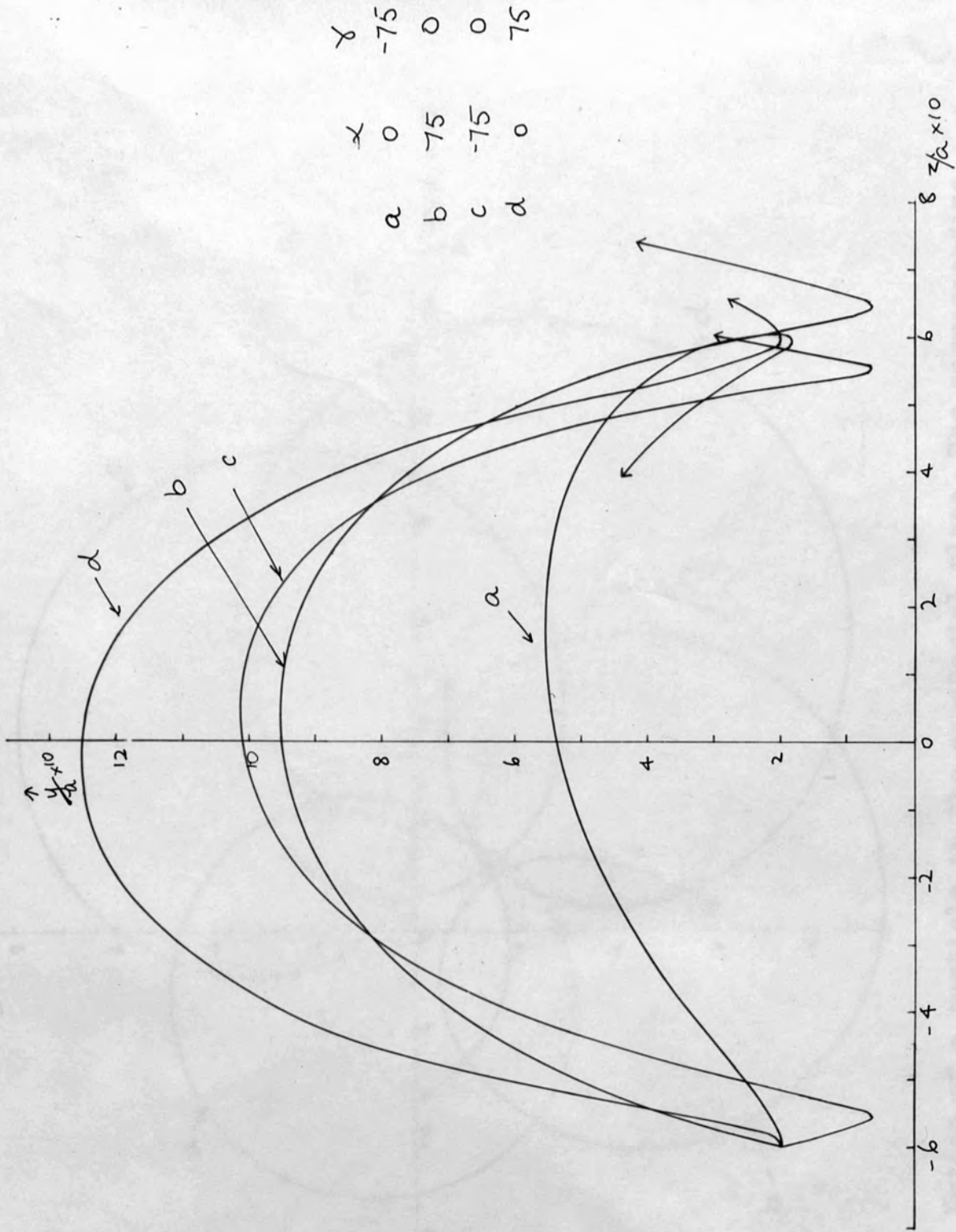
Fig. 33. Trajectories in the meridional plane for a particle for which the initial velocity lies on a cone(Fig.27) $p^2=55$, $y_0/a =0.2$, and $z_0/a = -0.6$.
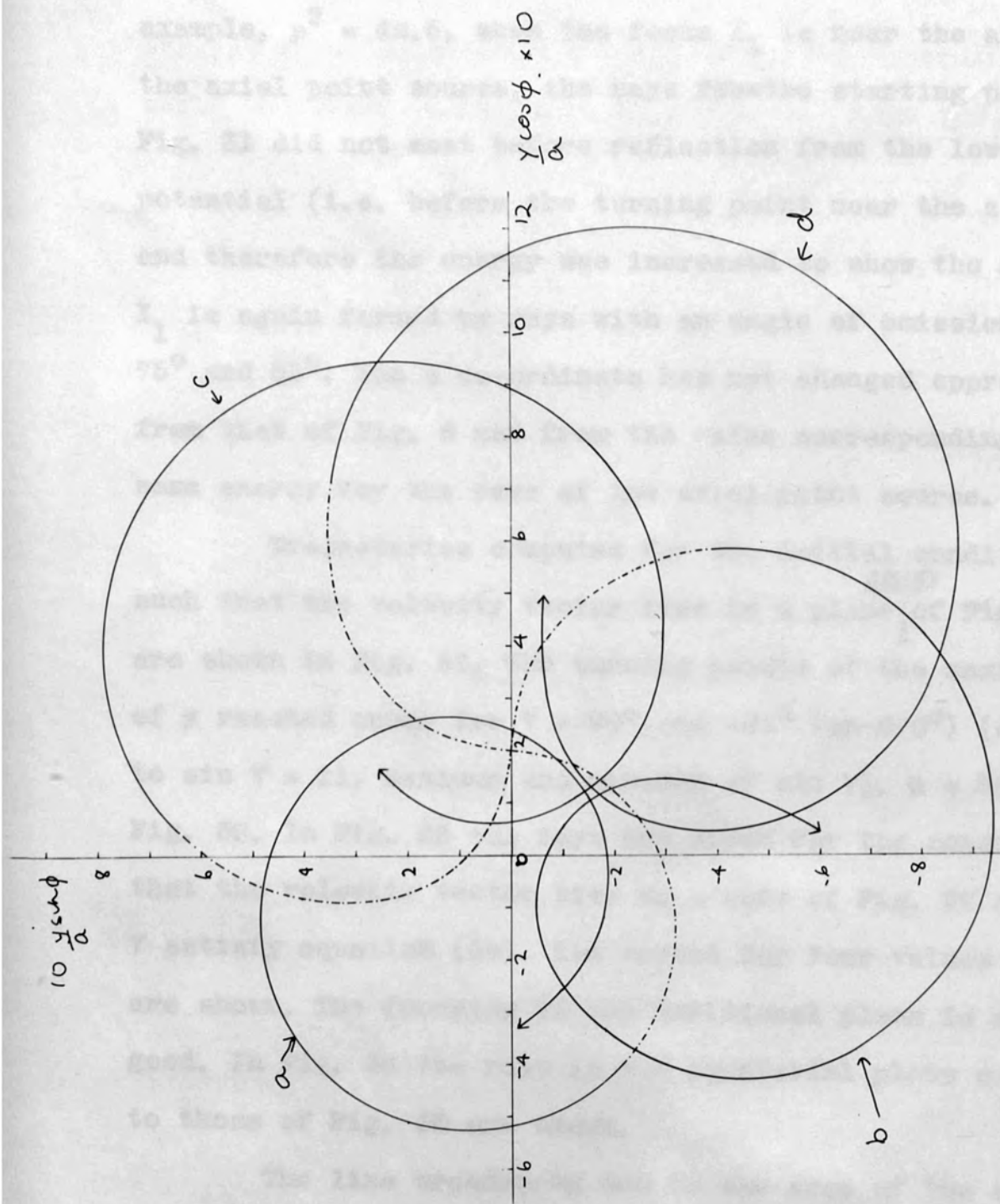
Fig. 34. Motion of a particle in the equatorial plane. The corresponding trajectories in the meridional plane are shown in Fig. 33.

example, $p^2 = 42.5$, when the focus I_1 is near the axis for
the axial point source, the rays from the starting point of
Fig. 31 did not meet before reflection from the lower equi-
potential (i.e. before the turning point near the z axis)
and therefore the energy was increased to show the focus.
I_1 is again formed by rays with an angle of emission between
75° and 85°. The z co-ordinate has not changed appreciably
from that of Fig. 6 and from the value corresponding to the
same energy for the case of the axial point source.

Trajectories computed for the initial conditions
such that the velocity vector lies in a plane ABCD of Fig. 26
are shown in Fig. 32. The turning points of the maximum value
of y reached occur for $\Upsilon = 90^\circ$ and -90° (or 270°) (corresponding
to $\sin \Upsilon = \pm 1$, maximum and minimum of $\sin \Upsilon$). $\alpha = 80^\circ$ in
Fig. 32. In Fig. 33 the rays are shown for the condition
that the velocity vector lies on a cone of Fig. 27 and α,
Υ satisfy equation (34). The curves for four values of Υ
are shown. The focusing in the meridional plane is not very
good. In Fig. 34 the rays in the equatorial plane corresponding
to those of Fig. 33 are shown.

The line broadening due to the size of the source
disc could be evaluated for a particular arrangement of selecting
slits [3] if more trajectories were computed for smaller discs.

From the trajectories it can be seen that particles
are trapped in the field, and those starting on a ring are

trapped in a 'belt' around the z axis. The spheroidal field
would therefore be suitable as a magnetic trap [29].

IV

Spectrometry using combined spheroidal and uniform fields.

(i)   Introduction.

In the large spheroidal field spectrometer described
in reference 13 the rays forming the focus were projected at
$\sim 45^{\circ}$. The shape of the trajectories found experimentally is
shown in Figs. 2 and 3 of reference 13. The right hand end
plate (24 in Fig. 3 of part I) is a magnetic equipotential
surface, therefore the source must be somewhere in the vicinity
of the mid plane of the spheroidal field. Some trajectories
with an axial source near the mid plane have been plotted in
Fig. 12. For this energy the focus I_1 is below the axis and
as in the case of rays for other starting points shown (Figs. 5,
7, 8, 10) the rays with angles of projection at about $\sim 45^{\circ}$
are nearly parallel and do not form a sharp focus. It was
therefore concluded that the field in the spectrometer is
not truly spheroidal.

In an attempt to find the theoretical field in the
spectrometer, a uniform field has been superposed on the
spheroidal field. The focusing of the rays for an axial point
source were investigated.
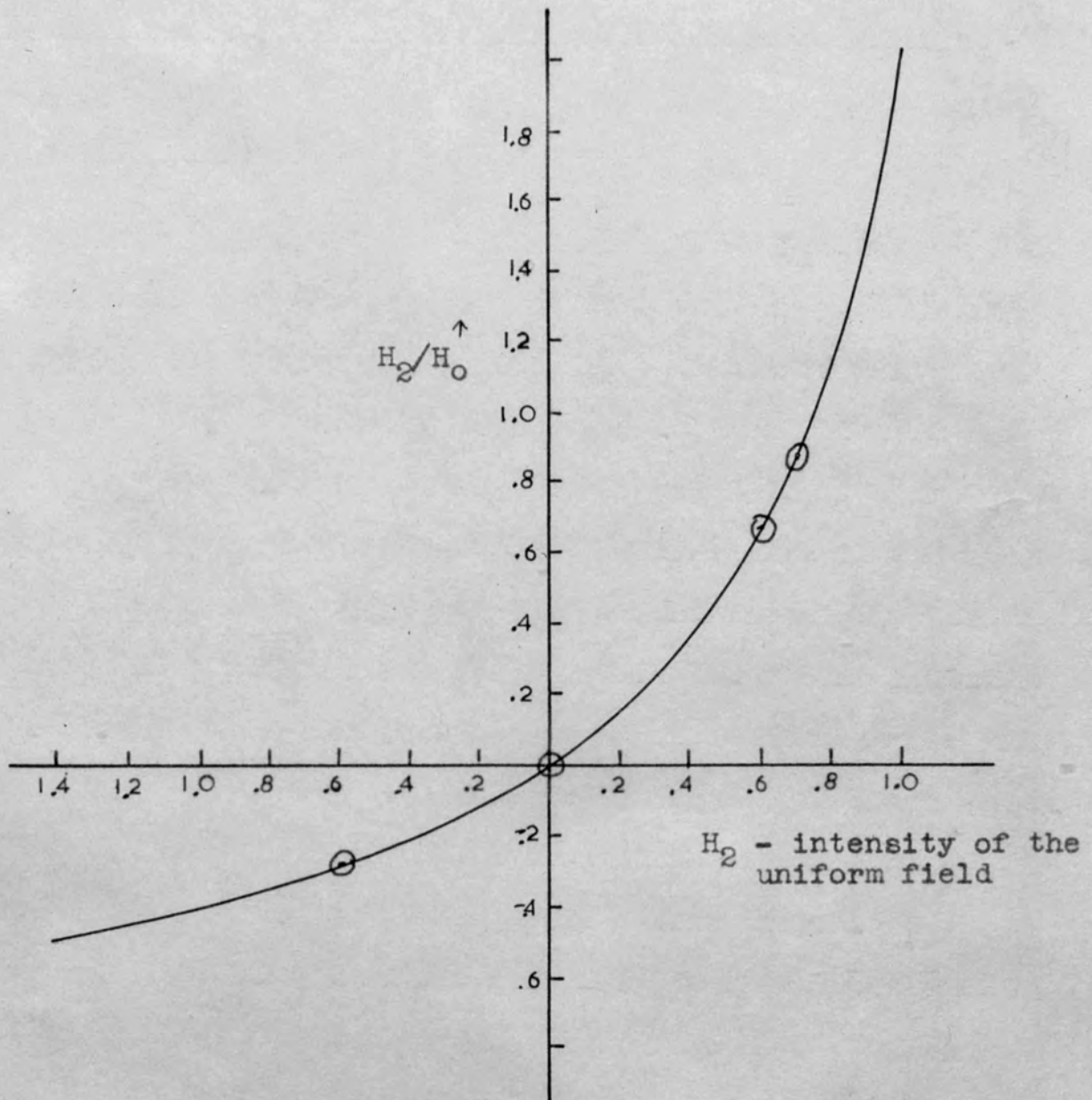
Fig. 35. Variation of the ratio H_2/H_o (ratio of the uniform field to the spheroidal at the centre of co-ordinates) such that their sum (H_2+H_o) is constant and equal to 1.5.
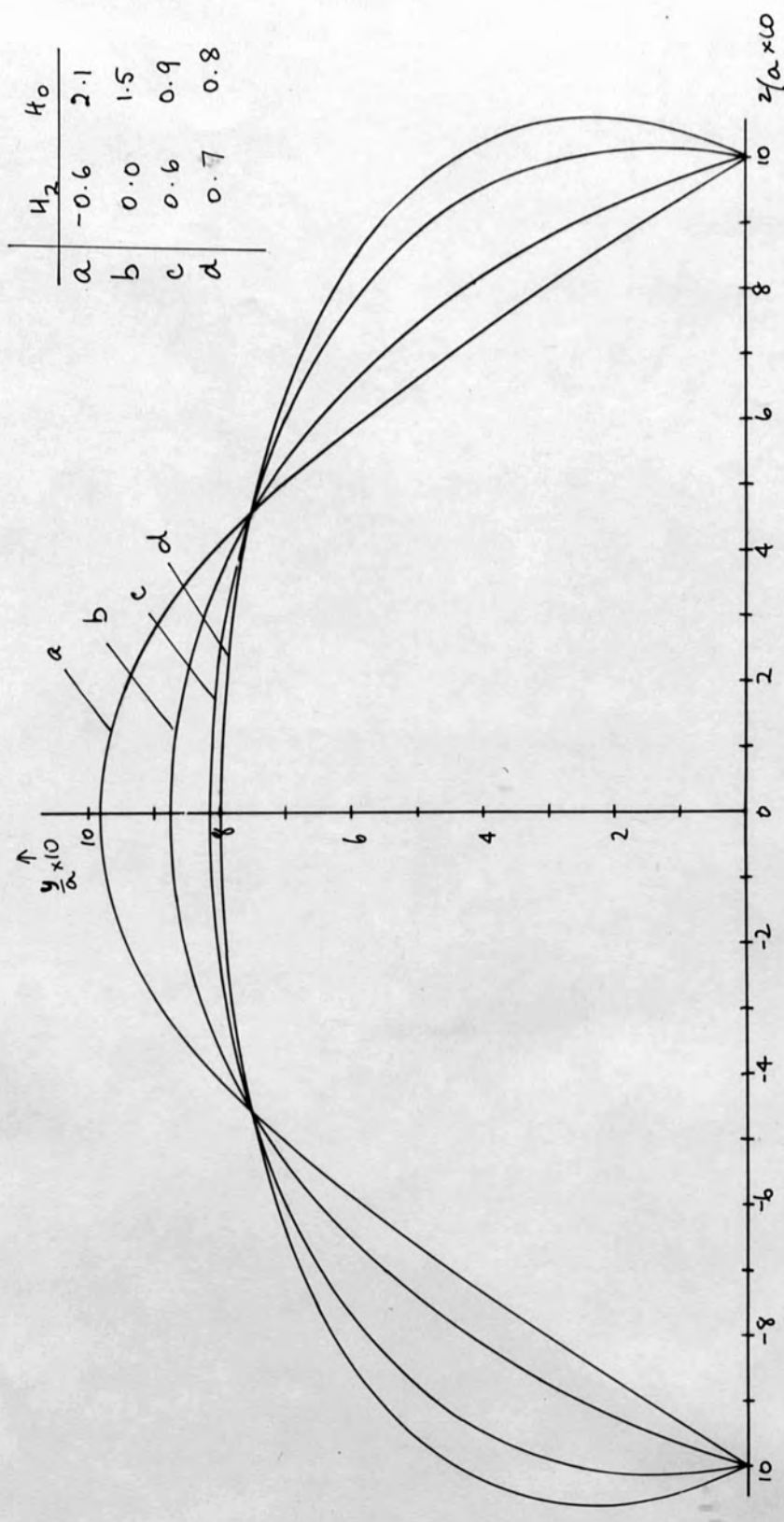
Fig. 36. Equipotentials V for the four ringed ratios H_2/H_0 of the uniform to the spheroidal field. $2V = 32$. The ratio is positive when H_2 is in the same direction as H_0, and negative if the two fields are in opposite directions (see Fig. 35).

(ii)   Equipotentials of the combined field.

In axially symmetric fields A_ϕ only exists and therefore the vector potential of the combined field can be found by adding the vector potentials of the spheroidal and uniform fields.

For the spheroidal field

$$A_\phi = \frac{\alpha^2 H_0 (\eta - 1)}{y} = A_1$$

and for the uniform field (Klemperer [18a])

$$A_\phi = A_2 = \frac{H_2 y}{2} \tag{45}$$

where H_2 is the intensity of the uniform field.

The total $A_\phi = A_1 + A_2 = \dfrac{\alpha^2 H_0 (\eta - 1)}{y} + \dfrac{H_2 y}{2}$ $\tag{46}$

To find the effect of H_2 on the equipotentials the contours of equal $|A_\phi|$ were found and then relabelled in order to simplify the calculation.

Equation (46) can be written in the following form

$$A = \alpha^2 H_0 \left(\frac{\eta - 1}{y} + \frac{H_2 y}{2 \alpha^2 H_0} \right) \tag{47}$$

Putting $\dfrac{H_2}{2a^2 H_0} = h$

equation (47) after rearrangement was written as follows

$$\frac{1}{a^2 H_0}\left(A y - h y^2\right) = (\eta - 1) \tag{48}$$

y was chosen as the independent variable and the left hand side was evaluated for the given A and h, $\eta^2 - 1$ was calculated using equation (11) and then ξ and z were found. The values of the fields H_0 and H_2 were chosen so that the intensity at the centre of the spheroidal co-ordinates was 1.5 as before, i.e.

$$H_2 + H_0 = 1.5 \tag{49}$$

H_2/H_0 as a function of H satisfying eq. (49) is plotted in Fig. 35. The equipotentials corresponding to the ringed ratios in Fig. 35 are plotted in Fig. 36. The uniform field changes the curvature of the equipotentials. This gives an extra variable parameter to ease the matching of the experimental and theoretical fields.

(iii)   The equations of motion in a combined field.

The equations of motion were derived by substituting the value of A in equation (46) into equations (20), (21) and (22).

From (46) it follows that

$$\frac{\partial A}{\partial y} = \frac{\partial A_1}{\partial y} + \frac{H_2}{2}$$

$$\frac{\partial A}{\partial z} = \frac{\partial A_1}{\partial z}$$

(49a)

With this substitution, the equations of motion become

$$\ddot{y} = -\frac{e^2}{m^2}\left(\frac{a^2 H_0(\eta-1)}{y} + \frac{H_2 y}{2}\right)\left(\frac{\partial A_1}{\partial y} + \frac{H_2}{2}\right)$$

(50)

$$\ddot{z} = -\frac{e^2}{m^2}\left(\frac{a^2 H_0(\eta-1)}{y} + \frac{H_2 y}{2}\right)\frac{\partial A}{\partial z}$$

(51)

$$y\dot{\phi} = -\frac{e}{m}\left(\frac{a^2 H_0(\eta-1)}{y} + \frac{H_2 y}{2}\right)$$

(52)

The following equations are obtained after the differentiation of A

$$\ddot{y} = -\left(\frac{a^2 H_0 e}{m}\right)^2 \left\{\frac{(\eta-1)}{y} + hy\right\}\left\{\frac{1}{2a}\left(\frac{1}{r_1} + \frac{1}{r_2}\right) - \frac{(\eta-1)}{y^2} + h\right\}$$

(53)

$$\ddot{z} = -\left(\frac{a^2 H_0 e}{m}\right)^2 \left\{\frac{(\eta-1)}{y} + hy\right\}\left\{\frac{a+z}{r_1} - \frac{a-z}{r_2}\right\}\frac{1}{2ay}$$

(54)

$$y\dot{\phi} = -\left(\frac{a^2 H_0 e}{m}\right)\left\{\frac{(\eta-1)}{y} + hy\right\}$$

(55)
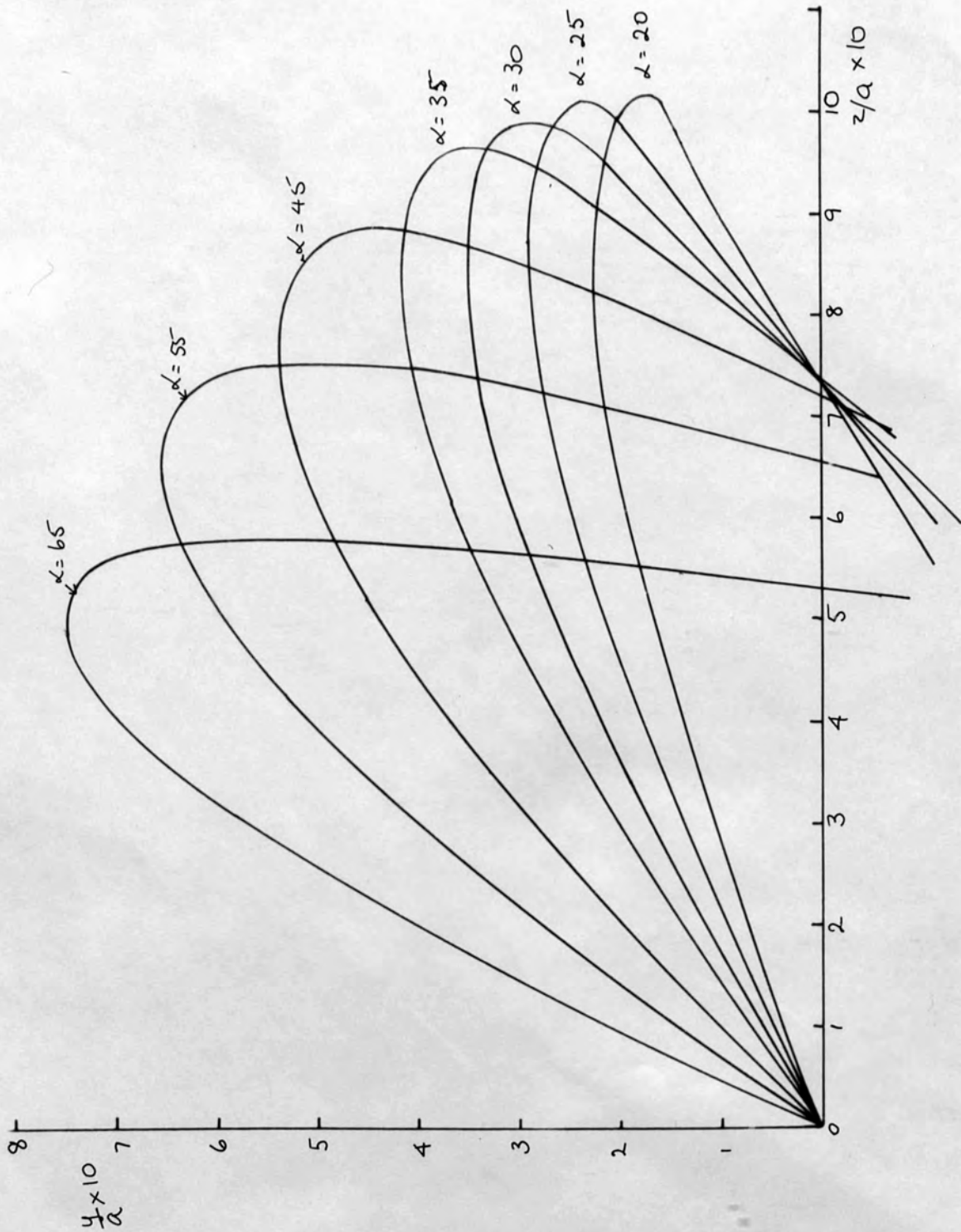
Fig. 37. Trajectories of a particle in the combined field starting in the mid plane with $p^2 = 35$.
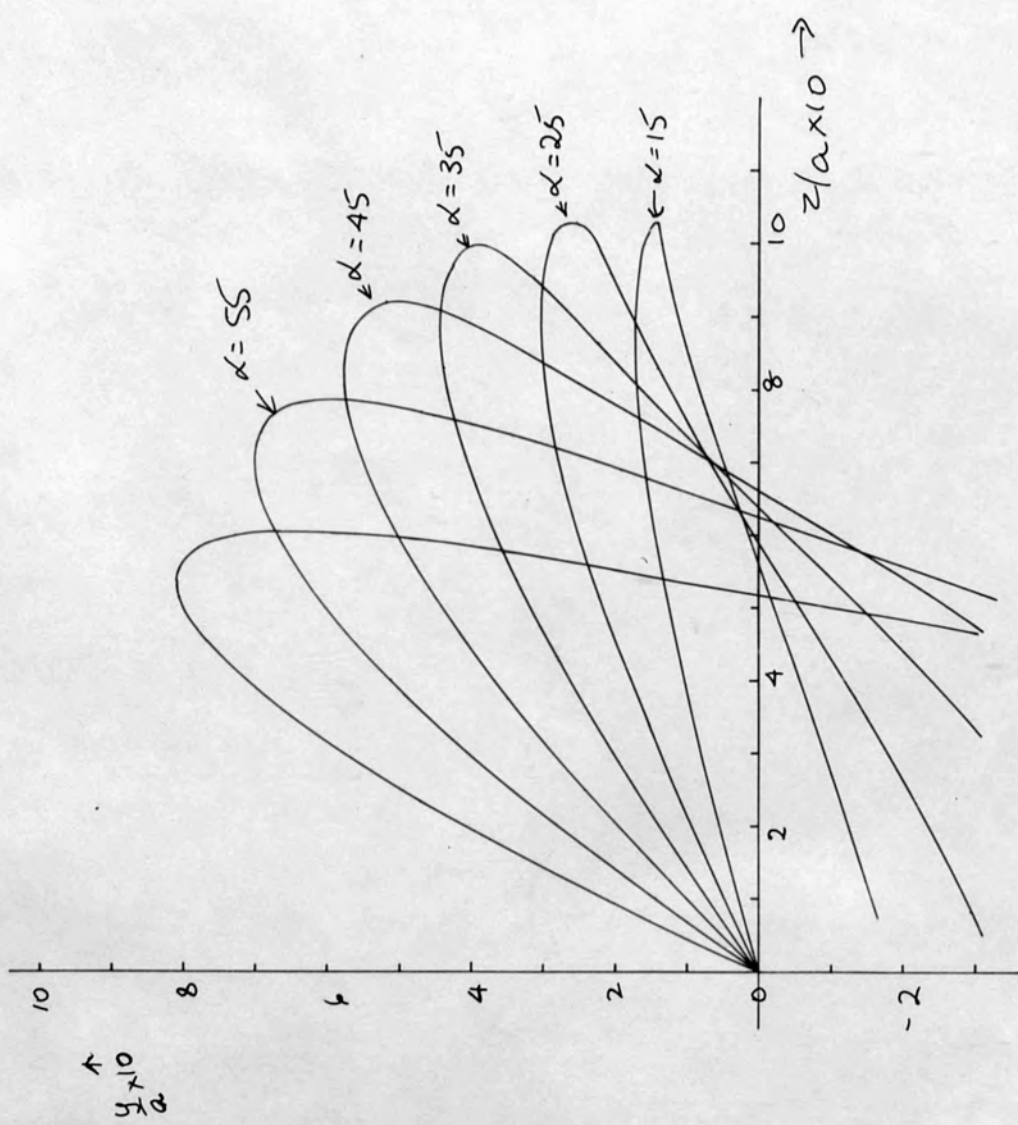
Fig. 38 . A set of trajectories of a particle in the combined field with $p^2 = 40$.

Since y appears in the denominator it is again necessary to use approximate relations in the integration if $y/a \ll 1$.

$$A \approx y \left[\frac{1}{2(a^2-z^2)} + h \right] a^2 H_0 \qquad \text{for small y, therefore,}$$

equations (53), (54) and (55) can be approximated by

$$\ddot{y} = - \left(\frac{a^2 H_0 e}{m} \right)^2 \left[\frac{y}{2(a^2-z^2)} + hy \right] \left[\frac{1}{2(a^2-z^2)} + h \right] \qquad (56)$$

$$\ddot{z} = - \left(\frac{a^2 H_0 e}{m} \right)^2 \left[\frac{y}{2(a^2-z^2)} + hy \right] \frac{zy}{(a^2-z^2)^2} \qquad (57)$$

$$y\dot{\phi} = - \frac{a^2 H_0 e}{m} \left[\frac{y}{2(a^2-z^2)} + hy \right]$$

for $y/a \ll 1$.

(iv)   <u>Properties of trajectories.</u>

The flow diagram for the programme used for integrating (53), (54) and (55) was similar to that shown in Fig. 4. Some of the trajectories obtained are shown in Figs. 37 and 38. The characteristic features of the spheroidal field are still present. The focus such as I_1 is now formed by rays with lower angles of emission with values depending on the ratio of the fields. Thus it is possible to bring rays with low angles of projection to a focus by varying the ratio H_2/H_0. The ~~two~~ cusps forming I_1 are also tilted.

The dispersion was again calculated by plotting the
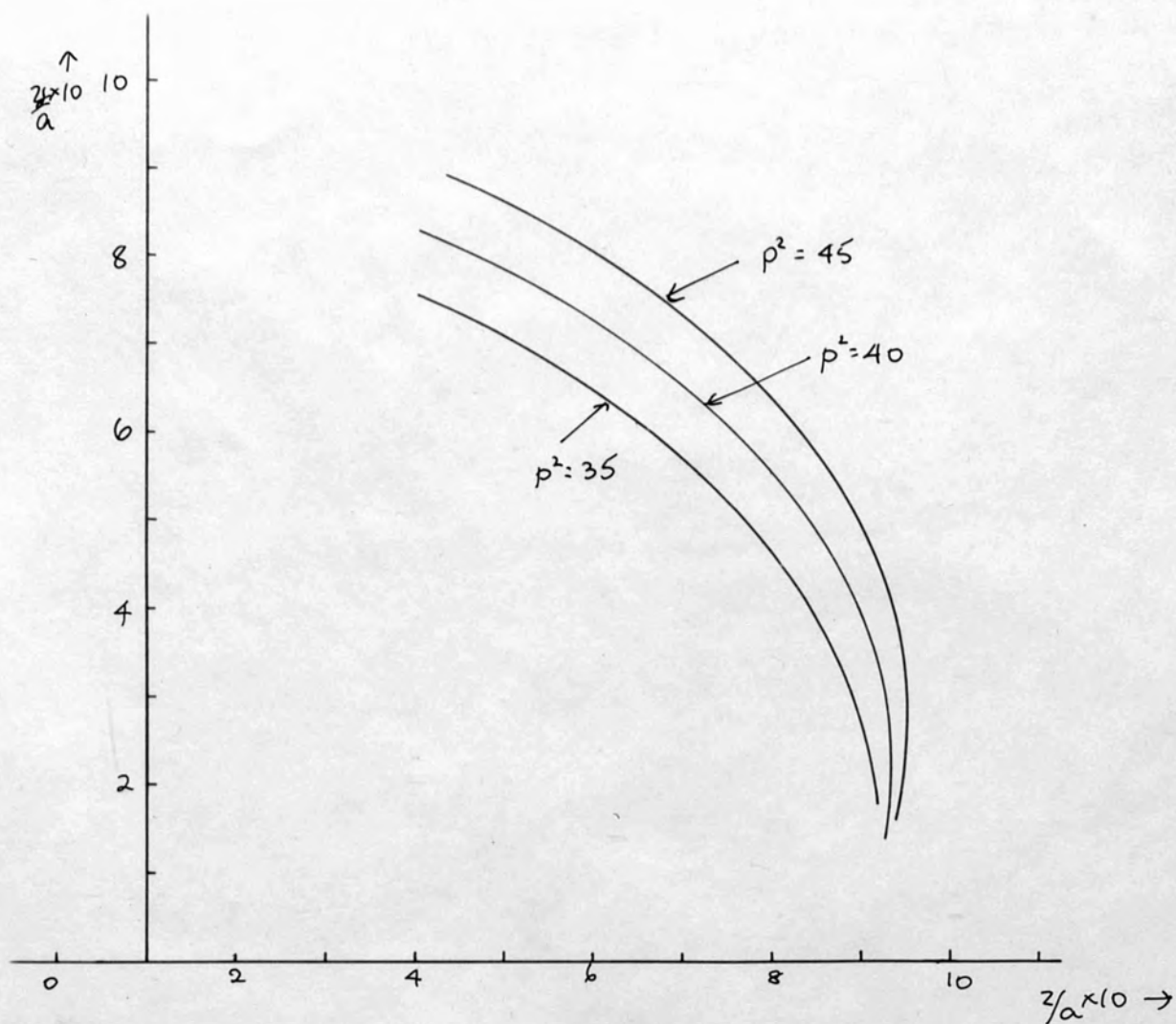
Fig. 39. Primary caustics for a particle starting in the mid plane of the combined field. The ratio of H_2/H_0 was 1/3. The caustics were used to obtain lines in Fig. 22.

Fig. 40. Various primary caustics of sets of trajectories in the combined field for various starting points and field ratios.
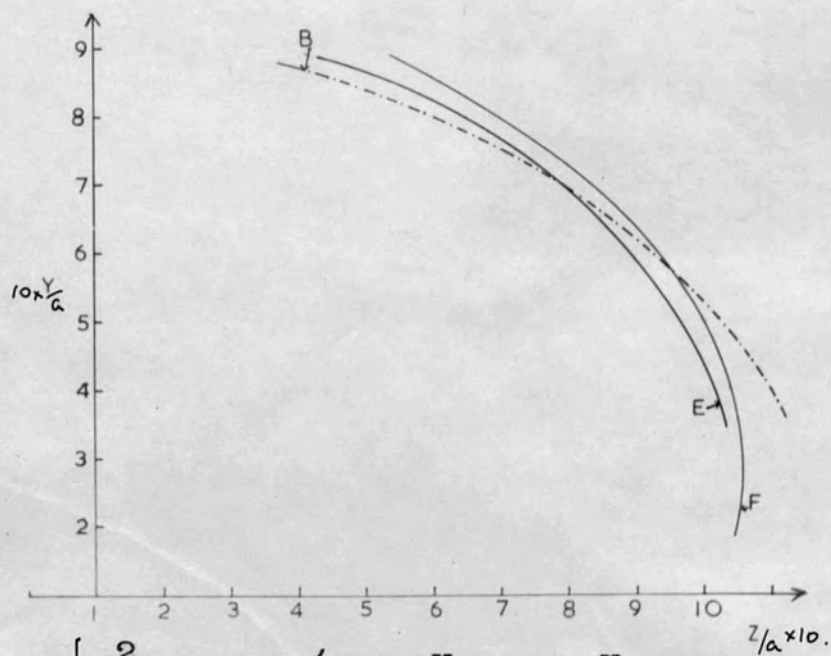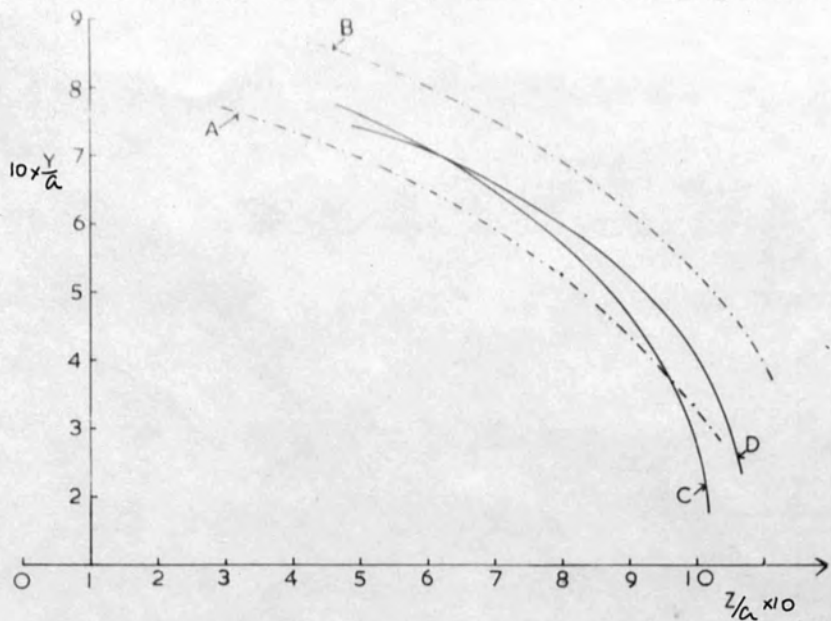
	p^2	z_o/a	H_2	H_o
A	35	−0.2	0.8	0.7
B	45	−0.2	0.8	0.7
C	35	0	0.6	0.9
D	35	0	0.8	0.7
E	45	−0.2	0.6	0.9
F	45	0	0.6	0.9

primary caustics and the variation of the y co-ordinate with p^2 for various values of z is shown in Fig. 22. This compares favourably with those of the spheroidal field. Some primary caustics for various conditions, ratios of fields and starting points are shown in Fig. 40.

The parameters s', ε and ε/T, as defined in Chapter II, were calculated for some of the trajectories and are tabulated in Table I. s' is now larger than for the spheroidal field due to the fact that, for the chosen position of the slits, the slit width is much wider for the same solid angle of collection, and the dispersion is smaller in the plane of the slit.

For the trajectories in Fig. 37 $p^2 = 35$. Therefore $B\rho/H = 3.94$ is smaller than that for the rays in Fig. 5.

(v) Comparison of the calculated and measured field along the axis of the large spectrometer.

The field can be calculated from the relation $\mu H =$ $= \text{curl } A$. In the cylindrical co-ordinates y, z, ϕ curl A is given by

$$\text{curl } A = \left(\frac{1}{y} \frac{\partial A_z}{\partial \phi} - \frac{\partial A_\phi}{\partial z} \right) i_1 + \left(\frac{\partial A_y}{\partial z} - \frac{\partial A_z}{\partial y} \right) i_2 + \left(\frac{1}{y} \frac{\partial (y A_\phi)}{\partial y} - \frac{1}{y} \frac{\partial A_y}{\partial \phi} \right) \quad (58)$$

If A_ϕ only exists, then
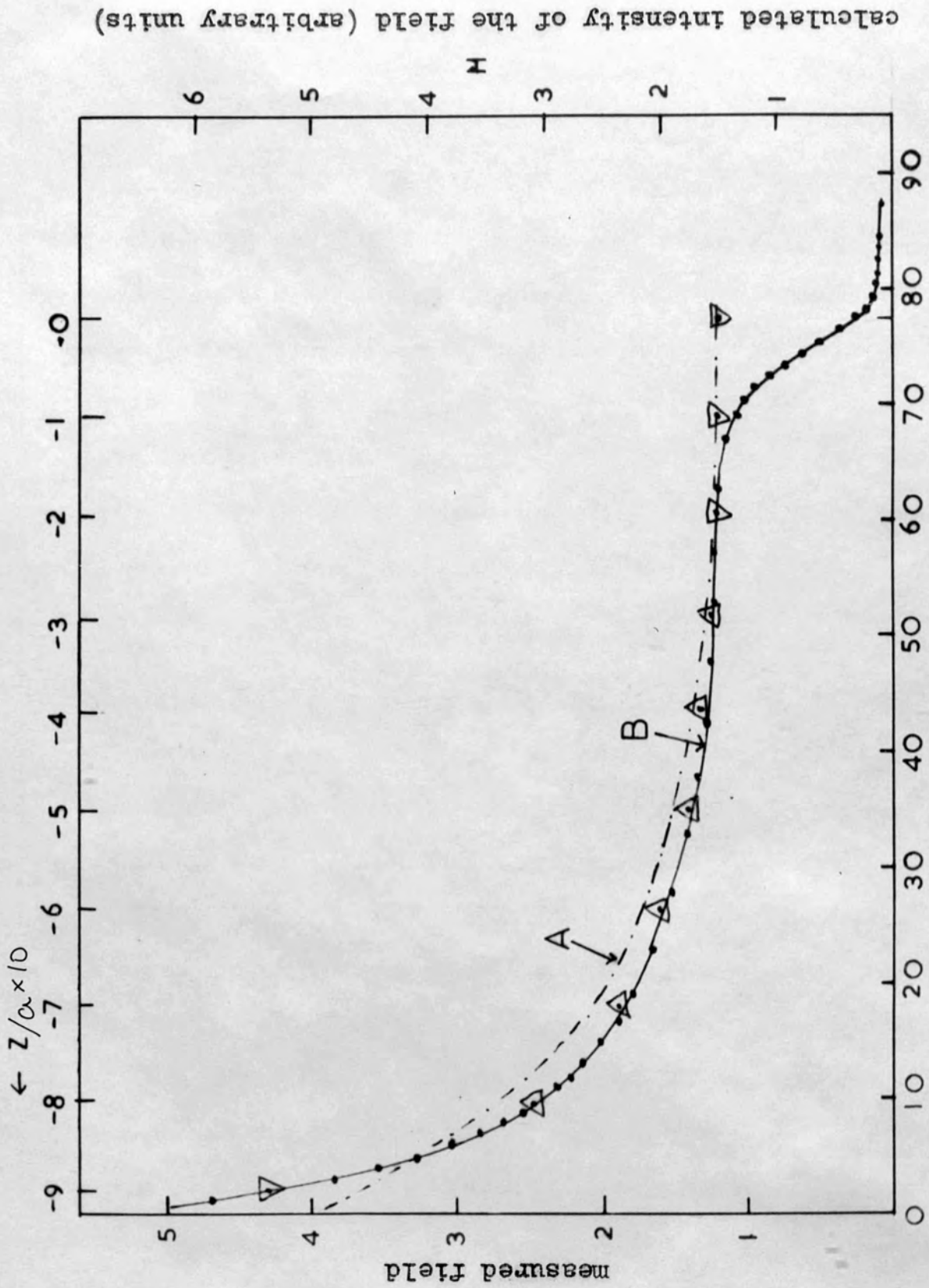
Fig. 41. Comparison of the calculated and experimental field along the axis of the large spectrometer. B – experimental curve, A – best fit with spheroidal field, ◁ – combined field.

$$\text{curl } A = -\frac{\partial A\phi}{\partial z}\, i_1 + \frac{1}{y}\frac{\partial}{\partial y}(y A_\varphi)\, i_3 \tag{59}$$

To find the field along the axis of symmetry, the limit of curl A as $y \rightarrow 0$ was calculated. On substituting for A_ϕ , one obtains

$$H(0) = \frac{a^2 H_0}{a^2 - z^2} + H_2 \tag{60}$$

$H(0)$ = field along the axis.

This was calculated for various values of $\begin{bmatrix} a & \text{for} \\ H_2/H_0 \end{bmatrix} = 2/3$ and the best fit is shown in Fig. 41. The calculated points are in triangles and the experimental points [13] are joined by the continuous curve B. The best fit for the spheroidal field is shown as a dotted line, curve A. With the exception of the field at the source the fit is very close. The spheroidal co-ordinate is plotted at the top and H is plotted on the right hand side. It seems that the pole piece is at $\xi_0 = -0.92$.

It would be interesting to find the magnification by integrating the equations of motion for a particle starting on a ring. It may be possible to reduce the spherical aberration by a suitable choice of baffles or by using a correcting field [6].

References.

1. C. Bastard, Comptes Rendus Acad. Sci. (Paris) 248 (1959) 3295.

2. C. Bastard and J. Lafouriere, J. Phys. Radium 19 (1958) 674.

3. D.B. Beard, Rev. Sci. Inst. 28 (1957) 385.

4. Braid and Richardson, Proc. Phys. Soc. A 64 (1951) 163.

5. A. Burdet, J. Phys. Radium 20 (1959) 837.

6. K.A. Dalmatova and V.M. Kelman, Nucl. Inst. and Meth.
    5 (1959) 269.

7. H. Daniel, Rev. Sci. Inst. 31 (1960) 249.

8. H. Daniel and L.J. Laslett, Rev. Sci. Inst. 31 (1960) 1225.

9. H. Daniel, Z. Naturforsch. 12a (1957) 940.

10. L. Dick, J. Phys. Radium 17 (1956) 590.

11. Dosse, Z. Tech. Phys. 17 (1936) 315.

12. J.W. DuMond, Rev. Sci. Inst. 20 (1949) 160 and 616.

13. P.R. Evans, N.J. Freeman, G.K. McGinty, B.H. Armitage and
    H.O.W. Richardson, Proc. Phys. Soc. 52 (1958) 949.

14. S. Frankel, Phys. Rev. 73 (1948) 804.

15. S. Gill, Proc. Camb. Phil. Soc. 47 (1951), 96. ~~50 (1951) 604~~.

16. P. Hubert, Physica 18 (1952) 1129.

17. J.A. Jungerman and D.B. Beard, Rev. Sci. Inst. 27 (1956) 56.
    Rev. Sci. Inst. 27 (1956) 650.

18. Klemperer, Electron Optics (Cambridge Univ. Press 1953)
    (a) p. 81 and (b) p. 115.

19. I. Lindgren, Nucl. Inst. and Meth. 3 (1958) 104.

20. V.H. Lukashev, Prib. i Tekh. Eksp. No. 2 (1961) 26.

21. D.W. Martin, The Computer Journal 1 (1958) 118.

22. Margenau and Murphy, The Mathematics of Physics and
      Chemistry (D. Van Nostrand, 1956) p. 283.

23. Mott and Sneddon, Wave Mechanics and its Applications
                              (Oxford, 1948) p. 292.

24. E. Persico, Rev. Sci. Inst. 20 (1949) 191.

25. E. Persico and C. Geoffrion, Rev. Sci. Inst. 21 (1950) 945.

26. Y. Ramburg and A.E. Blaugrund, Rev. Sci. Inst. 28 (1957)
                                                        286.

27. H.O.W. Richardson, Phil. Mag. Ser. 7, 11 (1949) 233.

28. K. Siegbahn, β- and γ-ray Spectroscopy (Amsterdam, 1955)
                                                        p. 55.

29. K.D. Sinel'nikov et al., Zh. Tekh. Fiz. 30 (1960) 256.

30. Slatis and Siegbahn, Ark. f. Fysik 1 (1949) 339.

31. W.R. Smythe (McGraw Hill, 1950), Static and Dynamic
                                        Electricity p. 268.

32. Stratton, Electromagnetic Theory (McGraw Hill, 1941) p. 51.

33. P.I. Strel'nikov et al., Zh. Tekh. Fiz. 30 (1960) 138.

34. N.F. Verster, Physica 16 (1950) 815.

35. N.F. Verster, Appl. Sci. B1 (1950) 363.

36. N.F. Verster, Progr. Nucl. Physics 2 (1952) 1.

37. C.M. Witcher, Phys. Rev. 60 (1941) 32.

38. H. Wild and O. Huber, Helv. Phys. Acta 30 (1957) 3.